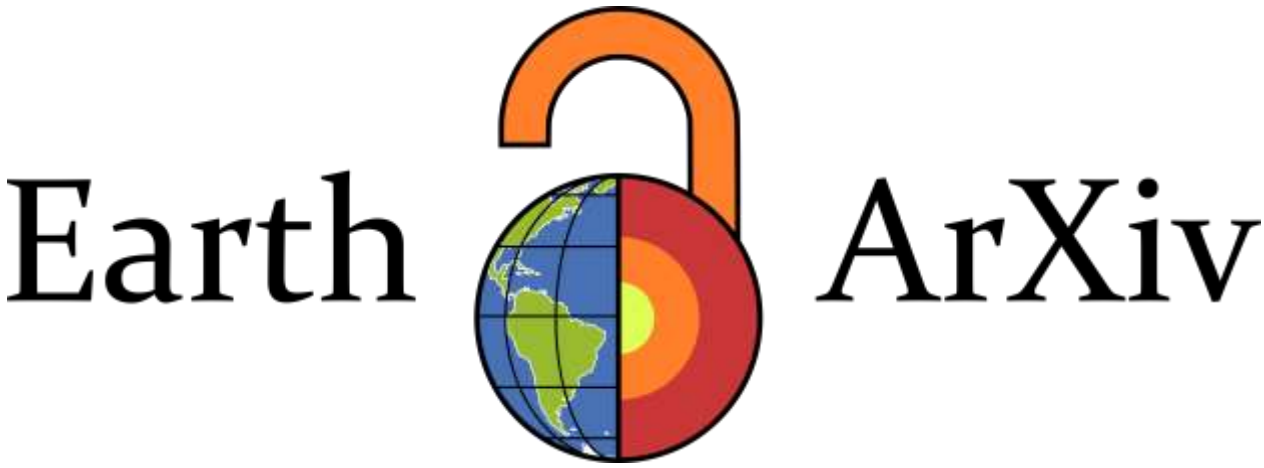

Testing the accuracy and transferability of remotely sensed biomass models across heterogeneous grasslands

Jan Schweizer[1,2*], Leon T. Hauser[1,2], Hamed Gholizadeh[3], Anna K. Schweiger[4], Christian Rossi[1,2,3]

[1]Department of Geoinformation, Swiss National Park, Runatsch 124, 7530 Zernez, CH

[2]Department of Geography, University of Zurich, Winterthurerstrasse 190, 8057 Zurich, CH

[3]Department of Geography, Oklahoma State University, 318 Social Sciences & Humanities, 74078 Stillwater, OK, USA

[4]Department of Land Resources & Environmental Sciences, Montana State University, 334 Leon Johnson Hall, 59717 Bozeman, MT, USA

[*]Author to whom correspondence should be addressed

Keywords

Model comparison, Empirical models, Physically-based models, Hybrid retrieval, Active Learning, Sentinel-2, LUT inversion, PROSAIL, Gaussian process regression

Abstract

Grassland aboveground biomass provides key insights into ecological processes such as carbon sequestration, animal movement patterns, and agricultural management practices. Different model types have been developed to estimate grassland biomass from satellite imagery. However, differences in model performance across sites with varying management and ecology remain largely understudied. In this study, we compared accuracy and transferability of empirical, physically-based, and hybrid models to estimate grassland biomass from multispectral Sentinel-2 data in an agnostic scenario, i.e., the models were not provided with any site-specific information beyond the spectral data. Based on field data from five study sites in Europe and the United States, we assessed (1)site-level accuracy of biomass estimation models, (2) model transferability between sites (domain shift), (3) the performance of models trained or optimized with data from multiple study sites (domain generalization), and (4) the relationship between epistemic uncertainty and model transferability. Our results showed that (1) all models exhibited comparable performance at the site level, (2) physically-based models showed the highest degree of transferability between sites, (3) no model consistently outperformed all other models when trained or optimized with field data from multiple sites, and (4) epistemic uncertainty was not necessarily a reliable measure of model applicability to unseen data. Our findings demonstrate the challenges associated with grassland biomass models under domain shift. This elucidates limits to agnostic inference in targeting diverse grasslands and highlights that model transferability is an integral part of performance assessment towards scalable satellite-based grassland monitoring systems, especially as the community increasingly deploys models at continental to global scales.

1. Introduction

Grasslands cover up to 40% of Earth's terrestrial surface (White et al., 2000) and two-thirds of the Earth's agricultural land area (O'Mara, 2012). With their extensive land coverage, grasslands store around a third of the global terrestrial carbon (Bai and Cotrufo, 2022) and host many endemic species (Hobohm and Bruchmann, 2009). At the same time, grasslands provide essential ecosystem services (Lemaire et al., 2011; Zhao et al., 2020) including global food production (Bengtsson et al., 2019; O'Mara, 2012). Given their ecological, cultural, and economic importance, accurate monitoring of grasslands is imperative to counteract declines in biodiversity and ecosystem services (Bardgett et al., 2021).

Within the overall objective of grassland monitoring, the accurate and reliable estimation of aboveground biomass (hereafter referred to as biomass) is critical for quantifying numerous ecological processes and effects of human disturbances. Biomass is an important parameter for Earth System Models (e.g., Lawrence et al., 2019) and for estimating the contribution of grasslands to the global carbon cycle (Erb et al., 2018). Grassland biomass is also a key driver of animal movement and grazing patterns (Bailey et al., 1996; Rempfler et al., 2024; Schweiger et al., 2015b), and provides information about management practices such as mowing (De Vroey et al., 2022), whose timing and frequency are linked to biodiversity (Socher et al., 2012; Van Vooren et al., 2018) and productivity (Zhang et al., 2023).

For large-scale grassland biomass estimation, spaceborne remote sensing enables repeated observations across large spatial domains. Optical sensors measuring surface reflectance, such as those onboard the European Space Agency's (ESA) Sentinel-2 and the National Aeronautics and Space Administration's (NASA)/United States Geological Survey's (USGS) Landsat satellites, are widely used to examine vegetation dynamics of grasslands (Reinermann et al., 2020). Open data policies have supported the availability of many years of archived data (Gascon et al., 2017; Masek et al., 2020; Roy et al., 2014). The spectral layout of Sentinel-2 has

shown to hold viable information to estimate foliar properties and canopy structure used to infer biomass (de Sá et al., 2021; Guerini Filho et al., 2020; Hauser et al., 2021a; Rossi et al., 2020). However, many grasslands are subject to high levels of spectral complexity arising from several factors, including effects of non-photosynthetically active vegetation (NPV; Xu et al., 2014), co-occurring plant functional types (Dixon et al., 2014), and management regimes affecting grassland phenology and species composition (Ali et al., 2016; Rossi et al., 2024).

This complexity led to the emergence of different model types to estimate biomass, including the use of vegetation indices (VIs), empirical, physical, and hybrid models. Each of these model types has its specific trade-offs regarding required field data, model complexity, specificity, and transferability (i.e., domain shift). Vegetation indices (VIs), such as the Normalized Difference Vegetation Index (NDVI; Guerini Filho et al., 2020; Li et al., 2016; Wang et al., 2019), are found to correlate to various vegetation properties at both the leaf and canopy level. They are straightforward to use, but can saturate with high amounts of biomass (Huete et al., 2002; Zeng et al., 2023). Empirical models are statistical models trained and validated using field data. Deriving relationships from the training data, they do not rely on prior knowledge about the relationship between input and output variables, and are generally well-equipped to handle non-linearity and noise often present in remote sensing data (Verrelst et al., 2015). Numerous empirical machine and deep learning models such as Random Forest regression (RFR), Support Vector regression (SVR), Extreme Gradient boosting (XGB), Gaussian process regression (GPR) and Deep Neural Networks (DNN) have been successfully used to estimate grassland biomass and vegetation traits from optical Sentinel-2 and Sentinel-1 synthetic aperture radar (SAR) data (Li et al., 2021; Muro et al., 2022; Raab et al., 2020; Schwieder et al., 2020; Verrelst et al., 2012). Physically-based Radiative Transfer Models (RTMs) simulate the interactions between light and matter at leaf- and canopy-scales reducing reliance on field data and improving domain generalization by leveraging universal physical principles (He et

al., 2019; Wang et al., 2023). RTM inversion can be achieved by using a look-up table (LUT) approach (Verrelst et al., 2014), which connects simulated or measured spectra with trait combinations linked to those spectra. For example, the PROSAIL RTM (Jacquemoud et al., 2009) can be inverted to estimate grassland biomass derived by multiplying leaf dry matter content with leaf area index (LAI; see e.g., He et al. (2019)). However, the PROSAIL RTM is based on heavily idealized assumptions, such as uniformly distributed leaf constituents and geometrically homogeneous canopies (Jacquemoud and Baret, 1990; Verhoef et al., 2007), that are never met in reality. Hybrid models combine RTM-simulated canopy spectra with machine learning models for model inversion (Verrelst et al., 2015). Active Learning (AL) is often used in combination with hybrid models to select the most informative training samples (Verrelst et al., 2016) to perform the RTM inversion which is inherently ill-posed (Combal et al., 2003), coming however at the potential cost of model transferability (Berger et al., 2021b; Tagliabue et al., 2022). Hybrid models have been successfully used for estimating vegetation properties in croplands (Berger et al., 2021a, 2020; Ranghetti et al., 2022; Tagliabue et al., 2022; Verrelst et al., 2021; Wocher et al., 2022) and forests (Binh et al., 2022; Brown et al., 2019; Hauser et al., 2021a; Yuan et al., 2015). However, the findings from these previous studies cannot be simply extended to grasslands, since grasslands are more chemically and structurally diverse compared to croplands and differ in plant size and canopy characteristics from forests (Habel et al., 2013; Wellstein et al., 2013). Grasslands also tend to violate the assumption of geometrically homogeneous canopies of one-dimensional RTMs (Berger et al., 2018; Rossi et al., 2020), complicating the selection of the most appropriate model for a given application.

In this paper, we aim to compare well-established empirical, physically-based, and hybrid models to estimate biomass across grassland sites with different management regimes, altitude and climate, and determine model performance by assessing their local accuracy, transferability, and epistemic uncertainty (= model uncertainty referring to the confidence of a

model about its prediction) sensu Martínez-Ferrer et al. (2022). In doing so, we are focusing on an agnostic scenario, meaning that the models were not provided with any site-specific information beyond the spectral data. The rationale behind this scenario is the endeavor to develop accurate grassland biomass models using only widely available remote sensing data, as site-specific ancillary data often represent an operational bottleneck. Our goals are to develop adequate grassland biomass estimation models for each site and to identify key considerations for domain shift and generalization.

2. Methods

2.1. Study sites and data acquisition

We used field and remote sensing data from five study sites: one in Switzerland, three in Germany, and one in the United States differing in environmental characteristics, including altitude, climate, and management practices (Table 1, Figure 1). These differences make our compiled dataset particularly valuable for assessing model transferability. The number of samples per study site ranged from 100 to 429, but we based all our models on 100 samples to keep them comparable. For sample selection we used Latin hypercube sampling (LHS) as implemented in the clhs package *v0.9.0* (Roudier, 2021) in R *v4.2.1* (R Core Team, 2021).

Table 1: Overview of the characteristics of the five study sites covering a wide range of topographic and climate, and management practices. Remote sensing data were acquired with the Airborne Prism Experiment (APEX) and Sentinel-2 between 2010 and 2020. The Köppen-Geiger climate classification is following Beck et al. (2018) for period 1991-2020. Dominant species are provided for Switzerland by the Swiss National Park's long-term permanent grassland monitoring project, for Germany by Bolliger et al. (2020), and for the United States by Gholizadeh et al. (2022). m.a.s.l.: meters above sea level, MAT: mean annual air temperature, MAP: mean annual precipitation.

Country	Switzerland		Germany			United States
Site code	CH		ALB	HAI	SCH	US
Site	Swiss National Park	Lower Engadine, Val Müstair	Schwäbische Alb	Hainich-Dün	Schorfheide-Chorin	The Nature Conservancy's Tallgrass Prairie Preserve (Pawhuska, OK)
Elevation [m.a.s.l.]	1,400 – 2,500		460 – 860	285 – 550	3 – 140	252 - 365
MAT [°C]	1 (at 2,000 m.a.s.l.)		6 – 7	6.5 – 8	8 – 8.5	17.4
MAP [mm/a]	800		700 – 1,000	500 – 800	500 – 600	960
Köppen-Geiger climate class	Cold, no dry season, cold summer (Dfc)		Cold, no dry season, warm summer (Dfb)	Mostly Cfb, small areas Dfb	Temperate, no dry season, warm summer (Cfb)	Temperate, no dry season, hot summer (Cfa)

Dominant species	*Erica carnea, Nardus stricta, Carex sempervirens, Festuca rubra*		*Alopecurus pratensis, Taraxacum* sp., *Festuca rubra* aggr., *Bromus erectus*	*Poa pratensis* aggr., *Taraxacum* sp., *Lolium perenne, Alopecurus pratensis*	*Poa pratensis* aggr., *Lolium perenne, Poa trivialis, Elymus repens*	*Schizachyrium scoparium, Andropogon gerardii, Sorghastrum nutans, Panicum virgatum*
Management	Strict protection	Grazing, mowing, fertilizing				Grazing, burning
Sensor	Resampled APEX	Sentinel-2				
Years	2010 - 2013	2016 - 2017	2017 - 2020			2022
Number of available samples	407	22	194	185	146	100
Number of selected samples	78	22	100	100	100	100

137

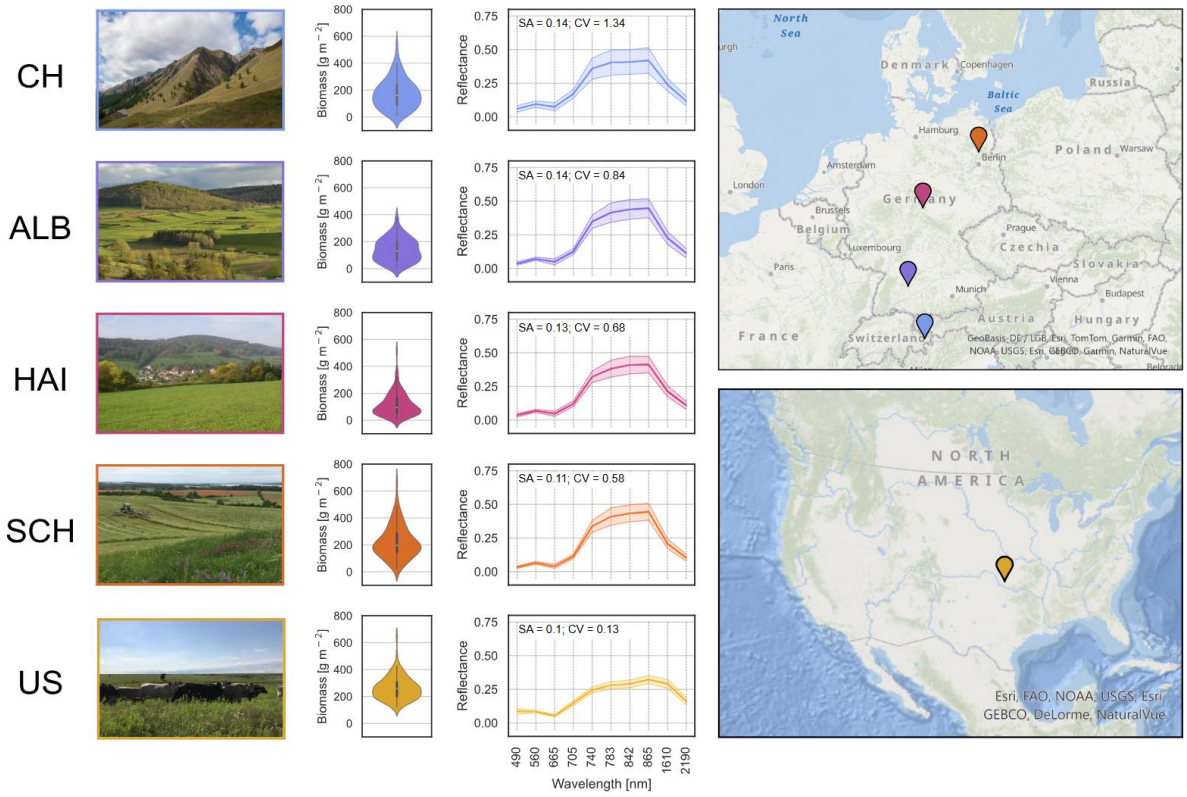

Figure 1: Overview of the five study sites. Violin plots show dried aboveground biomass for the 100 selected samples per site. Line plots show the mean spectra (± 1 standard deviation) per site for Sentinel-2 or resampled APEX data. Mean spectral angle in radians (SA; Yuhas et al., 1992) of all unique sample combinations and coefficient of variation (CV) for all spectral bands serve as indicators of site-specific spectral variability. CH: Switzerland, image credits: Swiss National Park/Hans Lozza. ALB: Schwäbische Alb, image credits: Biodiversity Exploratories Information System (BExIS)/Martin Fellendorf. HAI: Hainich-Dün, image credits: BExIS/Steffen Both. SCH: Schorfheide-Chorin, image credits: BExIS/Ulrike Garbe. US: United States, image credits: Nicholas McMillan.

2.1.1. Switzerland

The Swiss study site (site code CH) encompasses the Lower Engadine and the Val Müstair in the Canton of Grisons in southeast Switzerland. Plots located in the Swiss National Park (SNP), an IUCN (International Union for the Conservation of Nature) category Ia nature reserve (highest protection level – strict nature reserve), are unmanaged. Plots in the Lower Engadine and the Val Müstair adjacent to the SNP are fertilized, mown, and grazed to varying degrees (Rossi et al., 2020).

154 At the CH site, biomass sampling for took place on the day of remote sensing data acquisition
155 in late June to early July of 2010 – 2013 and 2016 – 2017, respectively. Biomass was clipped
156 approximately 1 cm above the ground in 1 m^2 plots representative for a homogeneous area of 6
157 × 6 m, and dried at 65° for 48 h for 429 samples (Rossi et al., 2020; Schweiger et al., 2017,
158 2015b, 2015a). From 2010 to 2013 (before the launch of Sentinel-2), remote sensing data were
159 acquired with the Airborne Prism Experiment (APEX) imaging spectrometer (Jehle et al., 2010;
160 Schaepman et al., 2015). APEX data were resampled to 2 m pixel size using nearest neighbor
161 interpolation and the parametric geocoding procedure PARGE (Schläpfer and Richter, 2002)
162 and the airborne atmospheric and topographic correction model ATCOR-4 (Richter and
163 Schläpfer, 2002) were used for geometric and atmospheric correction, respectively (Schweiger
164 et al., 2015b). APEX data were resampled to Sentinel-2 bands (Appendix A Section A.1) using
165 the prospectr R package *v0.2.6* (Stevens and Ramirez-Lopez, 2022) in R *v4.2.1*, and can be
166 considered comparable with Sentinel-2 (Helfenstein et al., 2022). In 2016 and 2017, Sentinel-
167 2 Level-1C (top of atmosphere) images were downloaded from the Copernicus Open Access
168 Hub (https://scihub.copernicus.eu/dhus/) and processed to Level-2A (surface reflectance) using
169 Sen2Cor *v2.3* (Müller-Wilm et al., 2013) and the SRTM 90 m digital elevation model (Reuter
170 et al., 2007). The 10 m bands (B2, B3, B4, B8) were aggregated to a spatial resolution of 20 m
171 using the arithmetic mean and bidirectional reflectance distribution function (BRDF) correction
172 was applied following Poortinga et al. (2019). No cloud masking was required. For each plot,
173 the spectral reflectance was sampled in the respective Sentinel-2 image by calculating the
174 weighted mean on 20 m resolution around the plot center coordinate.

175 2.1.2. Germany

176 The three German study sites (site codes ALB, HAI, SCH) are part of the *Biodiversity*
177 *Exploratories* (https://www.biodiversity-exploratories.de/en/). At each site, 50 grassland plots
178 with different management regimes have been closely monitored since 2009 (Fischer et al.,

2010; Hinderling et al., 2023; Ostrowski et al., 2020). Management intensity varies from extensive to moderately intensive, e.g., from no mowing or fertilization to three mowing events per year plus fertilization (Blüthgen et al., 2012; Fischer et al., 2010).

Biomass was harvested between late April and mid-July from 2017 to 2020 by clipping biomass approximately 4 cm above the ground on an area of 2 m^2 in plots representative of a homogeneous area of 50 × 50 m and subsequent drying at 80° for 48 h, resulting in 600 samples (Hinderling et al., 2023). We linearly scaled the dry biomass content to 1 m^2 for consistency with the other study sites. Sentinel-2 Level-2A data closest to the day of biomass harvest were acquired through the Google Earth Engine (GEE, Gorelick et al., 2017) using the "Harmonized Sentinel-2 MSI: MultiSpectral Instrument, Level-2A" collection. The s2cloudless algorithm was used to mask out clouds and cloud shadows with the cloud probability threshold set to 10% (Zupanc, 2017). Again, the 10 m bands were aggregated to 20 m using the function *reduceResolution* in GEE and BRDF correction was applied. Sampling of the spectral reflectance for each plot follows the protocol for the CH site. An NDVI threshold was applied to prevent the inclusion of plots influenced by artifacts such as remaining cloud shadows or inhomogeneous vegetation cover (Appendix A Section A.2) with 525 samples remaining (Table 1).

2.1.3. United States

The study site in the United States (site code US) is located near Pawhuska, Oklahoma, and falls within The Nature Conservancy's Tallgrass Prairie Reserve (TGPP), encompassing an area of approximately 160 km^2 mostly covered by tallgrass prairie with some oak woodland (Hamilton, 2007; The Nature Conservancy, 2023). The TGPP is managed by cattle or bison grazing, and patch burning (Sherrill, 2019). This creates a *"shifting mosaic"* (Fuhlendorf and Engle, 2004) of patches with varying grazing pressure, as bison and cattle tend to primarily

graze in recently burned areas with high nutrient availability (Anderson et al., 2006; Fuhlendorf and Engle, 2001).

Biomass sampling was conducted between July and August 2022 across 100 plots of 30 × 30 m, each containing nine 1 m^2 quadrats (Gholizadeh et al., 2024). Biomass was clipped in 80 of the 900 1 m^2 quadrats at approximately 2.54 cm (1 inch) above ground and dried at 65° for 144 h. In the remaining quadrats, biomass was determined using the digital obstruction method using the 80 samples for calibration (Limb et al., 2007). For each of the 100 plots, biomass was calculated as the mean biomass across the nine quadrats. Sentinel-2 Level-2A data for each plot were acquired following the same protocol as for the German study sites.

2.2. Model types

We assessed the accuracy and transferability of three different model types (i.e., empirical, physically-based, and hybrid; Figure 2). Field data were partitioned into training (for the empirical models) or optimization (for the physically-based and hybrid models) and external testing sets using an 80:20% split using LHS (Figure 2A). We used scikit-learn *v1.5.2* (Pedregosa et al., 2012) and xgboost *v2.1.2* (Chen and Guestrin, 2016) in Python 3.13 for model training, optimization, and validation.

2.2.1. Empirical models

A wide variety of algorithms can be used to train empirical models (Figure 2B). We used Random Forest regression (RFR), Support Vector regression (SVR), Extreme Gradient boosting regression (XGB), and Gaussian process regression (GPR) models to represent both tree-based and kernel-based methods. These algorithms all have been successfully used to estimate grassland biomass (Li et al., 2021; Muro et al., 2022; Raab et al., 2020; Schwieder et al., 2020; Verrelst et al., 2015, 2012). RFR uses an ensemble of decision trees, where each tree is trained on a random subset of samples and features and the final prediction is obtained by

227 averaging the predictions of all trees (Breiman, 2001). SVR was originally introduced by
228 Vapnik et al. (1997) and uses support vectors to fit hyperplanes in the data within a specified
229 margin of tolerance. XGB is based on the concept of gradient boosting of regression trees
230 introduced by Friedman (2001) and incorporates regularization to mitigate overfitting (Chen
231 and Guestrin, 2016). Lastly, GPR uses a prior belief about the latent function describing the
232 relationship between input and output variables, and training data to form the posterior
233 distribution (Rasmussen and Williams, 2006). The advantages of using GPR include automatic
234 hyperparameter optimization during model training and the provision of epistemic uncertainty
235 (Verrelst et al., 2013a). To predict a data point, the model returns the mean of the posterior
236 distribution as the estimated value and the predictive standard deviation (SD) as a measure of
237 epistemic uncertainty.

238 A 5-fold cross-validation (CV) scheme with negative RMSE for scoring was used to identify
239 the optimal model parametrization from all possible combinations of parameters listed in Table
240 2.

241 *Table 2: Parameter values used for cross-validation of empirical Random Forest regression (RF), Support Vector regression*
242 *(SVR), Extreme Gradient Boosting regression (XGB), and Gaussian process regression (GPR) models. Nomenclature of*
243 *parameter names for RFR, SVR, and GPR according to Pedregosa et al. (2012), for XGB according to Chen and Guestrin (2016).*

Model	Parameter function	Parameter name	Values
RF	Number of trees	n_estimators	100, 200, 500
	Maximum tree depth	max_depth	None, 5, 10, 15
	Minimum number of samples required to be at a leaf node	min_samples_leaf	1, 2, 5
	Number of features	max_features	‘sqrt’, ‘log2’, 10
	Maximum number of leaf nodes	max_leaf_nodes	10, 20, None
SVR	Kernel type	kernel	‘rbf’, ’linear’
	Kernel coefficient	gamma	‘scale’, ‘auto’, 0.01, 0.1, 1
	Regularization parameter	C	0.1, 1, 10, 100
	Epsilon-tube	epsilon	0.01, 0.1, 0.5, 1
XGB	Number of gradient boosted trees	n_estimators	100, 200, 300

	Maximum tree depth	max_depth	3, 5, 7, 9
	Boosting learning rate	learning_rate	0.01, 0.1, 0.2
	Subsample ratio of training instance	subsample	0.8, 1
	Subsample ratio of columns when constructing each tree	subsample_bytree	0.8, 1
	Minimum loss reduction	gamma	0, 0.1, 0.2
GPR	Kernel	kernel	ConstantKernel() * RBF()
	Length scale bounds of RBF kernel	length_scale_bounds	(-100, 100)

244

245 2.2.2. Physically-based model

246 Here we used the PROSAIL RTM (Jacquemoud et al., 2009), which combines the PROSPECT-
247 D (Féret et al., 2017) and 4SAIL (Verhoef et al., 2007) RTMs, to simulate grassland canopy
248 reflectance (Figure 2C). PROSPECT-D simulates leaf level reflectance by considering leaf
249 properties such as chlorophyll content (CHL), leaf mass per area (LMA) and the angle of
250 incoming solar radiation (Féret et al., 2008). Subsequently, 4SAIL computes the bidirectional
251 reflectance at the canopy level, employing canopy properties such as LAI and sun-target-sensor
252 geometry. We used the prosail R package *v1.1.1* (Féret and de Boissieu, 2022) in R *v4.2.1* to
253 create a single LUT for all study sites containing 10,000 simulated canopy reflectance spectra
254 with input parameters selected by means of LHS within their respective value ranges (Table 3)
255 derived from satellite image metadata, prior knowledge, and literature (He et al., 2019; Rossi
256 et al., 2020; Verrelst et al., 2021). The value ranges and size of the LUT were consistent with
257 other studies (Darvishzadeh et al., 2011; Hauser et al., 2021a; Locherer et al., 2015; Punalekar
258 et al., 2018; Rivera et al., 2013; Rossi et al., 2020). We used the psoil parameter as weighting
259 factor for the dry and wet soil spectra with psoil = 0 corresponding to completely wet soil
260 conditions and psoil = 1 corresponding to completely dry soil conditions, respectively. We used
261 the default dry and wet soil spectra of the prosail R package and did not use site-specific soil
262 spectra, as no corresponding reference data were available and their use would have

contradicted the agnostic modeling scenario. The simulated reflectance spectra were resampled to Sentinel-2 bands using the prospectr R package and their corresponding biomass content was calculated following Quan et al. (2017, Equation 1).

$$biomass\ [g\ m^{-2}] = LMA\ [g\ cm^{-2}] * LAI * 10{,}000 \qquad (1)$$

Table 3: Value ranges and distributions of PROSAIL input parameters used in this study.

Parameter	Variable	Unit	Minimum value	Maximum value	Distribution
Leaf structure parameter	N	[-]	1.5	1.9	uniform
Chlorophyll content	CHL	[µg cm^{-2}]	5	75	uniform
Carotenoid content	CAR	[µg cm^{-2}]	2	60	uniform
Anthocyanin content	ANT	[µg cm^{-2}]	0	2	uniform
Brown pigment content	BROWN	[-]	0	1	uniform
Equivalent water thickness	EWT	[cm]	0.001	0.04	uniform
Leaf mass per area	LMA	[g cm^{-2}]	0.002	0.015	uniform
Angle for incident light at leaf surface	alpha	[°]	40	40	fixed
Leaf inclination distribution function	TypeLidf	[-]	2	2	fixed
Average leaf angle	LIDFa	[°]	40	70	uniform
Leaf area index	LAI	[-]	0.1	4	uniform
Hot spot parameter	q	[-]	0.01	0.1	uniform
Sun zenith angle	tts	[°]	25	75	uniform
Observer zenith angle	tto	[°]	0	0	fixed
Relative azimuth angle	psi	[°]	50	180	uniform
Dry/wet soil factor	psoil	[-]	0	1	uniform

Two parameters must be determined for the inversion of the generated LUT: the cost function and the number of spectra with the lowest cost to consider (hereafter referred to as percentage of solutions). We tested 17 commonly used cost functions listed by Rivera et al. (2013) and different percentages of solutions, namely 0.01% (= 1 solution), 1%, 2%, 5%, and 10% (Punalekar et al., 2018; Rivera et al., 2013; Rossi et al., 2020) to optimize parameter choice. The predicted biomass value was calculated as the mean value of the selected solutions, with

the corresponding SD being indicative of epistemic uncertainty (Locherer et al., 2015; Rivera et al., 2013).

2.2.3. Hybrid model

For the hybrid model, we created a LUT containing 1,000 simulations (Tagliabue et al., 2022; Verrelst et al., 2021) as described above. But in this case, the simulated canopy reflectance spectra were used to train a regression algorithm for RTM inversion (Figure 2D). Here we used a GPR model (see Section 2.2.1 for further details) with the parameters indicated in Table 2 for the regression task. We used AL to avoid biophysically unrealistic variable combinations and redundant information, and select the most informative simulations from the LUT (Verrelst et al., 2016). Using the AL-selected subset of simulations for GPR training can help to mitigate the ill-posedness inherent to RTM inversion as different variable combinations can lead to similar spectra (Combal et al., 2003), and increase computational efficiency (Berger et al., 2021b). AL selects a predefined percentage of simulations from the LUT as an initial training dataset. Subsequently, the GPR model is trained using this initial training set, and its predictive training accuracy is assessed via the root-mean-square error (RMSE) computed with the optimization set. By employing a selection heuristic, such as Euclidean distance-based diversity (EBD), a simulation from the remaining LUT is selected, temporarily added to the training set, and only permanently kept if the updated training set leads to an improved RMSE. This optimization process continues until all simulations are evaluated. Finally, the validation accuracy of the GPR model trained with the optimal training set is determined.

In line with previous studies, we used 2% of the data as initial training data (Tagliabue et al., 2022; Wocher et al., 2022). Hybrid models without the use of AL did not lead to meaningful results in the context of this study (Appendix A Section A.3) and were therefore not further analyzed.

2.3. Model comparisons

We conducted three model comparisons to investigate model accuracy and assess model transferability (Figure 3). First, models were trained (empirical) or optimized (physically-based and hybrid) and validated individually for each study site (hereafter referred to as local models, Figure 3A). This setting corresponds to that of most local to regional scale studies in which field data of a specific area of interest are available. Second, the local models were applied to the field data of the other study sites to assess their transferability (hereafter referred to as transferred models, Figure 3B), simulating the case where a model trained or optimized for one area is applied to another area where no field data are available (domain shift). For the physically-based models, this means that the combination of cost function and percentage of solutions identified during local model optimization is transferred to the other study sites (i.e., the LUT remains unchanged). Third, models were trained or optimized with field data from four study sites and validated using the field data of the remaining site to examine any improvement in transferability (hereafter referred to as global models, Figure 3C). This mimics the case in which a diverse set of field data are available, for example from a compiled database, and used to make predictions for an area not covered by the database. Model transferability in such a setting is also referred to as the model's ability for domain generalization (Zhou et al., 2022). In addition, we compared epistemic uncertainties with model accuracies for all model comparisons where available – namely empirical GPR, physically-based, and hybrid models.

Model performance was assessed by coefficient of determination (R^2), relative root-mean-square errors (RRMSE) calculated as the RMSE divided by the mean value of the external testing set (Richter et al., 2012), and mean bias error (MBE) using the external testing set. In all cases, we used the ten Sentinel-2 bands in the visible and near-infrared (B2 – B8A) and the short-wave infrared regions (B11 – B12) as predictor variables with reflectance values being standardized for empirical and hybrid models and normalized, i.e., treating the spectra as probability distributions summing up to 1, for physically-based models (Rivera et al., 2013),

respectively. Accordingly, the models should be considered agnostic, meaning that apart from Sentinel-2 spectral data, no site-specific data were used for model training or prediction.

We note that due to comparatively small sample size (N=100), partitioning of the data into training or calibration and external testing set was repeated 10 times for the local and transferred models to account for stochastic effects (Muro et al., 2022). Correspondingly, local and transferred model performance of all model types were assessed by calculating both mean and SD for R^2, RRMSE, and MBE.

For the empirical models, the best-performing method was selected to be presented in the results as the focus lied on the comparison of model types and not different empirical models. Comprehensive cross-validation and testing performances for all models including additional performance metrics are enclosed in Appendix A Sections A.4 to A.16.

Lastly, the epistemic uncertainty of the local, transferred, and global models was compared to the absolute difference between measured and predicted biomass of the external testing set to test if epistemic uncertainty could potentially be used as an indicator of model transferability for heterogeneous grasslands. Further information about said relation for all models, including the individual repetitions of local and transferred models, is included in Appendix A Section A.17. We tested the relationship between absolute difference and epistemic uncertainty since it has been demonstrated that epistemic uncertainty of GPR models can serve as a *quality indicator* to identify reliable and unreliable predictions of transferred models for croplands, even when applied across spatial scales (Verrelst et al., 2013b, 2013a, 2012).

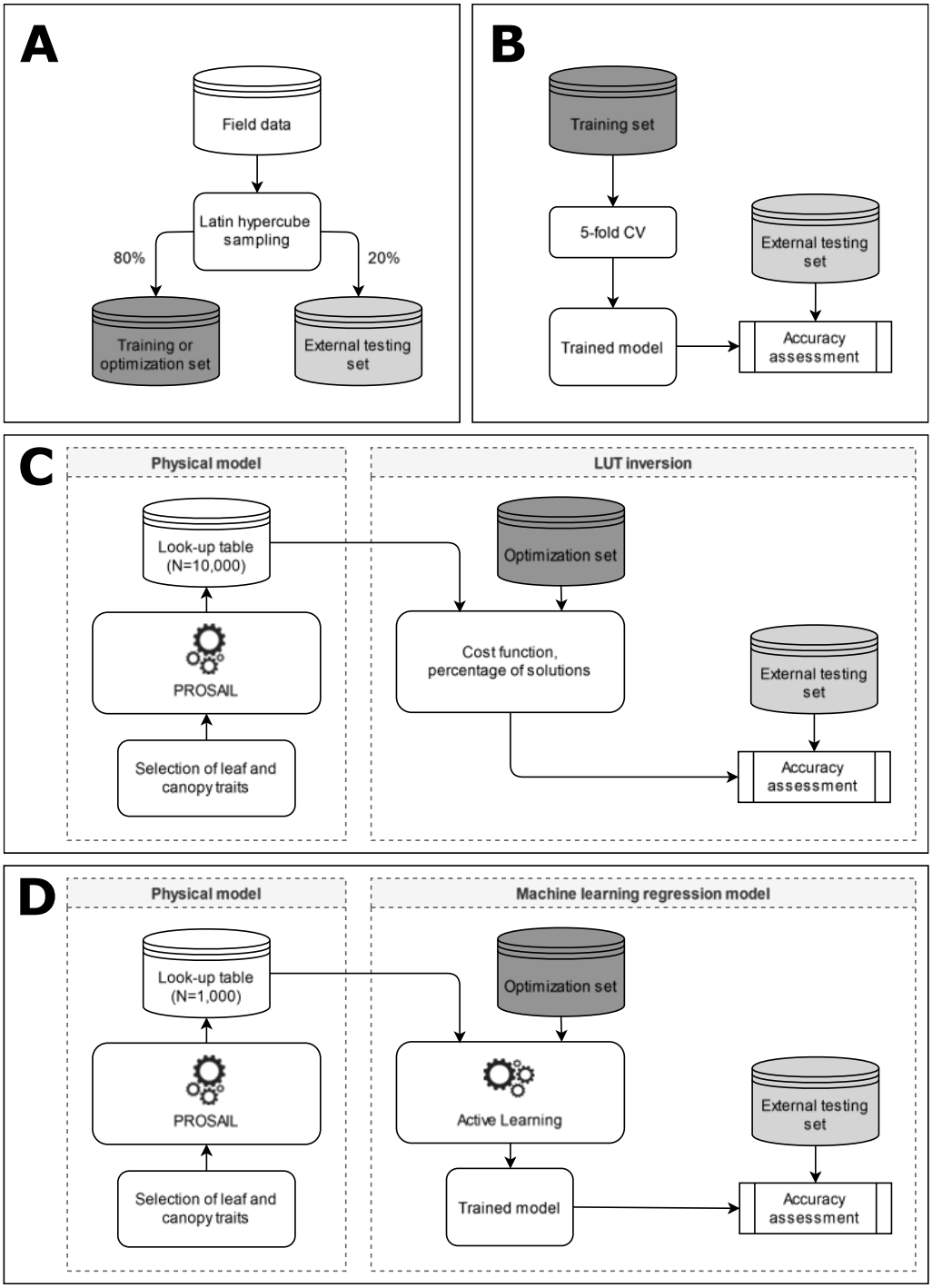

345

346 *Figure 2: Functioning of the models used in this study. A: As a prerequisite for all models, the field data need to be split into*
347 *training (in the case of empirical models) or optimization set (in case of physically-based and hybrid models; colored in dark*
348 *grey) and external testing set (colored in light grey) using Latin hypercube sampling. B: Empirical models are data-driven and*
349 *learn data-specific relationships between predictor variables. The 5-fold cross-validation (CV) was performed with each*
350 *possible combination of parameters listed in Table 2. C: Physically-based models use a radiative transfer model (RTM) such as*
351 *PROSAIL to simulate canopy reflectance spectra and a cost function is used to find a predefined number of best matches*
352 *between each field data point and the simulated spectra, a process commonly referred to as look-up table (LUT) inversion. D:*

Hybrid models are trained with a set of RTM-simulated spectra, which are optionally optimized using Active Learning. Subsequently, a machine learning regression model is used to perform the LUT inversion.

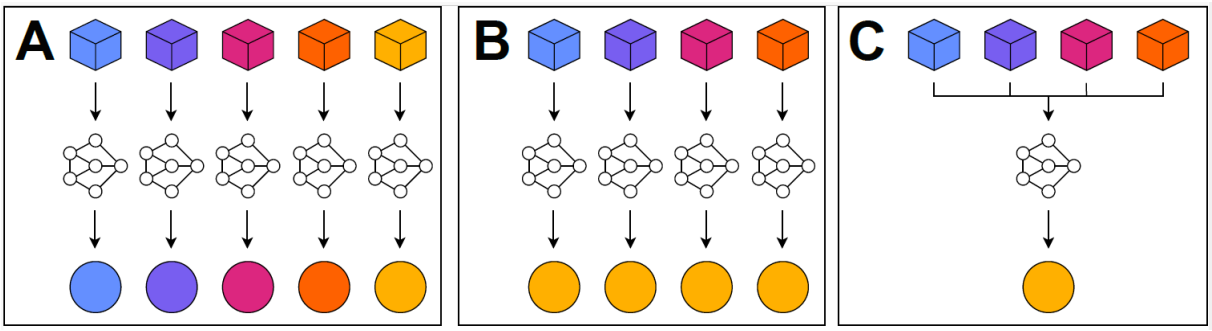

Figure 3: The three model comparisons conducted in this study. Cubes represent data used for training (of empirical models) or optimization (of physically-based and hybrid models). Circles represent data used for model validation. Colors represent data from different study sites. A: Local models with training/optimization and validation data from the same study site. B: Domain shift: transferred models with training/optimization and validation data from different study site (only one of five cases shown). C: Domain generalization: global models with training/optimization data from four sites and validation data from the remaining site (only one of five cases shown).

3. Results

3.1. Local models

The accuracy of all models varied with the study sites (Figure 4). For empirical models (Figure 4A-E), mean R^2 ranged from 0.31 to 0.64 (CH and HAI, respectively) and mean RRMSE from 0.22 to 0.55 (US and CH, respectively). Mean MBE indicated a systematic underestimation for all sites between -4.1 and -13.29 g/m^2 (HAI and CH, respectively) except for the US, for which a mean overestimation of 5.06 g/m^2 was observed. SVR outperformed the other empirical models for most sites, only the HAI site was best predicted by RFR.

For physically-based models (Figure 4F-J), mean R^2 ranged from 0.26 to 0.66 (CH and HAI, respectively) and mean RRMSE from 0.47 to 0.71 (SCH and US, respectively). For the ALB and HAI sites, a mean MBE of up to 42.64 g/m^2 was observed while on average, biomass was underestimated for CH and SCH. For the US model, a severe underestimation of -167.32 g/m^2 was reported. Compared to empirical models, model accuracy slightly decreased for most sites; for the US site it decreased substantially.

For hybrid models (Figure 4K-O), mean R^2 ranged from 0.23 to 0.54 (US and HAI, respectively) while mean RRMSE ranged from 0.29 to 0.64 (US and CH, respectively). Except for the US site, a slight underestimation in terms of MBE could be observed. Model accuracy across sites resembled those of empirical models, although they were again slightly lower.

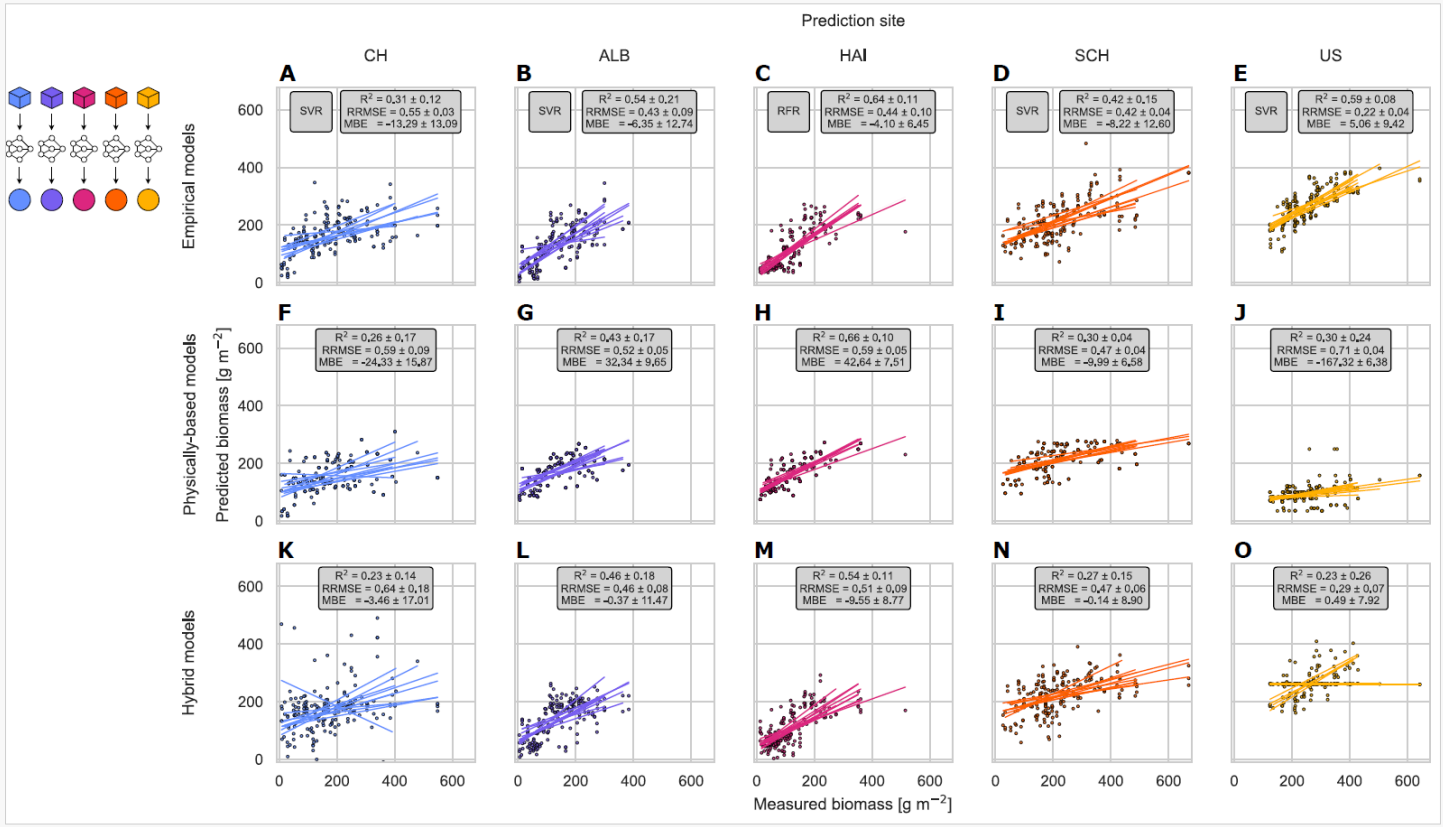

Figure 4: Scatterplots of measured versus predicted biomass for the local empirical (A-E), physically-based (F-J), and hybrid models (L-O). Textboxes show mean coefficient of determination (R^2), relative root-mean-square error (RRMSE) and mean bias error (MBE) ± 1 standard deviation across 10 repetitions for each model type. For empirical models, only the best-performing model in terms of lowest RRMSE is shown with the corresponding model name added in a separate textbox. CH: Switzerland (A, F, K), ALB: Schwäbische Alb (B, G, L), HAI: Hainich-Dün (C, H, M), SCH: Schorfheide-Chorin (D, I, N), US: United States (E, J, O), RFR: Random Forest regression, SVR: Support Vector regression.

3.2. Transferred models

In general, model accuracy decreased when local models were applied to other sites, although physical models sustained their predictive power the best (Table 4).

Out of all transferred empirical models, the accuracy of the CH models transferred to the SCH site (mean R^2 = 0.33, mean RRMSE = 0.49) and models transferred among the three German sites came closest to that of the local models, e.g., the ALB models predicting the HAI site (mean R^2 = 0.49, mean RRMSE = 0.54) or the HAI and SCH models predicting the ALB site (mean R^2 = 0.30, mean RRMSE = 0.53 and mean R^2 = 0.49, mean RRMSE = 0.64, respectively). For the CH site, only a mean R^2 of 0.15 with an associated mean RRMSE of 0.65 could be achieved by the transferred empirical model trained at the SCH site. For the US site, all transferred empirical models exhibited a systematic underestimation of the present biomass while the US models themselves overestimated biomass at other sites, e.g., with a mean MBE of 146.09 g/m^2 when predicting the HAI site.

Regarding physically-based models, transferability diverged less strongly between combinations of optimization and prediction sites, with the performance being best for the ALB, HAI, and SCH sites. Overall, variability between the 10 repetitions was comparatively low, as identical combinations of cost function and percentage of solutions were selected for the German sites (Appendix A Section A.5). Best results were achieved for the ALB site with the HAI models having performed similarly to the local models (mean R^2 = 0.43, mean RRMSE = 0.51). A slight decline in performance could be observed for the HAI site, although the ALB model still achieved a mean R^2 of 0.53 and a mean RRMSE of 0.66, with the decline for the SCH site being more pronounced. For the CH site, the models showed a lower mean R^2, but only a slightly higher mean RRMSE. For the US site, in contrast, a direct comparison with the local models was difficult; generally, a higher mean R^2 was achieved, but mean RRMSE and

systematic underestimation also increased. Moreover, the US models consistently performed worse for all other prediction sites. In comparison with transferred empirical models, the transferability of physically-based models was higher for the CH, ALB, and HAI sites.

The transferability of hybrid models also varied among different combinations of optimization and validation sites with best results for combinations of the German study sites such as the ALB models for the HAI site (mean $R^2 = 0.32$, mean RRMSE = 0.63) and vice versa (mean $R^2 = 0.34$, mean RRMSE = 0.52). The ALB models for the SCH site showed comparatively good values for mean R^2 and RRMSE, but with increased systematic underestimation. For the CH and US sites, no satisfactory performance could be achieved. Overall, the transferred hybrid models exhibited similar patterns to the empirical models, although their performance was somewhat lower. Particularly notable was the comparatively good performance among the German study sites and the systematic underestimation of biomass for the US site.

Table 4: Mean coefficient of determination (R^2), relative root-mean-square error (RRMSE), and mean bias error (MBE) for ± 1 standard deviation across 10 repetitions for the transferred empirical, physically-based, and hybrid models. To facilitate an estimation of model transferability, the metrics of the local models were included (in italic). For empirical models, only the best-performing model in terms of lowest RRMSE is shown with the corresponding model name added in brackets. CH: Switzerland, ALB: Schwäbische Alb, HAI: Hainich-Dün, SCH: Schorfheide-Chorin, US: United States, RFR: Random Forest regression, SVR: Support Vector regression, XGB: Extreme Gradient Boosting regression, GPR: Gaussian Process regression.

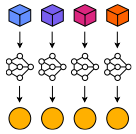		**Prediction site**														
		CH			**ALB**			**HAI**			**SCH**			**US**		
Model type	**Training/optimization site**	**R^2**	**RRMSE**	**MBE**	**R^2**	**RRMSE**	**MBE**	**R^2**	**RRMSE**	**MBE**	**R^2**	**RRMSE**	**MBE**	**R^2**	**RRMSE**	**MBE**
Empirical	**CH**	*0.31 ± 0.12 (SVR)*	*0.55 ± 0.03 (SVR)*	*-13.29 ± 13.09 (SVR)*	0.46 ± 0.12 (SVR)	0.70 ± 0.12 (SVR)	67.46 ± 23.94 (SVR)	0.39 ± 0.04 (SVR)	0.92 ± 0.15 (SVR)	77.08 ± 20.47 (SVR)	0.33 ± 0.08 (SVR)	0.49 ± 0.05 (SVR)	-14.42 ± 23.94 (SVR)	0.08 ± 0.05 (GPR)	0.48 ± 0.00 (GPR)	-88.80 ± 0.88 (GPR)
	ALB	0.04 ± 0.02 (GPR)	0.69 ± 0.00 (GPR)	-37.63 ± 0.98 (GPR)	*0.54 ± 0.21 (SVR)*	*0.43 ± 0.09 (SVR)*	*-6.35 ± 12.74 (SVR)*	0.49 ± 0.05 (SVR)	0.54 ± 0.02 (SVR)	-10.15 ± 5.00 (SVR)	0.30 ± 0.03 (XGB)	0.55 ± 0.01 (XGB)	-68.78 ± 3.22 (XGB)	0.04 ± 0.02 (GPR)	0.57 ± 0.00 (GPR)	-123.02 ± 0.86 (GPR)
	HAI	0.00 ± 0.01 (GPR)	0.73 ± 0.00 (GPR)	-62.02 ± 0.58 (GPR)	0.30 ± 0.03 (GPR)	0.53 ± 0.02 (GPR)	-13.74 ± 3.73 (GPR)	*0.64 ± 0.11 (RFR)*	*0.44 ± 0.10 (RFR)*	*-4.10 ± 6.45 (RFR)*	0.16 ± 0.03 (XGB)	0.63 ± 0.02 (XGB)	-83.11 ± 5.78 (XGB)	0.16 ± 0.04 (GPR)	0.65 ± 0.00 (GPR)	-146.93 ± 0.65 (GPR)
	SCH	0.15 ± 0.02 (RFR)	0.65 ± 0.03 (RFR)	22.32 ± 9.96 (RFR)	0.49 ± 0.04 (SVR)	0.64 ± 0.04 (SVR)	64.65 ± 7.68 (SVR)	0.48 ± 0.05 (SVR)	0.76 ± 0.05 (SVR)	62.53 ± 6.07 (SVR)	*0.42 ± 0.15 (SVR)*	*0.42 ± 0.04 (SVR)*	*-8.22 ± 12.60 (SVR)*	0.09 ± 0.03 (GPR)	0.36 ± 0.00 (GPR)	-39.81 ± 1.23 (GPR)
	US	0.01 ± 0.00 (GPR)	0.81 ± 0.00 (GPR)	87.98 ± 1.09 (GPR)	0.03 ± 0.01 (GPR)	1.07 ± 0.01 (GPR)	122.53 ± 1.11 (GPR)	0.02 ± 0.00 (GPR)	1.46 ± 0.01 (GPR)	146.09 ± 1.31 (GPR)	0.01 ± 0.00 (GPR)	0.57 ± 0.00 (GPR)	39.83 ± 1.14 (GPR)	*0.59 ± 0.08 (SVR)*	*0.22 ± 0.04 (SVR)*	*5.06 ± 9.42 (SVR)*
Physically-based	**CH**	*0.26 ± 0.17*	*0.59 ± 0.09*	*-24.33 ± 15.87*	0.41 ± 0.00	0.53 ± 0.00	34.97 ± 0.37	0.53 ± 0.00	0.69 ± 0.00	51.81 ± 0.23	0.21 ± 0.00	0.51 ± 0.00	-40.07 ± 0.25	0.45 ± 0.00	0.75 ± 0.01	-182.43 ± 1.66
	ALB	0.14 ± 0.00	0.61 ± 0.00	-24.61 ± 0.00	*0.43 ± 0.17*	*0.52 ± 0.05*	*32.34 ± 9.65*	0.53 ± 0.00	0.66 ± 0.00	45.83 ± 0.00	0.20 ± 0.00	0.53 ± 0.00	-45.64 ± 0.00	0.44 ± 0.00	0.75 ± 0.00	-182.09 ± 0.00
	HAI	0.14 ± 0.00	0.61 ± 0.00	-24.61 ± 0.00	0.43 ± 0.00	0.51 ± 0.00	29.33 ± 0.00	*0.66 ± 0.10*	*0.59 ± 0.05*	*42.64 ± 7.51*	0.20 ± 0.00	0.53 ± 0.00	-45.64 ± 0.00	0.44 ± 0.00	0.75 ± 0.00	-182.09 ± 0.00
	SCH	0.12 ± 0.00	0.60 ± 0.00	-3.44 ± 0.00	0.45 ± 0.00	0.63 ± 0.00	60.49 ± 0.00	0.50 ± 0.00	0.85 ± 0.00	77.44 ± 0.00	*0.30 ± 0.04*	*0.47 ± 0.04*	*-9.99 ± 6.58*	0.43 ± 0.00	0.71 ± 0.00	-170.48 ± 0.00
	US	0.13 ± 0.00	0.64 ± 0.04	-18.58 ± 7.28	0.22 ± 0.21	0.68 ± 0.07	19.05 ± 37.63	0.26 ± 0.23	0.84 ± 0.02	41.44 ± 31.11	0.12 ± 0.12	0.60 ± 0.13	-45.40 ± 31.62	*0.30 ± 0.24*	*0.71 ± 0.04*	*-167.32 ± 6.38*
Hybrid	**CH**	*0.23 ± 0.14*	*0.64 ± 0.18*	*-3.46 ± 17.01*	0.07 ± 0.07	0.88 ± 0.06	55.91 ± 19.27	0.03 ± 0.03	1.13 ± 0.11	70.71 ± 24.06	0.02 ± 0.02	0.64 ± 0.06	-44.35 ± 27.74	0.13 ± 0.10	0.70 ± 0.10	-148.09 ± 28.52
	ALB	0.02 ± 0.02	0.73 ± 0.05	-31.66 ± 21.59	*0.46 ± 0.18*	*0.46 ± 0.08*	*-0.37 ± 11.47*	0.32 ± 0.04	0.63 ± 0.01	0.42 ± 12.18	0.23 ± 0.04	0.58 ± 0.04	-75.77 ± 12.38	0.12 ± 0.10	0.62 ± 0.15	-132.65 ± 46.57
	HAI	0.02 ± 0.03	0.72 ± 0.06	-36.42 ± 18.12	0.34 ± 0.07	0.52 ± 0.03	-19.74 ± 5.34	*0.54 ± 0.11*	*0.51 ± 0.09*	*-9.55 ± 8.77*	0.17 ± 0.07	0.65 ± 0.03	-94.74 ± 5.45	0.14 ± 0.11	0.59 ± 0.04	-120.22 ± 12.54
	SCH	0.03 ± 0.03	0.79 ± 0.07	36.96 ± 48.54	0.41 ± 0.09	0.77 ± 0.06	83.55 ± 6.82	0.25 ± 0.06	0.95 ± 0.04	78.01 ± 6.21	*0.27 ± 0.15*	*0.47 ± 0.06*	*-0.14 ± 8.90*	0.19 ± 0.05	0.45 ± 0.09	-48.41 ± 44.96
	US	0.01 ± 0.01	0.94 ± 0.20	93.61 ± 20.14	0.03 ± 0.02	1.14 ± 0.20	117.33 ± 42.37	0.02 ± 0.03	1.55 ± 0.27	146.89 ± 38.34	0.02 ± 0.03	0.65 ± 0.12	39.24 ± 43.46	*0.23 ± 0.26*	*0.29 ± 0.07*	*0.49 ± 7.92*

3.3. Global models

For empirical models, accuracy was generally low (Figure 5A-E). It was highest for the ALB site, followed by the HAI and SCH sites, but accompanied by a high MBE. For the CH site, the R^2 of the prediction was practically 0.00, while the systematic underestimation for the US site amounted to -195.82 g/m^2. Comparatively poor results were also produced by the physically-based models in most cases (Figure 5F-J). An exception was the US site, for which an R^2 of 0.45 and an RRMSE of 0.75 were achieved. However, the systematic underestimation also tended to be high with an MBE of -183.99 g/m^2. Regarding hybrid models (Figure 5K-O), best results were obtained for the models predicting the ALB, HAI, and SCH sites, although the MBE indicated substantial over- and underestimations ranging from 37.30 for the ALB model to -79.07 g/m^2 for the SCH model, respectively. No satisfactory performance was achieved for the CH and US sites. Overall, the accuracy of global models was lower than for the local models (with the exception of the physically-based model for the US site, Figure 5K).

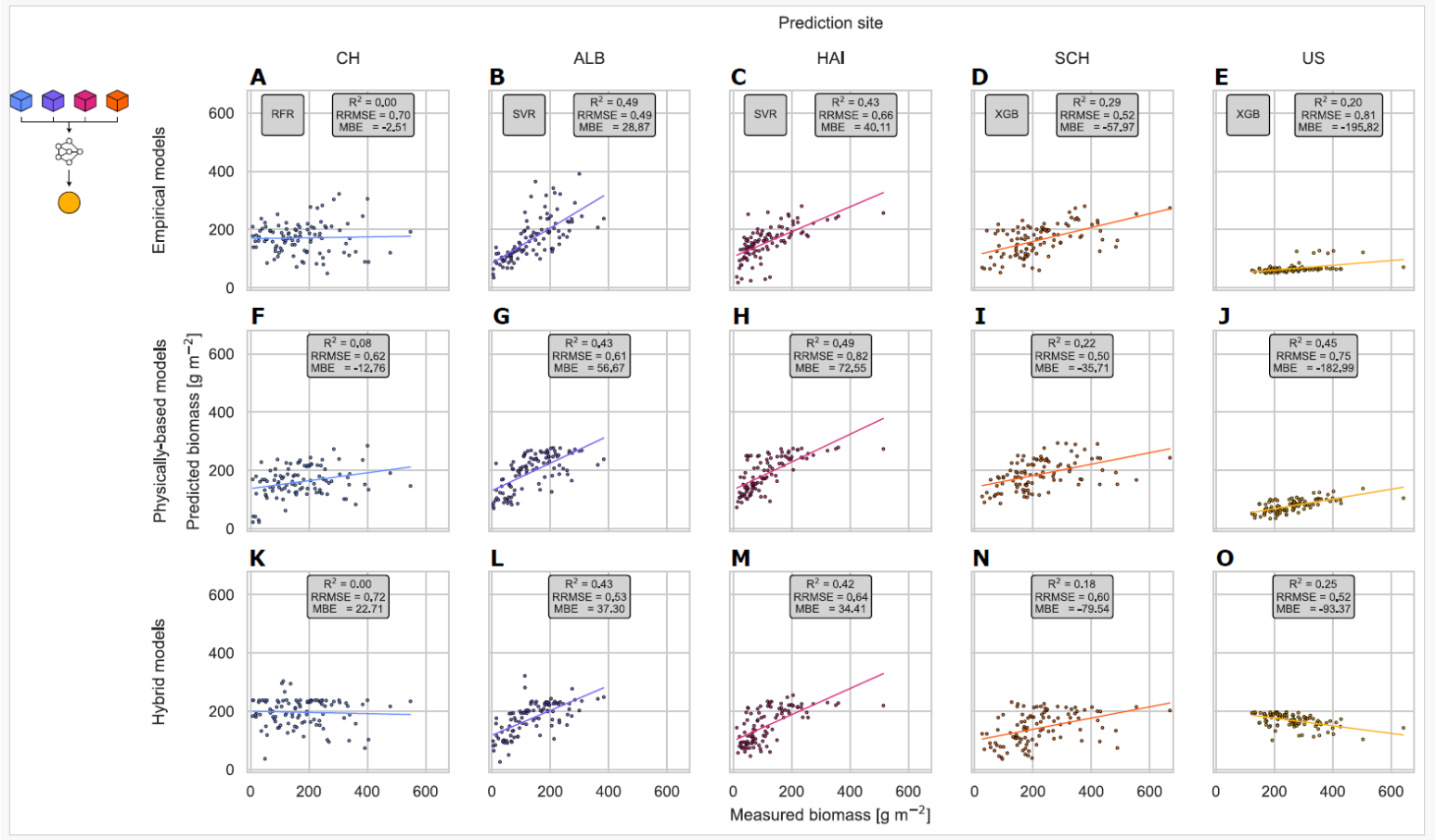

441

442 *Figure 5: Scatterplots of measured versus predicted biomass for the global empirical (A-E), physically-based (F-J), and hybrid models (L-O). Textboxes show coefficient of determination (R^2), relative*

443 *root-mean-square error (RRMSE) and mean bias error (MBE) for each model. For empirical models, only the best-performing model in terms of lowest RRMSE is shown with the corresponding model*

444 *name added in a separate textbox. CH: Switzerland (A, F, K), ALB: Schwäbische Alb (B, G, L), HAI: Hainich-Dün (C, H, M), SCH: Schorfheide-Chorin (D, I, N), US: United States (E, J, O), RFR: Random*

445 *Forest regression, SVR: Support Vector regression, XGB: Extreme Gradient Boosting regression.*

3.4. Epistemic uncertainty

For none of the comparisons (local, transferred, and global), a systematic relationship between epistemic uncertainty and absolute differences between measured and predicted biomass values was observed when considering all predicted data points (10 repetitions of 20 data points for local and transferred models, 100 data points for global models; Tables 5 and 6). Only isolated weak correlations were found, e.g., for local and transferred physically-based models predicting the US site (R^2 up to 0.31) or the global hybrid model predicting the US site (R^2 = 0.38).

Only for the mean values of epistemic uncertainty and absolute difference, a few patterns could be identified. Regarding the local empirical and hybrid models, a positive correlation between mean epistemic uncertainty and mean absolute difference could be observed. The lowest correlation values were found for the HAI site (for both model types) and the highest values for the SCH and CH sites (for empirical and hybrid models, respectively). The physically-based models displayed a negative correlation; the US site exhibited the lowest mean epistemic uncertainty but the highest mean absolute difference (52.71 and 162.16 g/m^2, respectively).

For the transferred models, a clear pattern between combinations of training or optimization and prediction site was found. The respective empirical and hybrid models of the ALB and HAI sites exhibited low values for both mean epistemic uncertainty and absolute difference for mutual prediction. The highest values for mean epistemic uncertainty and absolute difference were produced by the CH and US models of both model types. For the transferred physically-based models, the lowest values for mean epistemic uncertainty were observed for the US site (38.86 g/m^2 for ALB and HAI models), which did not coincide with the high values for mean absolute difference (182.09 g/m^2 for ALB and HAI models). For the global models, no agreement between mean epistemic uncertainty and mean absolute difference was found for any model type or prediction site.

Table 5: Mean difference between predicted and measured grassland biomass and epistemic uncertainty ± 1 standard deviation and coefficient of determination (R^2) for the 10 local (in italic) and local transferred models. For the local models, 200 samples (10 predictions of 20 samples each) and for the transferred models, 1000 samples (10 predictions of 100 samples each) were available. If the percentage of solutions of a given physically-based model was 0.01%, only 1 solution was used to derive the predicted biomass value and no epistemic uncertainty could be calculated for the corresponding predicted samples (see Appendix A Section A.5). The absolute difference was calculated by taking the absolute value after subtracting the measured biomass value from the predicted biomass value for each predicted sample. For the empirical and hybrid models, the epistemic uncertainty for a predicted sample corresponds to the predicted standard deviation of the Gaussian process regression (GPR) models. For the physically-based models, the epistemic uncertainty corresponds to the standard deviation of all selected solutions. CH: Switzerland, ALB: Schwäbische Alb, HAI: Hainich-Dün, SCH: Schorfheide-Chorin, US: United States.

		Prediction site														
		CH			**ALB**			**HAI**			**SCH**			**US**		
Model type	**Training/optimization site**	**Absolute difference [g m^{-2}]**	**Epistemic uncertainty [g m^{-2}]**	**R^2**	**Absolute difference [g m^{-2}]**	**Epistemic uncertainty [g m^{-2}]**	**R^2**	**Absolute difference [g m^{-2}]**	**Epistemic uncertainty [g m^{-2}]**	**R^2**	**Absolute difference [g m^{-2}]**	**Epistemic uncertainty [g m^{-2}]**	**R^2**	**Absolute difference [g m^{-2}]**	**Epistemic uncertainty [g m^{-2}]**	**R^2**
Empirical	**CH**	*83.69 ± 74.12*	*94.67 ± 21.25*	*0.08*	98.15 ± 71.22	108.78 ± 11.78	0.18	119.89 ± 72.50	109.00 ± 10.10	0.19	101.10 ± 82.35	111.90 ± 8.79	0.02	94.41 ± 81.49	116.21 ± 3.83	0.03
	ALB	90.79 ± 77.02	82.00 ± 3.57	0.10	*55.08 ± 41.92*	*64.64 ± 14.89*	*0.01*	53.80 ± 48.66	70.18 ± 12.51	0.05	96.30 ± 90.96	69.07 ± 11.85	0.00	123.80 ± 84.85	82.86 ± 1.06	0.00
	HAI	96.51 ± 83.30	87.96 ± 7.87	0.03	58.07 ± 44.78	65.96 ± 16.17	0.02	*41.89 ± 43.50*	*57.10 ± 17.38*	*0.03*	102.05 ± 95.57	65.59 ± 15.87	0.07	146.93 ± 86.94	89.98 ± 6.35	0.00
	SCH	100.43 ± 66.40	123.63 ± 5.15	0.00	100.29 ± 62.11	111.75 ± 14.43	0.05	105.34 ± 57.31	111.95 ± 13.54	0.13	*86.17 ± 76.45*	*110.94 ± 14.80*	*0.02*	69.60 ± 64.11	123.97 ± 5.05	0.00
	US	120.43 ± 73.51	96.99 ± 7.78	0.00	129.78 ± 73.50	96.99 ± 7.78	0.00	156.39 ± 65.59	96.98 ± 7.78	0.00	104.73 ± 69.81	96.99 ± 7.78	0.00	*54.01 ± 48.06*	*66.35 ± 19.96*	*0.01*
Physically-based	**CH**	*72.56 ± 74.38*	*72.64 ± 28.22*	*0.02*	64.22 ± 37.31	90.64 ± 25.47	0.00	68.23 ± 41.77	87.73 ± 24.39	0.01	80.90 ± 80.60	95.65 ± 21.07	0.04	182.43 ± 73.30	40.22 ± 11.08	0.20
	ALB	76.45 ± 72.35	71.98 ± 24.64	0.01	*63.10 ± 37.78*	*88.68 ± 25.09*	*0.00*	64.28 ± 41.40	84.10 ± 24.24	0.02	81.28 ± 83.70	92.55 ± 20.37	0.03	182.09 ± 73.19	38.86 ± 10.85	0.21
	HAI	76.45 ± 72.35	71.98 ± 24.64	0.01	60.97 ± 36.65	86.64 ± 25.29	0.00	*59.18 ± 34.42*	*81.59 ± 25.56*	*0.00*	81.28 ± 83.70	92.55 ± 20.37	0.03	182.09 ± 73.19	38.86 ± 10.85	0.21
	SCH	79.70 ± 67.66	95.62 ± 24.64	0.01	76.02 ± 43.42	103.37 ± 27.38	0.04	87.85 ± 44.65	101.54 ± 24.53	0.05	*76.14 ± 71.71*	*109.97 ± 19.35*	*0.02*	170.48 ± 70.77	51.96 ± 15.66	0.17
	US	77.93 ± 69.49	85.86 ± 26.66	0.01	74.45 ± 42.24	100.68 ± 28.68	0.03	83.05 ± 46.07	97.41 ± 27.84	0.07	77.86 ± 71.21	107.35 ± 23.30	0.03	*162.16 ± 64.37*	*52.71 ± 8.87*	*0.31*
Hybrid	**CH**	*85.15 ± 79.45*	*168.42 ± 64.24*	*0.02*	100.74 ± 69.41	116.83 ± 57.08	0.10	113.54 ± 67.88	84.32 ± 47.26	0.00	109.92 ± 92.14	102.34 ± 55.32	0.02	151.07 ± 108.91	152.27 ± 53.92	0.19
	ALB	96.76 ± 82.75	127.65 ± 34.26	0.03	*49.07 ± 43.37*	*100.59 ± 38.06*	*0.00*	52.49 ± 50.49	76.32 ± 33.13	0.04	96.64 ± 86.68	84.99 ± 36.44	0.06	137.02 ± 92.86	129.28 ± 28.89	0.25
	HAI	94.79 ± 82.74	130.98 ± 27.94	0.03	52.71 ± 49.66	101.47 ± 30.03	0.00	*41.62 ± 42.70*	*83.56 ± 29.03*	*0.01*	106.33 ± 98.54	89.19 ± 31.22	0.07	124.46 ± 93.54	135.26 ± 23.55	0.17
	SCH	111.38 ± 80.29	138.79 ± 41.65	0.00	93.55 ± 52.99	109.98 ± 42.53	0.00	92.91 ± 59.13	87.59 ± 43.11	0.05	*79.79 ± 68.74*	*100.39 ± 44.62*	*0.08*	92.30 ± 77.51	144.42 ± 34.61	0.17
	US	135.55 ± 98.87	137.77 ± 47.69	0.01	135.62 ± 86.92	120.75 ± 38.63	0.04	163.14 ± 82.09	107.63 ± 33.42	0.00	118.59 ± 85.61	112.79 ± 36.61	0.00	*58.76 ± 53.06*	*135.36 ± 38.89*	*0.04*

Table 6: Mean difference between predicted and measured grassland biomass and epistemic uncertainty ± 1 standard deviation and coefficient of determination (R^2) for global models. For each model, 100 samples (1 prediction of 100 samples each) were available. The absolute difference was calculated by taking the absolute value after subtracting the measured biomass value from the predicted biomass value for each predicted sample. For the empirical and hybrid models, the epistemic uncertainty for a predicted sample corresponds to the predicted standard deviation of the Gaussian process regression (GPR) models. For the physically-based models, the epistemic uncertainty corresponds to the standard deviation of all selected solutions. CH: Switzerland, ALB: Schwäbische Alb, HAI: Hainich-Dün, SCH: Schorfheide-Chorin, US: United States.

	Prediction site														
	CH			**ALB**			**HAI**			**SCH**			**US**		
Model type	**Absolute difference [g m^{-2}]**	**Epistemic uncertainty [g m^{-2}]**	**R^2**	**Absolute difference [g m^{-2}]**	**Epistemic uncertainty [g m^{-2}]**	**R^2**	**Absolute difference [g m^{-2}]**	**Epistemic uncertainty [g m^{-2}]**	**R^2**	**Absolute difference [g m^{-2}]**	**Epistemic uncertainty [g m^{-2}]**	**R^2**	**Absolute difference [g m^{-2}]**	**Epistemic uncertainty [g m^{-2}]**	**R^2**
Empirical	89.36 ± 65.55	112.11 ± 0.00	0.00	83.81 ± 55.91	115.07 ± 0.00	0.00	105.16 ± 56.70	111.4 ± 0.00	0.00	92.12 ± 90.44	107.64 ± 0.00	0.00	102.31 ± 81.66	108.8 ± 0.00	0.00
Physically-based	81.37 ± 71.47	83.49 ± 27.37	0.00	74.45 ± 42.24	100.68 ± 28.68	0.03	83.05 ± 46.07	97.41 ± 27.84	0.07	78.35 ± 79.36	94.48 ± 21.91	0.01	182.99 ± 73.17	39.74 ± 11.05	0.20
Hybrid	98.72 ± 75.78	138.74 ± 25.66	0.01	62.54 ± 40.14	138.67 ± 51.71	0.03	57.72 ± 45.84	88.45 ± 24.39	0.14	97.38 ± 92.43	106.99 ± 34.61	0.11	101.97 ± 90.03	132.54 ± 7.63	0.38

4. Discussion

Remote sensing has gained traction in its application for monitoring ecosystem functioning, with spatial (and temporal) scalability often highlighted as a key advantage. When developing scalable models, model transferability should be an integral part of performance assessment; however, systematic evaluation often lags behind the ambition for scalability within and across ecosystems. In this study, we demonstrated the importance of assessing model transferability when evaluating the performance of remotely sensed grassland biomass estimates and related model selection considerations. Our model comparisons indicated that in most cases physically-based models exhibited the highest transferability when applied to unseen grassland sites. However, no single model consistently outperformed others when trained or optimized with data from multiple sites. These results underscore the challenges in developing scalable models, highlight the importance and possible trade-offs of appropriate model selection, and shed light on the discrepancies between epistemic uncertainty and predictive accuracy.

4.1. Accuracy of local models

All model types performed similarly when predicting biomass locally with accuracies comparable to those of other studies conducted in alpine and semi-natural grasslands in Switzerland and Germany (Raab et al., 2020; Schweiger et al., 2015a). Generally, model accuracy decreased with increasing biomass range and (to a lesser extent) spectral variability (see also Dehghan-Shoar et al., 2023, Figure 1, and Appendix A Section A.18). Overall, empirical models performed best at the site level, presumably due to their high flexibility, allowing them to incorporate site-specific relationships in the data without necessarily relying on physical principles.

507 For the physical models, we found a large discrepancy between the *in situ* and modeled data
508 for the US site caused by the employed LUT parametrization. Although the models recognized
509 the underlying relationship between biomass and spectral information to a certain extent (mean
510 $R^2 = 0.30$), a high RRMSE of 0.71 resulted probably due to a too narrow range of values for
511 LMA in the LUT since testing an alternative value range with a higher upper bound for LMA
512 resulted in a mean R^2 of 0.51 and mean RRMSE of 0.33 (Appendix A Section A.19). An
513 evaluation of the agreement between the PROSAIL simulations and Sentinel-2 spectra of the
514 different study sites as an indicator of the respective PROSAIL forward mode fit quality can be
515 found in Appendix A Section A.20. However, broadening the trait ranges increased ill-
516 posedness (Combal et al., 2003; Verrelst et al., 2014) and deteriorated model performance for
517 the other sites; therefore, a site-specific parametrization of multiple narrowly defined LUTs
518 would be necessary to obtain comparable results to the empirical models for all sites.

519 The hybrid models performed similarly compared to the empirical models. Selecting training
520 samples with AL led to substantial improvements in performance as stated in AL theory
521 (Verrelst et al., 2016). In our case, the use of AL for selecting the most informative optimization
522 samples was essential because we did not parameterize the LUT *a priori* or excluded
523 biophysically unrealistic simulations as done by others (see, e.g., Campos-Taberner et al.,
524 2018). Moreover, the hybrid models did not display the aforementioned imbalance between R^2
525 and RRMSE for the US site although having been trained on a suboptimally configured LUT,
526 presumably because the employed GPR kernel was able to scale the predictions by the
527 magnitude of the employed constant kernel resulting in a lower RRMSE compared to the
528 physically-based models while keeping R^2 comparatively high (scikit-learn Developers, 2023).

529 The fact that local models in grasslands sometimes underperform compared to croplands is
530 largely due to the specific particularities of grassland systems. Grasslands often contain a
531 complex mixture of photosynthetic and non-photosynthetic vegetation, with litter potentially

532 contributing a substantial fraction of total biomass (Schweiger et al., 2015a). Contrasting
533 absorption and scattering properties of litter compared to green biomass can reduce the
534 sensitivity of reflectance-based predictors to total biomass. High species and trait diversity of
535 grasslands is reflected in heterogeneous canopy architectures that violate the homogeneity
536 assumptions underlying radiative transfer models such as PROSAIL (Rossi et al., 2020). In
537 addition, strong fine-scale spatial heterogeneity driven by grazing by wild and domestic
538 herbivores further confounds the link between plot-scale measurements and satellite-based
539 observations.

540 4.2. Transferability of local models

541 Several factors possibly hampered model transferability. First, the transferability of empirical
542 and hybrid models remained limited to combinations of training or optimization and validation
543 sites sharing similar environmental and management characteristics such as ALB and HAI. This
544 is consistent with the findings of Muro et al. (2022) who, among the German study sites, found
545 the prediction of SCH to be the most challenging due to an elevated level of soil organic content
546 and different management compared to ALB and HAI (Busch et al., 2018). At the other
547 extreme, the US site, which was poorly predicted by transferred models, was sampled during a
548 very dry summer, and the Sentinel-2 spectra showed a substantial increase in reflectance in the
549 short-wave infrared region, likely due to low water content confounding the overall spectra
550 (Jacquemoud et al., 2009; Mesonet, 2024; Appendix A Section A.21). The summer drought
551 may have also led to early senescence, resulting in a potential underestimation of LAI in
552 PROSAIL as the latter is predominantly equipped for modelling green vegetation and struggles
553 to capture NPV (Amin et al., 2021; Delegido et al., 2015; Schiefer et al., 2021; Verrelst et al.,
554 2023). Second, differences in the abundance of C3 and C4 grasses among sites may have further
555 limited model transferability from European sites to the US exhibiting a substantially higher
556 cover fraction of C4 grasses (Kothari and Schweiger, 2022; Shoko et al., 2016; Appendix A

Section A.22). Third, the derivation of biomass values in physically-based and hybrid approaches via LUT-based LMA and LAI multiplication resulted in numerous parameter combinations associated with the same biomass values, increasing the prevalent ill-posedness of the model. Fourth, plot definition and field measurements were handled differently among the study sites and field campaigns. For example, the plots being monitored by the Biodiversity Exploratories were selected to be representative of an area of 2,500 m^2 and biomass was cut for an area of 2 m^2 (Hinderling et al., 2023), whereas the plots in Switzerland were representative for an area of 36 m^2 and biomass harvesting was limited to 1 m^2 (Schweiger et al., 2015b). While such discrepancies between monitoring programs are likely to introduce uncertainties, they are difficult to mitigate when working with already existing field data. Moreover, the *in situ* data collection might not necessarily have been optimized for the pixel grid of the utilized remote sensing data, e.g., 20 × 20 m grid for Sentinel-2, leading to the problem of diminished representativeness (Hauser et al., 2021b; Schweiger, 2020) such as in the case of mixed pixels. Even though standardization of field campaigns could potentially benefit the transferability of model trained with remote sensing data, it might be hardly feasible due to ecological or policy constraints and the legitimate interest of existing monitoring programs to ensure temporally consistent measurements.

Nevertheless, physically-based models outperformed empirical and hybrid models when predicting novel study sites in an agnostic scenario which is consistent with the claimed transferability of physically-based models and the results of previous studies conducted at leaf level (Féret et al., 2019; Verrelst et al., 2015; Wang et al., 2023). For the hybrid models, we expected a comparatively high transferability due to the physical foundation of the RTM-simulated training data. In addition, previous studies have shown the general ability of machine learning regression models to serve as RTM emulators, i.e., being able to accurately grasp the physical principles of RTMs during model training (Rivera et al., 2015; Verrelst et al., 2017).

However, our results showed that the transferability of the hybrid models was weakest in most cases, potentially because the empirical features of hybrid models overrode the physical foundation of the training data by fitting data-specific single-trait relationships between the AL-selected training set and the optimization data. To increase the transferability of hybrid models, it has been suggested to increase the initial training set size (Berger et al., 2021b; Tagliabue et al., 2022), enforcing the inclusion of more general training data prior to the employment of AL. However, no general increase in transferability was apparent in our results even when using different initial training set sizes (Appendix A Section A.23).

4.3. Accuracy of global models

In this study, global models were defined as models that were trained (empirical) or optimized (physically-based and hybrid) using field data from multiple sites and applied to an unseen prediction site. The reasoning behind this model set-up was that model training or optimization with heterogeneous field data might increase model transferability by allowing the model to learn from a larger pool of diverse field data motivated by previous studies employing similar approaches (Muro et al., 2022) and the emergence of global plant trait products derived from remote sensing data using physically-based or machine learning models (Campos-Taberner et al., 2018; Kovács et al., 2023; Moreno-Martinez et al., 2020) relying on accurate predictions for unsampled areas. The results of this third model comparison were not conclusive as to which model performed best at this task.

The global physically-based models achieved lower accuracy than the local models for all sites, indicating a strong influence of the selected combinations of cost function and percentage of solutions, which differed strongly from those of the local models (Appendix A Sections A.5 and A.8). This seems to contradict the observed higher transferability of the transferred physically-based models and the eventual conclusion that physically-based models are always the best choice if no validation data is available (see Section 4.2).

607 One major challenge for global empirical and hybrid models was that different confounding
608 relationships between biomass and spectral information are possible for various study sites.
609 This was reflected for the empirical and hybrid models by the increased mean RRMSE of the
610 US site, whose specific conditions could not be adequately learned by the models without
611 additional contextual information (in the case of the global physically-based models, the reason
612 for the high mean RRMSE was most likely the parametrization of the LUT as discussed in 4.1).
613 Nevertheless, comparatively good results were obtained by the empirical models for the ALB
614 site (R^2 = 0.49, RRMSE = 0.49, MBE = 28.87 g/m^2) and by the hybrid models for the ALB (R^2
615 = 0.43, RRMSE = 0.53, MBE = 37.30 g/m^2) and HAI sites (R^2 = 0.42, RRMSE = 0.64, MBE =
616 34.41 g/m^2) which is consistent with the results of Muro et al. (2022) who reported a lower
617 transferability of models applied to the SCH site due to confounding factors such as soil organic
618 content and management practices (Busch et al., 2018). Identifying the exact factors
619 contributing to the divergent performance is challenging within the multi-site training set-up
620 and limits definitive conclusions to be drawn on model selection and suitability.

621 4.4. Prediction uncertainty as a measure of model applicability to unseen data

622 Value and acceptance of remote sensing products increase with a quantitative specification of
623 uncertainty (Woodcock, 2002); increased attention to uncertainty is also called for in the context
624 of machine learning applications (Meyer and Pebesma, 2020). Motivated by the finding that
625 epistemic uncertainty of GPR models might help to identify reliable and unreliable predictions
626 for croplands (Verrelst et al., 2013b, 2013a, 2012), we tested if epistemic uncertainty could be
627 used as proxy for model transferability across heterogeneous grasslands by comparing the
628 absolute difference between measured and predicted biomass with the epistemic uncertainty
629 associated with each prediction and found low correspondence between the two (as shown in
630 Section 3.4).

In the case of GPR, epistemic uncertainty is a direct model output in the form of the predictive SD. According to Rasmussen and Williams (2006), the epistemic uncertainty of GPR models is determined by the similarity between a data point to be predicted and the training data as well as the properties of the optimized kernel, e.g., the magnitude of the constant kernel and the lengthscale of the RBF kernel. Accordingly, it is not surprising that the empirical models for the mutual prediction of the spectrally more similar ALB and HAI sites showed lower mean epistemic uncertainty than the US models, whose training data exhibited different spectral properties, e.g., the high reflectance in the short-wave infrared region for the US site. The fact that the AL-selected training data of the hybrid models did not differ much among the study sites (Appendix A Section A.24) led to a consistently lower epistemic uncertainty for the German sites, for which the spectral properties of the field data were more similar to those of the AL-selected training data. Correspondingly, a high mean epistemic uncertainty resulted for the CH and US sites, since these sites exhibited larger spectral heterogeneity (as shown in Appendix A Section A.18) or contained spectra that were not fully covered by the current parametrization of the PROSAIL LUT, respectively. Thus, a high epistemic uncertainty indicated that the data points to be predicted are not optimally covered by the training data, while a low epistemic uncertainty on the contrary did not necessarily indicate a reliable prediction as suggested by the missing correspondence between low absolute differences and associated epistemic uncertainty. Hence, using the epistemic uncertainty as a measure of model applicability to unseen data might be valid only in the case of comparable relationships between biomass and spectral information – a condition violated in our study. Nevertheless, the GPR uncertainty still serves as valuable information to optimize field sampling efforts as outlined in Verrelst et al. (2012).

In the case of physically-based models, the SD of the solutions considered in the LUT inversion process is a comparatively simple approach to express the variability of the candidate solutions

656 and thus to quantify the diversity of the possible solutions. This diversity was relatively
657 consistent per prediction site, e.g., mean epistemic uncertainty was between 38.86 and 51.96
658 g/m^2 for predictions of the US site, suggesting a subordinate influence of the cost functions and
659 percentages of solutions used for different LUT inversions. Rather, the epistemic uncertainty
660 appeared to depend primarily on the spectral properties of the predicted data. For example, the
661 US site had by far the lowest epistemic uncertainty, which was not consistent with the
662 comparatively high mean RRMSE. In fact, a more accurate prediction of the US site would
663 have required a modification of the LUT parameterization (as shown in Appendix A Section
664 A.19), which is obscured by relying solely on the prediction uncertainty. Therefore, in our
665 study, the epistemic uncertainty expressed as diversity of the possible solutions did not allow a
666 direct conclusion on the applicability of the models to unseen data.

667 ### 4.5. Possible improvements

668 Regarding the performance of local models, various opportunities for improvement are
669 conceivable depending on the model type. First, the use of alternative algorithms or cost
670 functions should be considered. For empirical models, alternative algorithms such as Artificial
671 Neural Networks (ANNs) as employed by Ali et al. (2017) and Muro et al. (2022) could be
672 tested to determine further improvements in model accuracy. For the physically-based models,
673 the cost functions discussed by Rivera et al. (2013) were tested but since the choice of the
674 optimal cost functions varied between study sites, the inclusion of additional cost functions
675 such as genetic algorithms (Fang et al., 2003) could benefit the accuracy of the LUT inversion.
676 Second, subsetting the LUT using correlations between PROSAIL input parameters could
677 reduce solution space (Campos-Taberner et al., 2018). For this, *in situ* data of several PROSAIL
678 input parameters are necessary whose correlations could be exploited to prevent unrealistic
679 parameter combinations being included in the LUT (Combal et al., 2003) as done by Schiefer
680 et al. (2021). Ideally, the *in situ* data should be collected for each study site, since the correlation

between the parameters is subject to environmental gradients such as climatic and soil factors (Joswig et al., 2021), laying the foundation for a locally informed scenario. In such a scenario, further variables besides the aforementioned LMA (see Section 4.1) could have played a key role in increasing the representativeness of the simulated LUT for site-specific conditions. On the one hand, Berger et al. (2021a) and Verrelst et al. (2023) have shown that NPV can be modeled by coupling PROSPECT-PRO (Féret et al., 2021), the successor model to PROSPECT-D, with 4SAIL by combining carbon-based constituents (CBC) and LAI. The approximation of NPV would allow the local ratio of green and brown vegetation to be better represented. On the other hand, the default spectra for dry and wet soil of the prosail R package could be replaced by locally measured spectra or spectra contained in a spectral library in order to take their spatial variability into account. Using existing soil spectral libraries (Safanelli et al., 2025; Viscarra Rossel et al., 2016), the default spectra used for the PROSAIL simulation could be replaced by spectra tailored to local soil properties. Third, the inclusion of additional predictor variables could improve model accuracy and transferability, for example additional biomass-relevant variables such as vegetation height could lead to improved predictions. However, sampling of additional variables is time- and labor-intensive and deriving them from remote sensing data is challenging, highlighting the need for reliable, accurate, and transferable remote sensing models. For example, the mean average error (MAE) of the estimated canopy height from spaceborne laser altimeters amounts to at least 2 m (Liu et al., 2021) and the use of Sentinel-1 SAR data has led to mixed results, ranging from improving grassland biomass estimation to providing little or no added value when combined with optical data (Muro et al., 2022; Raab et al., 2020; Wang et al., 2019). For hybrid models, it is possible to employ further advanced models such as multi-output GPR models (MOGPs) if additional *in situ* measured PROSAIL parameters are available, which allow to predict multiple output variables while preserving the correlations among the input variables (Liu et al., 2018). The feasibility of employing MOGPs in the context of biophysical variable estimation has already been

707 demonstrated by Pipia et al. (2019) and Caballero et al. (2023) who predicted LAI and
708 vegetation water content (VWC), respectively, by combining Sentinel-1 and Sentinel-2 data.

709 To improve the local models' transferability as well as the global models' accuracy, it is
710 essential to disentangle the site-specific confounded relationships between biomass and spectral
711 information, effectively shifting from agnostic to locally informed biomass models. First,
712 additional predictor variables could help to distinguish these relationships, including vegetation
713 height, climate data, land use intensity as continuous proxy for management information
714 (Blüthgen et al., 2012; Rossi et al., 2024), evapotranspiration, and the quantification of NPV.
715 Second, a stratification based on climatic priors for subsequent LUT optimization would be
716 useful in the context of diverse study sites and resonates with studies making the case for a
717 stronger embedding of remote sensing data with ancillary data (Aguirre-Gutiérrez et al., 2021;
718 Cavender-Bares et al., 2022; Moreno-Martinez et al., 2020; Verrelst et al., 2023). Although a
719 remote sensing-only solution may have been desirable, our results reaffirm, through a new
720 perspective, the trade-off between a LUT parametrization covering the ecological conditions of
721 all sites and a degradation of the LUT inversion accuracy. Such a stratification would allow, in
722 the first step, the data points to be projected into different environmental regimes based on
723 climate data and in the second step, to use LUTs subsetted based on correlations between
724 PROSAIL parameters and with optimized parameter ranges for the physically-based or hybrid
725 models. While coarse-resolution climate data for the first step are freely available over large
726 spatial scales (e.g., ERA5-Land; Muñoz Sabater, 2019), the second step still places high
727 demand on the availability of *in situ* data.

Conclusion

In this study, we compared different models for biomass estimation from multispectral spaceborne remote sensing data across heterogeneous grasslands to assess model assumptions and facilitate model choice for specific applications. In three model comparisons, we investigated the accuracy and transferability of empirical, physically-based, and hybrid models across five study sites regarding (1) their local applicability, (2) their spatial transferability, and (3) the opportunity to compile field data from multiple study sites to increase transferability. Our results showed that:

1) on the local level, all models performed similarly well in terms of RRMSE and R^2. Further, we found that in the context of hybrid models, employing AL to identify the most informative training samples was required.
2) when transferring local models to a different study site, the physically-based models led to the most promising results for most combinations of training (empirical models) or optimization (physically-based and hybrid models) and validation sites. Moreover, we observed a trade-off between LUT specificity and generality, impeding the universal application of a single physically-based model. The transferability of empirical and hybrid models was limited to combinations of sites sharing similar ecological and/or spectral conditions.
3) when compiling the field data of four study sites to predict the remaining one, no model clearly outperformed the others. Differences in model performance remained challenging to explain, highlighting the need to further explore the possibilities and characterize the trade-offs of developing models applicable on a large spatial scale and across ecological gradients.
4) common epistemic uncertainty implementations were not necessarily reliable measures of model applicability to unseen data in the case of varying relationships between

biomass and spectral information across study sites. While high epistemic uncertainty indicates suboptimal coverage of the data points to be predicted by the training data and can therefore guide future sampling efforts, low epistemic uncertainty does not necessarily indicate high prediction accuracy.

5) model transferability needs to be thoroughly tested when developing remote sensing applications whose intended applicability goes beyond the local scale.

Possibilities for improving local model accuracy and transferability include the testing of alternative machine and deep learning algorithms and cost functions, hierarchical subsetting of LUTs based on ecological priors, and the use of multi-output models to preserve correlations among predictor variables, incorporating additional predictors such as NPV or climate data, and exploring multi-sensor approaches. To fully exploit the spatio-temporal potential of satellite observations, evaluating and improving model transferability should be a priority; this requires datasets that enable rigorous testing across sites and conditions, along with theory-driven foundations to build models capable of robust prediction when applied to new unseen data.

CRediT authorship contribution statement

Jan Schweizer: Conceptualization, Methodology, Software, Investigation, Data Curation, Writing – Original draft, Visualization. **Leon T. Hauser:** Conceptualization, Methodology, Investigation, Data Curation, Writing – Original draft, Supervision, Funding Acquisition. **Hamed Gholizadeh:** Data Curation, Writing – Review & Editing. **Anna-Katharina Schweiger:** Data Curation, Writing – Review & Editing. **Christian Rossi:** Conceptualization, Methodology, Investigation, Data Curation, Writing – Original draft, Supervision, Funding Acquisition.

Acknowledgements

This work was conducted under the 'Biodiv-Watch' project, funded by the ESA Initial Support for Innovation (EISI) [Grant Number 4000138090], and with the financial and operational support of the Swiss National Park (SNP). Hamed Gholizadeh was supported by a NASA NIP award [80NSSC21K0941]. This work is based on data obtained within the DFG Priority Program 1374 'Infrastructure-Biodiversity-Exploratories'. We thank the staff of the three exploratories, the BE office and the BExIS team for their work in maintaining the plot and project infrastructure, and Markus Fischer, the late Elisabeth Kalko, Eduard Linsenmair, Dominik Hessenmöller, Jens Nieschulze, Daniel Prati, Ingo Schöning, François Buscot, Ernst-Detlef Schulze and Wolfgang W. Weisser for their role in setting up the Biodiversity Exploratories project. Field work permits were issued by the responsible state environmental offices of Baden-Württemberg, Thüringen, and Brandenburg (according to § 72 BbgNatSchG). The authors thank Antonia Ludwig for her insightful comments on an earlier version of the manuscript and Matteo Delucchi of the consulting team of the Applied Statistics group at the Department of Mathematical Modeling and Machine Learning, University of Zurich.

Data availability

This work is based on data elaborated by the BExIS and Botany core projects of the Biodiversity Exploratories program (DFG Priority Program 1374). The datasets are publicly available in the Biodiversity Exploratories Information System (http://doi.org/10.17616/R32P9Q). The datasets are listed in the references section. Field data for Switzerland and Oklahoma are available upon request. Python codes and synthetic mock data are available upon request.

References

Aguirre-Gutiérrez, J., Rifai, S., Shenkin, A., Oliveras, I., Bentley, L.P., Svátek, M., Girardin, C.A.J., Both, S., Riutta, T., Berenguer, E., Kissling, W.D., Bauman, D., Raab, N., Moore, S., Farfan-Rios, W., Figueiredo, A.E.S., Reis, S.M., Ndong, J.E., Ondo, F.E., N'ssi Bengone, N., Mihindou, V., Moraes de Seixas, M.M., Adu-Bredu, S., Abernethy, K., Asner, G.P., Barlow, J., Burslem, D.F.R.P., Coomes, D.A., Cernusak, L.A., Dargie, G.C., Enquist, B.J., Ewers, R.M., Ferreira, J., Jeffery, K.J., Joly, C.A., Lewis, S.L., Marimon-Junior, B.H., Martin, R.E., Morandi, P.S., Phillips, O.L., Quesada, C.A., Salinas, N., Schwantes Marimon, B., Silman, M., Teh, Y.A., White, L.J.T., Malhi, Y., 2021. Pantropical modelling of canopy functional traits using Sentinel-2 remote sensing data. Remote Sens Environ 252, 112122. https://doi.org/10.1016/j.rse.2020.112122

Ali, I., Cawkwell, F., Dwyer, E., Barrett, B., Green, S., 2016. Satellite remote sensing of grasslands: from observation to management. Journal of Plant Ecology 9, 649–671. https://doi.org/10.1093/jpe/rtw005

Ali, I., Cawkwell, F., Dwyer, E., Green, S., 2017. Modeling Managed Grassland Biomass Estimation by Using Multitemporal Remote Sensing Data—A Machine Learning Approach. IEEE J Sel Top Appl Earth Obs Remote Sens 10, 3254–3264. https://doi.org/10.1109/JSTARS.2016.2561618

Amin, E., Verrelst, J., Rivera-Caicedo, J.P., Pipia, L., Ruiz-Verdú, A., Moreno, J., 2021. Prototyping Sentinel-2 green LAI and brown LAI products for cropland monitoring. Remote Sens Environ 255, 112168. https://doi.org/10.1016/j.rse.2020.112168

Anderson, R.H., Fuhlendorf, S.D., Engle, D.M., 2006. Soil Nitrogen Availability in Tallgrass Prairie Under the Fire–Grazing Interaction. Rangel Ecol Manag 59, 625–631. https://doi.org/10.2111/05-088R2.1

Bailey, D.W., Gross, J.E., Laca, E.A., Rittenhouse, L.R., Coughenour, M.B., Swift, D.M., Sims, P.L., 1996. Mechanisms That Result in Large Herbivore Grazing Distribution Patterns. Journal of Range Management 49, 386. https://doi.org/10.2307/4002919

Bai, Y., Cotrufo, M.F., 2022. Grassland soil carbon sequestration: Current understanding, challenges, and solutions. Science (1979) 377, 603–608. https://doi.org/10.1126/science.abo2380

Bardgett, R.D., Bullock, J.M., Lavorel, S., Manning, P., Schaffner, U., Ostle, N., Chomel, M., Durigan, G., L. Fry, E., Johnson, D., Lavallee, J.M., Le Provost, G., Luo, S., Png, K., Sankaran, M., Hou, X., Zhou, H., Ma, L., Ren, W., Li, X., Ding, Y., Li, Y., Shi, H., 2021. Combatting global grassland degradation. Nat Rev Earth Environ 2, 720–735. https://doi.org/10.1038/s43017-021-00207-2

Beck, H.E., Zimmermann, N.E., McVicar, T.R., Vergopolan, N., Berg, A., Wood, E.F., 2018. Present and future Köppen-Geiger climate classification maps at 1-km resolution. Sci Data 5, 180214. https://doi.org/10.1038/sdata.2018.214

Bengtsson, J., Bullock, J.M., Egoh, B., Everson, C., Everson, T., O'Connor, T., O'Farrell, P.J., Smith, H.G., Lindborg, R., 2019. Grasslands—more important for ecosystem services than you might think. Ecosphere 10, e02582. https://doi.org/10.1002/ecs2.2582

Berger, K., Atzberger, C., Danner, M., D'Urso, G., Mauser, W., Vuolo, F., Hank, T., 2018. Evaluation of the PROSAIL Model Capabilities for Future Hyperspectral Model Environments: A Review Study. Remote Sens (Basel) 10, 85. https://doi.org/10.3390/rs10010085

Berger, K., Hank, T., Halabuk, A., Rivera-Caicedo, J.P., Wocher, M., Mojses, M., Gerhátová, K., Tagliabue, G., Dolz, M.M., Venteo, A.B.P., Verrelst, J., 2021a. Assessing Non-Photosynthetic Cropland Biomass from Spaceborne Hyperspectral Imagery. Remote Sens (Basel) 13, 4711. https://doi.org/10.3390/rs13224711

Berger, K., Rivera Caicedo, J.P., Martino, L., Wocher, M., Hank, T., Verrelst, J., 2021b. A Survey of Active Learning for Quantifying Vegetation Traits from Terrestrial Earth Observation Data. Remote Sens (Basel) 13, 287. https://doi.org/10.3390/rs13020287

Berger, K., Verrelst, J., Féret, J.-B., Hank, T., Wocher, M., Mauser, W., Camps-Valls, G., 2020. Retrieval of aboveground crop nitrogen content with a hybrid machine learning method. International Journal of Applied Earth Observation and Geoinformation 92, 102174. https://doi.org/10.1016/j.jag.2020.102174

Binh, N.A., Hauser, L.T., Viet Hoa, P., Thi Phuong Thao, G., An, N.N., Nhut, H.S., Phuong, T.A., Verrelst, J., 2022. Quantifying mangrove leaf area index from Sentinel-2 imagery using hybrid models and active learning. Int J Remote Sens 43, 5636–5657. https://doi.org/10.1080/01431161.2021.2024912

Blüthgen, N., Dormann, C.F., Prati, D., Klaus, V.H., Kleinebecker, T., Hölzel, N., Alt, F., Boch, S., Gockel, S., Hemp, A., Müller, J., Nieschulze, J., Renner, S.C., Schöning, I., Schumacher, U., Socher, S.A., Wells, K., Birkhofer, K., Buscot, F., Oelmann, Y., Rothenwöhrer, C., Scherber, C., Tscharntke, T., Weiner, C.N., Fischer, M., Kalko, E.K.V., Linsenmair, K.E., Schulze, E.-D., Weisser, W.W., 2012. A quantitative index of land-use intensity in grasslands: Integrating mowing, grazing and fertilization. Basic Appl Ecol 13, 207–220. https://doi.org/10.1016/j.baae.2012.04.001

Bolliger, R., Prati, D., Fischer, M., 2020. Vegetation Records for Grassland EPs, 2008 - 2020. Version 2. Biodiversity Exploratories Information System. Dataset. https://www.bexis.uni-jena.de/ddm/data/Showdata/27386. Dataset ID = 27386.

Breiman, L., 2001. Random forests. Mach Learn 45, 5–32. https://doi.org/https://doi.org/10.1023/A:1010933404324

Brown, L.A., Ogutu, B.O., Dash, J., 2019. Estimating Forest Leaf Area Index and Canopy Chlorophyll Content with Sentinel-2: An Evaluation of Two Hybrid Retrieval Algorithms. Remote Sens (Basel) 11, 1752. https://doi.org/10.3390/rs11151752

Busch, V., Klaus, V.H., Penone, C., Schäfer, D., Boch, S., Prati, D., Müller, J., Socher, S.A., Niinemets, Ü., Peñuelas, J., Hölzel, N., Fischer, M., Kleinebecker, T., 2018. Nutrient stoichiometry and land use rather than species richness determine plant functional diversity. Ecol Evol 8, 601–616. https://doi.org/10.1002/ece3.3609

Caballero, G., Pezzola, A., Winschel, C., Sanchez Angonova, P., Casella, A., Orden, L., Salinero-Delgado, M., Reyes-Muñoz, P., Berger, K., Delegido, J., Verrelst, J., 2023. Synergy of Sentinel-1 and Sentinel-2 Time Series for Cloud-Free Vegetation Water Content Mapping with Multi-Output Gaussian Processes. Remote Sens (Basel) 15, 1822. https://doi.org/10.3390/rs15071822

Campos-Taberner, M., Moreno-Martínez, Á., García-Haro, F., Camps-Valls, G., Robinson, N., Kattge, J., Running, S., 2018. Global Estimation of Biophysical Variables from Google Earth Engine Platform. Remote Sens (Basel) 10, 1167. https://doi.org/10.3390/rs10081167

Cavender-Bares, J., Schneider, F.D., Santos, M.J., Armstrong, A., Carnaval, A., Dahlin, K.M., Fatoyinbo, L., Hurtt, G.C., Schimel, D., Townsend, P.A., Ustin, S.L., Wang, Z., Wilson, A.M., 2022. Integrating

remote sensing with ecology and evolution to advance biodiversity conservation. Nat Ecol Evol 6, 506–519. https://doi.org/10.1038/s41559-022-01702-5

Chen, T., Guestrin, C., 2016. XGBoost: A scalable tree boosting system. Proceedings of the ACM SIGKDD International Conference on Knowledge Discovery and Data Mining 13-17-August-2016, 785–794. https://doi.org/10.1145/2939672.2939785

Combal, B., Baret, F., Weiss, M., Trubuil, A., Macé, D., Pragnère, A., Myneni, R., Knyazikhin, Y., Wang, L., 2003. Retrieval of canopy biophysical variables from bidirectional reflectance. Remote Sens Environ 84, 1–15. https://doi.org/10.1016/S0034-4257(02)00035-4

Darvishzadeh, R., Atzberger, C., Skidmore, A., Schlerf, M., 2011. Mapping grassland leaf area index with airborne hyperspectral imagery: A comparison study of statistical approaches and inversion of radiative transfer models. ISPRS Journal of Photogrammetry and Remote Sensing 66, 894–906. https://doi.org/10.1016/J.ISPRSJPRS.2011.09.013

Dehghan-Shoar, M.H., Orsi, A.A., Pullanagari, R.R., Yule, I.J., 2023. A hybrid model to predict nitrogen concentration in heterogeneous grassland using field spectroscopy. Remote Sens Environ 285, 113385. https://doi.org/10.1016/j.rse.2022.113385

Delegido, J., Verrelst, J., Rivera, J.P., Ruiz-Verdú, A., Moreno, J., 2015. Brown and green LAI mapping through spectral indices. International Journal of Applied Earth Observation and Geoinformation 35, 350–358. https://doi.org/10.1016/j.jag.2014.10.001

de Sá, N.C., Baratchi, M., Hauser, L.T., van Bodegom, P., 2021. Exploring the Impact of Noise on Hybrid Inversion of PROSAIL RTM on Sentinel-2 Data. Remote Sens (Basel) 13, 648. https://doi.org/10.3390/rs13040648

De Vroey, M., de Vendictis, L., Zavagli, M., Bontemps, S., Heymans, D., Radoux, J., Koetz, B., Defourny, P., 2022. Mowing detection using Sentinel-1 and Sentinel-2 time series for large scale grassland monitoring. Remote Sens Environ 280, 113145. https://doi.org/10.1016/j.rse.2022.113145

Dixon, A.P., Faber-Langendoen, D., Josse, C., Morrison, J., Loucks, C.J., 2014. Distribution mapping of world grassland types. J Biogeogr 41, 2003–2019. https://doi.org/10.1111/jbi.12381

Erb, K.-H., Kastner, T., Plutzar, C., Bais, A.L.S., Carvalhais, N., Fetzel, T., Gingrich, S., Haberl, H., Lauk, C., Niedertscheider, M., Pongratz, J., Thurner, M., Luyssaert, S., 2018. Unexpectedly large impact of forest management and grazing on global vegetation biomass. Nature 553, 73–76. https://doi.org/10.1038/nature25138

Fang, H., Liang, S., Kuusk, A., 2003. Retrieving leaf area index using a genetic algorithm with a canopy radiative transfer model. Remote Sens Environ 85, 257–270. https://doi.org/10.1016/S0034-4257(03)00005-1

Féret, J.-B., Berger, K., de Boissieu, F., Malenovský, Z., 2021. PROSPECT-PRO for estimating content of nitrogen-containing leaf proteins and other carbon-based constituents. Remote Sens Environ 252, 112173. https://doi.org/10.1016/j.rse.2020.112173

Féret, J.-B., François, C., Asner, G.P., Gitelson, A.A., Martin, R.E., Bidel, L.P.R., Ustin, S.L., le Maire, G., Jacquemoud, S., 2008. PROSPECT-4 and 5: Advances in the leaf optical properties model separating photosynthetic pigments. Remote Sens Environ 112, 3030–3043. https://doi.org/10.1016/j.rse.2008.02.012

Féret, J.-B., Gitelson, A.A., Noble, S.D., Jacquemoud, S., 2017. PROSPECT-D: Towards modeling leaf optical properties through a complete lifecycle. Remote Sens Environ 193, 204–215. https://doi.org/10.1016/j.rse.2017.03.004

Féret, J.-B., le Maire, G., Jay, S., Berveiller, D., Bendoula, R., Hmimina, G., Cheraiet, A., Oliveira, J.C., Ponzoni, F.J., Solanki, T., de Boissieu, F., Chave, J., Nouvellon, Y., Porcar-Castell, A., Proisy, C., Soudani, K., Gastellu-Etchegorry, J.-P., Lefèvre-Fonollosa, M.-J., 2019. Estimating leaf mass per area and equivalent water thickness based on leaf optical properties: Potential and limitations of physical modeling and machine learning. Remote Sens Environ 231, 110959. https://doi.org/10.1016/j.rse.2018.11.002

Féret, J., de Boissieu, F., 2022. prosail: PROSAIL leaf and canopy radiative transfer model and inversion routines. R package version 1.1.1 [WWW Document]. URL https://gitlab.com/jbferet/prosail

Fischer, M., Bossdorf, O., Gockel, S., Hänsel, F., Hemp, A., Hessenmöller, D., Korte, G., Nieschulze, J., Pfeiffer, S., Prati, D., Renner, S., Schöning, I., Schumacher, U., Wells, K., Buscot, F., Kalko, E.K.V., Linsenmair, K.E., Schulze, E.-D., Weisser, W.W., 2010. Implementing large-scale and long-term functional biodiversity research: The Biodiversity Exploratories. Basic Appl Ecol 11, 473–485. https://doi.org/10.1016/j.baae.2010.07.009

Friedman, J.H., 2001. Greedy function approximation: A gradient boosting machine. Ann Stat 29, 1189–1232. https://doi.org/10.1214/AOS/1013203451

Fuhlendorf, S.D., Engle, D.M., 2004. Application of the fire-grazing interaction to restore a shifting mosaic on tallgrass prairie. Journal of Applied Ecology 41, 604–614. https://doi.org/10.1111/j.0021-8901.2004.00937.x

Fuhlendorf, S.D., Engle, D.M., 2001. Restoring Heterogeneity on Rangelands: Ecosystem Management Based on Evolutionary Grazing Patterns. Bioscience 51, 625–632. https://doi.org/https://doi.org/10.1641/0006-3568(2001)051[0625:RHOREM]2.0.CO;2

Gascon, F., Bouzinac, C., Thépaut, O., Jung, M., Francesconi, B., Louis, J., Lonjou, V., Lafrance, B., Massera, S., Gaudel-Vacaresse, A., Languille, F., Alhammoud, B., Viallefont, F., Pflug, B., Bieniarz, J., Clerc, S., Pessiot, L., Trémas, T., Cadau, E., De Bonis, R., Isola, C., Martimort, P., Fernandez, V., 2017. Copernicus Sentinel-2A Calibration and Products Validation Status. Remote Sens (Basel) 9, 584. https://doi.org/10.3390/rs9060584

Gholizadeh, H., Friedman, M.S., McMillan, N.A., Hammond, W.M., Hassani, K., Sams, A. V., Charles, M.D., Garrett, D.R., Joshi, O., Hamilton, R.G., Fuhlendorf, S.D., Trowbridge, A.M., Adams, H.D., 2022. Mapping invasive alien species in grassland ecosystems using airborne imaging spectroscopy and remotely observable vegetation functional traits. Remote Sens Environ 271, 112887. https://doi.org/10.1016/j.rse.2022.112887

Gholizadeh, H., Rakotoarivony, M.N.A., Hassani, K., Johnson, K.G., Hamilton, R.G., Fuhlendorf, S.D., Schneider, F.D., Bachelot, B., 2024. Advancing our understanding of plant diversity-biological invasion relationships using imaging spectroscopy. Remote Sens Environ 304, 114028. https://doi.org/10.1016/j.rse.2024.114028

Gorelick, N., Hancher, M., Dixon, M., Ilyushchenko, S., Thau, D., Moore, R., 2017. Google Earth Engine: Planetary-scale geospatial analysis for everyone. Remote Sens Environ 202, 18–27. https://doi.org/10.1016/j.rse.2017.06.031

962 Guerini Filho, M., Kuplich, T.M., Quadros, F.L.F. De, 2020. Estimating natural grassland biomass by
963 vegetation indices using Sentinel 2 remote sensing data. Int J Remote Sens 41, 2861–2876.
964 https://doi.org/10.1080/01431161.2019.1697004

965 Habel, J.C., Dengler, J., Janišová, M., Török, P., Wellstein, C., Wiezik, M., 2013. European grassland
966 ecosystems: threatened hotspots of biodiversity. Biodivers Conserv 22, 2131–2138.
967 https://doi.org/10.1007/s10531-013-0537-x

968 Hamilton, R.G., 2007. Restoring heterogeneity on the Tallgrass Prairie Preserve: applying the fire-
969 grazing interaction model, in: Masters, R.E., Galley, K.E.M. (Eds.), Proceedings of the 23rd Tall
970 Timbers Fire Ecology Conference: Fire in Grassland and Shrubland Ecosystems. Tall Timbers
971 Research Station, Tallahassee, FL, pp. 163–169.

972 Hauser, L.T., Féret, J.-B., An Binh, N., van der Windt, N., Sil, Â.F., Timmermans, J., Soudzilovskaia,
973 N.A., van Bodegom, P.M., 2021a. Towards scalable estimation of plant functional diversity from
974 Sentinel-2: In-situ validation in a heterogeneous (semi-)natural landscape. Remote Sens Environ
975 262, 112505. https://doi.org/10.1016/j.rse.2021.112505

976 Hauser, L.T., Timmermans, J., van der Windt, N., Sil, Â.F., César de Sá, N., Soudzilovskaia, N.A., van
977 Bodegom, P.M., 2021b. Explaining discrepancies between spectral and in-situ plant diversity in
978 multispectral satellite earth observation. Remote Sens Environ 265, 112684.
979 https://doi.org/10.1016/j.rse.2021.112684

980 Helfenstein, I.S., Schneider, F.D., Schaepman, M.E., Morsdorf, F., 2022. Assessing biodiversity from
981 space: Impact of spatial and spectral resolution on trait-based functional diversity. Remote Sens
982 Environ 275, 113024. https://doi.org/10.1016/j.rse.2022.113024

983 He, L., Li, A., Yin, G., Nan, X., Bian, J., 2019. Retrieval of Grassland Aboveground Biomass through
984 Inversion of the PROSAIL Model with MODIS Imagery. Remote Sensing 2019, Vol. 11, Page 1597
985 11, 1597. https://doi.org/10.3390/RS11131597

986 Hinderling, J., Penone, C., Fischer, M., Prati, D., Hoelzel, N., 2023. Biomass data for grassland EPs,
987 2009 - 2022. Version 8. Biodiversity Exploratories Information System. Dataset.
988 https://www.bexis.uni-jena.de/ddm/data/Showdata/31448. Dataset ID = 31448.

989 Hobohm, C., Bruchmann, I., 2009. Endemische Gefäßpflanzen und ihre Habitate in Europa - Plädoyer
990 für den Schutz der Grasland-Ökosysteme. Berichte der Reinhold-Tüxen-Gesellschaft 21, 142–
991 161.

992 Huete, A., Didan, K., Miura, T., Rodriguez, E.P., Gao, X., Ferreira, L.G., 2002. Overview of the
993 radiometric and biophysical performance of the MODIS vegetation indices. Remote Sens
994 Environ 83, 195–213. https://doi.org/10.1016/S0034-4257(02)00096-2

995 Jacquemoud, S., Baret, F., 1990. PROSPECT: A model of leaf optical properties spectra. Remote Sens
996 Environ 34, 75–91. https://doi.org/10.1016/0034-4257(90)90100-Z

997 Jacquemoud, S., Verhoef, W., Baret, F., Bacour, C., Zarco-Tejada, P.J., Asner, G.P., François, C., Ustin,
998 S.L., 2009. PROSPECT + SAIL models: A review of use for vegetation characterization. Remote
999 Sens Environ 113, S56–S66. https://doi.org/10.1016/J.RSE.2008.01.026

1000 Jehle, M., Hueni, A., Damm, A., D'Odorico, P., Weyermann, J., Kneubiihler, M., Schlapfer, D.,
1001 Schaepman, M.E., Meuleman, K., 2010. APEX - current status, performance and validation
1002 concept, in: 2010 IEEE Sensors. IEEE, pp. 533–537.
1003 https://doi.org/10.1109/ICSENS.2010.5690122

Joswig, J.S., Wirth, C., Schuman, M.C., Kattge, J., Reu, B., Wright, I.J., Sippel, S.D., Rüger, N., Richter, R., Schaepman, M.E., van Bodegom, P.M., Cornelissen, J.H.C., Díaz, S., Hattingh, W.N., Kramer, K., Lens, F., Niinemets, Ü., Reich, P.B., Reichstein, M., Römermann, C., Schrodt, F., Anand, M., Bahn, M., Byun, C., Campetella, G., Cerabolini, B.E.L., Craine, J.M., Gonzalez-Melo, A., Gutiérrez, A.G., He, T., Higuchi, P., Jactel, H., Kraft, N.J.B., Minden, V., Onipchenko, V., Peñuelas, J., Pillar, V.D., Sosinski, Ê., Soudzilovskaia, N.A., Weiher, E., Mahecha, M.D., 2021. Climatic and soil factors explain the two-dimensional spectrum of global plant trait variation. Nat Ecol Evol 6, 36–50. https://doi.org/10.1038/s41559-021-01616-8

Kothari, S., Schweiger, A.K., 2022. Plant spectra as integrative measures of plant phenotypes. Journal of Ecology 110, 2536–2554. https://doi.org/10.1111/1365-2745.13972

Kovács, D.D., Reyes-Muñoz, P., Salinero-Delgado, M., Mészáros, V.I., Berger, K., Verrelst, J., 2023. Cloud-Free Global Maps of Essential Vegetation Traits Processed from the TOA Sentinel-3 Catalogue in Google Earth Engine. Remote Sens (Basel) 15, 3404. https://doi.org/10.3390/rs15133404

Lawrence, D.M., Fisher, R.A., Koven, C.D., Oleson, K.W., Swenson, S.C., Bonan, G., Collier, N., Ghimire, B., van Kampenhout, L., Kennedy, D., Kluzek, E., Lawrence, P.J., Li, F., Li, H., Lombardozzi, D., Riley, W.J., Sacks, W.J., Shi, M., Vertenstein, M., Wieder, W.R., Xu, C., Ali, A.A., Badger, A.M., Bisht, G., van den Broeke, M., Brunke, M.A., Burns, S.P., Buzan, J., Clark, M., Craig, A., Dahlin, K., Drewniak, B., Fisher, J.B., Flanner, M., Fox, A.M., Gentine, P., Hoffman, F., Keppel-Aleks, G., Knox, R., Kumar, S., Lenaerts, J., Leung, L.R., Lipscomb, W.H., Lu, Y., Pandey, A., Pelletier, J.D., Perket, J., Randerson, J.T., Ricciuto, D.M., Sanderson, B.M., Slater, A., Subin, Z.M., Tang, J., Thomas, R.Q., Val Martin, M., Zeng, X., 2019. The Community Land Model Version 5: Description of New Features, Benchmarking, and Impact of Forcing Uncertainty. J Adv Model Earth Syst 11, 4245–4287. https://doi.org/10.1029/2018MS001583

Lemaire, G., Hodgson, J., Chabbi, A. (Eds.), 2011. Grassland productivity and ecosystem services. CAB International, Wallingford.

Li, C., Zhou, L., Xu, W., 2021. Estimating Aboveground Biomass Using Sentinel-2 MSI Data and Ensemble Algorithms for Grassland in the Shengjin Lake Wetland, China. Remote Sensing 2021, Vol. 13, Page 1595 13, 1595. https://doi.org/10.3390/RS13081595

Li, F., Zeng, Y., Luo, J., Ma, R., Wu, B., 2016. Modeling grassland aboveground biomass using a pure vegetation index. Ecol Indic 62, 279–288. https://doi.org/10.1016/j.ecolind.2015.11.005

Limb, R.F., Hickman, K.R., Engle, D.M., Norland, J.E., Fuhlendorf, S.D., 2007. Digital Photography: Reduced Investigator Variation in Visual Obstruction Measurements for Southern Tallgrass Prairie. Rangel Ecol Manag 60, 548–552. https://doi.org/https://doi.org/10.2111/1551-5028(2007)60[548:DPRIVI]2.0.CO;2

Liu, A., Cheng, X., Chen, Z., 2021. Performance evaluation of GEDI and ICESat-2 laser altimeter data for terrain and canopy height retrievals. Remote Sens Environ 264, 112571. https://doi.org/10.1016/j.rse.2021.112571

Liu, H., Cai, J., Ong, Y.-S., 2018. Remarks on multi-output Gaussian process regression. Knowl Based Syst 144, 102–121. https://doi.org/10.1016/j.knosys.2017.12.034

Locherer, M., Hank, T., Danner, M., Mauser, W., 2015. Retrieval of Seasonal Leaf Area Index from Simulated EnMAP Data through Optimized LUT-Based Inversion of the PROSAIL Model. Remote Sens (Basel) 7, 10321–10346. https://doi.org/10.3390/rs70810321

Martínez-Ferrer, L., Moreno-Martínez, Á., Campos-Taberner, M., García-Haro, F.J., Muñoz-Marí, J., Running, S.W., Kimball, J., Clinton, N., Camps-Valls, G., 2022. Quantifying uncertainty in high resolution biophysical variable retrieval with machine learning. Remote Sens Environ 280, 113199. https://doi.org/10.1016/J.RSE.2022.113199

Masek, J.G., Wulder, M.A., Markham, B., McCorkel, J., Crawford, C.J., Storey, J., Jenstrom, D.T., 2020. Landsat 9: Empowering open science and applications through continuity. Remote Sens Environ 248, 111968. https://doi.org/10.1016/j.rse.2020.111968

Mesonet, 2024. Monthly Rainfall Table: Norman (NRMN) Monthly Actual Oklahoma Mesonet Rainfall Table (in inches) [WWW Document]. URL https://www.mesonet.org/weather/rainfall/monthly-rainfall-table?ref=1210 (accessed 1.4.24).

Meyer, H., Pebesma, E., 2020. Predicting into unknown space? Estimating the area of applicability of spatial prediction models. Methods Ecol Evol 12, 1620–1633. https://doi.org/10.1111/2041-210X.13650

Moreno-Martinez, A., Camps-Valls, G., Kattge, J., Robinson, N., Reichstein, M., van Bodegom, P., Kramer, K., Cornelissen, J.H.C., Reich, P., Bahn, M., Niinemets, Ülo, Peñuelas, J., Craine, J., Cerabolini, B.E.L., Minden, V., Laughlin, D.C., Sack, L., Allred, B., Baraloto, C., Byun, C., Soudzilovskaia, N.A., Running, S.W., 2020. A Methodology to Derive Global Maps of Leaf Traits Using Remote Sensing and Climate Data. Remote Sens Environ 218, 69–88. https://doi.org/10.1016/j.rse.2018.09.006

Müller-Wilm, U., Louis, J., Richter, R., Gascon, F., Niezette, M., 2013. Sentinel-2 level 2A prototype processor: architecture, algorithms and first results, in: Proceedings of the ESA Living Planet Symposium. Edinburgh, UK, pp. 9–13.

Muñoz Sabater, J., 2019. ERA5-Land hourly data from 1950 to present. Copernicus Climate Change Service (C3S) Climate Data Store. https://doi.org/10.24381/cds.e2161bac

Muro, J., Linstädter, A., Magdon, P., Wöllauer, S., Männer, F.A., Schwarz, L.-M., Ghazaryan, G., Schultz, J., Malenovský, Z., Dubovyk, O., 2022. Predicting plant biomass and species richness in temperate grasslands across regions, time, and land management with remote sensing and deep learning. Remote Sens Environ 282, 113262. https://doi.org/10.1016/j.rse.2022.113262

O'Mara, F.P., 2012. The role of grasslands in food security and climate change. Ann Bot 110, 1263–1270. https://doi.org/10.1093/aob/mcs209

Ostrowski, A., Nieschulze, J., Schulze, E.D., König-Ries, B., 2020. Coordinates and Inventory Overview of all Grid Plots (GPs). Version 6. Biodiversity Exploratories Information System. Dataset. https://www.bexis.uni-jena.de. Dataset ID = 20907.

Pedregosa, F., Varoquaux, G., Gramfort, A., Michel, V., Thirion, B., Grisel, O., Blondel, M., Müller, A., Nothman, J., Louppe, G., Prettenhofer, P., Weiss, R., Dubourg, V., Vanderplas, J., Passos, A., Cournapeau, D., Brucher, M., Perrot, M., Duchesnay, É., 2012. Scikit-learn: Machine Learning in Python. Journal of Machine Learning Research 12, 2825–2830.

Pipia, L., Muñoz-Marí, J., Amin, E., Belda, S., Camps-Valls, G., Verrelst, J., 2019. Fusing optical and SAR time series for LAI gap filling with multioutput Gaussian processes. Remote Sens Environ 235, 111452. https://doi.org/10.1016/j.rse.2019.111452

Poortinga, A., Tenneson, K., Shapiro, A., Nquyen, Q., San Aung, K., Chishtie, F., Saah, D., 2019. Mapping Plantations in Myanmar by Fusing Landsat-8, Sentinel-2 and Sentinel-1 Data along

with Systematic Error Quantification. Remote Sens (Basel) 11, 831. https://doi.org/10.3390/rs11070831

Punalekar, S.M., Verhoef, A., Quaife, T.L., Humphries, D., Bermingham, L., Reynolds, C.K., 2018. Application of Sentinel-2A data for pasture biomass monitoring using a physically based radiative transfer model. Remote Sens Environ 218, 207–220. https://doi.org/10.1016/j.rse.2018.09.028

Quan, X., He, B., Yebra, M., Yin, C., Liao, Z., Zhang, X., Li, X., 2017. A radiative transfer model-based method for the estimation of grassland aboveground biomass. International Journal of Applied Earth Observation and Geoinformation 54, 159–168. https://doi.org/10.1016/J.JAG.2016.10.002

Raab, C., Riesch, F., Tonn, B., Barrett, B., Meißner, M., Balkenhol, N., Isselstein, J., 2020. Target-oriented habitat and wildlife management: estimating forage quantity and quality of semi-natural grasslands with Sentinel-1 and Sentinel-2 data. Remote Sens Ecol Conserv 6, 381–398. https://doi.org/10.1002/rse2.149

Ranghetti, M., Boschetti, M., Ranghetti, L., Tagliabue, G., Panigada, C., Gianinetto, M., Verrelst, J., Candiani, G., 2022. Assessment of maize nitrogen uptake from PRISMA hyperspectral data through hybrid modelling. Eur J Remote Sens. https://doi.org/10.1080/22797254.2022.2117650

Rasmussen, C.E., Williams, C.K.I., 2006. Gaussian Processes for Machine Learning. MIT Press, Cambridge, MA.

R Core Team, 2021. R: A Language and Environment for Statistical Computing. Vienna.

Reinermann, S., Asam, S., Kuenzer, C., 2020. Remote Sensing of Grassland Production and Management—A Review. Remote Sens (Basel) 12, 1949. https://doi.org/10.3390/rs12121949

Rempfler, T., Rossi, C., Schweizer, J., Peters, W., Signer, C., Filli, F., Jenny, H., Hackländer, K., Buchmann, S., Anderwald, P., 2024. Remote sensing reveals the role of forage quality and quantity for summer habitat use in red deer. Mov Ecol 12, 80. https://doi.org/10.1186/s40462-024-00521-6

Reuter, H.I., Nelson, A., Jarvis, A., 2007. An evaluation of void-filling interpolation methods for SRTM data. International Journal of Geographical Information Science 21, 983–1008. https://doi.org/10.1080/13658810601169899

Richter, K., Atzberger, C., Hank, T.B., Mauser, W., 2012. Derivation of biophysical variables from Earth observation data: validation and statistical measures. J Appl Remote Sens 6, 063557–1. https://doi.org/10.1117/1.JRS.6.063557

Richter, R., Schläpfer, D., 2002. Geo-atmospheric processing of airborne imaging spectrometry data. Part 2: Atmospheric/topographic correction. Int J Remote Sens 23, 2631–2649. https://doi.org/10.1080/01431160110115834

Rivera, J., Verrelst, J., Gómez-Dans, J., Muñoz-Marí, J., Moreno, J., Camps-Valls, G., 2015. An Emulator Toolbox to Approximate Radiative Transfer Models with Statistical Learning. Remote Sens (Basel) 7, 9347–9370. https://doi.org/10.3390/rs70709347

Rivera, J., Verrelst, J., Leonenko, G., Moreno, J., 2013. Multiple Cost Functions and Regularization Options for Improved Retrieval of Leaf Chlorophyll Content and LAI through Inversion of the PROSAIL Model. Remote Sens (Basel) 5, 3280–3304. https://doi.org/10.3390/rs5073280

Rossi, C., Kneubühler, M., Schütz, M., Schaepman, M.E., Haller, R.M., Risch, A.C., 2020. From local to regional: Functional diversity in differently managed alpine grasslands. Remote Sens Environ 236, 111415. https://doi.org/10.1016/j.rse.2019.111415

Rossi, C., McMillan, N.A., Schweizer, J.M., Gholizadeh, H., Groen, M., Ioannidis, N., Hauser, L.T., 2024. Parcel level temporal variance of remotely sensed spectral reflectance predicts plant diversity. Environmental Research Letters 19, 074023. https://doi.org/10.1088/1748-9326/ad545a

Roudier, P., 2021. Introduction to conditioned Latin hypercube sampling with the clhs package [WWW Document]. URL https://CRAN.R-project.org/package=clhs

Roy, D.P., Wulder, M.A., Loveland, T.R., C.E., W., Allen, R.G., Anderson, M.C., Helder, D., Irons, J.R., Johnson, D.M., Kennedy, R., Scambos, T.A., Schaaf, C.B., Schott, J.R., Sheng, Y., Vermote, E.F., Belward, A.S., Bindschadler, R., Cohen, W.B., Gao, F., Hipple, J.D., Hostert, P., Huntington, J., Justice, C.O., Kilic, A., Kovalskyy, V., Lee, Z.P., Lymburner, L., Masek, J.G., McCorkel, J., Shuai, Y., Trezza, R., Vogelmann, J., Wynne, R.H., Zhu, Z., 2014. Landsat-8: Science and product vision for terrestrial global change research. Remote Sens Environ 145, 154–172. https://doi.org/10.1016/j.rse.2014.02.001

Safanelli, J.L., Hengl, T., Parente, L.L., Minarik, R., Bloom, D.E., Todd-Brown, K., Gholizadeh, A., Mendes, W. de S., Sanderman, J., 2025. Open Soil Spectral Library (OSSL): Building reproducible soil calibration models through open development and community engagement. PLoS One 20, e0296545. https://doi.org/10.1371/journal.pone.0296545

Schaepman, M.E., Jehle, M., Hueni, A., D'Odorico, P., Damm, A., Weyermann, J., Schneider, F.D., Laurent, V., Popp, C., Seidel, F.C., Lenhard, K., Gege, P., Küchler, C., Brazile, J., Kohler, P., De Vos, L., Meuleman, K., Meynart, R., Schläpfer, D., Kneubühler, M., Itten, K.I., 2015. Advanced radiometry measurements and Earth science applications with the Airborne Prism Experiment (APEX). Remote Sens Environ 158, 207–219. https://doi.org/10.1016/j.rse.2014.11.014

Schiefer, F., Schmidtlein, S., Kattenborn, T., 2021. The retrieval of plant functional traits from canopy spectra through RTM-inversions and statistical models are both critically affected by plant phenology. Ecol Indic 121, 107062. https://doi.org/10.1016/j.ecolind.2020.107062

Schläpfer, D., Richter, R., 2002. Geo-atmospheric processing of airborne imaging spectrometry data. Part 1: Parametric orthorectification. Int J Remote Sens 23, 2609–2630. https://doi.org/10.1080/01431160110115825

Schweiger, A.K., 2020. Spectral Field Campaigns: Planning and Data Collection, in: Remote Sensing of Plant Biodiversity. Springer International Publishing, Cham, pp. 385–423. https://doi.org/10.1007/978-3-030-33157-3_15

Schweiger, A.K., Risch, A.C., Damm, A., Kneubühler, M., Haller, R., Schaepman, M.E., Schütz, M., 2015a. Using imaging spectroscopy to predict above-ground plant biomass in alpine grasslands grazed by large ungulates. Journal of Vegetation Science 26, 175–190. https://doi.org/10.1111/jvs.12214

Schweiger, A.K., Schütz, M., Anderwald, P., Schaepman, M.E., Kneubühler, M., Haller, R., Risch, A.C., 2015b. Foraging ecology of three sympatric ungulate species – Behavioural and resource maps indicate differences between chamois, ibex and red deer. Mov Ecol 3, 6. https://doi.org/10.1186/s40462-015-0033-x

Schweiger, A.K., Schütz, M., Risch, A.C., Kneubühler, M., Haller, R., Schaepman, M.E., 2017. How to predict plant functional types using imaging spectroscopy: linking vegetation community traits, plant functional types and spectral response. Methods Ecol Evol 8, 86–95. https://doi.org/10.1111/2041-210X.12642

Schwieder, M., Buddeberg, M., Kowalski, K., Pfoch, K., Bartsch, J., Bach, H., Pickert, J., Hostert, P., 2020. Estimating Grassland Parameters from Sentinel-2: A Model Comparison Study. PFG – Journal of Photogrammetry, Remote Sensing and Geoinformation Science 88, 379–390. https://doi.org/10.1007/s41064-020-00120-1

scikit-learn Developers, 2023. ConstantKernel [WWW Document]. URL https://scikit-learn.org/stable/modules/generated/sklearn.gaussian_process.kernels.ConstantKernel.html (accessed 10.12.23).

Sherrill, C.W., 2019. Analyzing sericea lespedeza (lespedeza cuneata) management practices and the importance of forbs in the diet of cattle and bison on tallgrass prairie (Master's Thesis). Oklahoma State University, Stillwater, OK.

Shoko, C., Mutanga, O., Dube, T., 2016. Progress in the remote sensing of C3 and C4 grass species aboveground biomass over time and space. ISPRS Journal of Photogrammetry and Remote Sensing 120, 13–24. https://doi.org/10.1016/J.ISPRSJPRS.2016.08.001

Socher, S.A., Prati, D., Boch, S., Müller, J., Klaus, V.H., Hölzel, N., Fischer, M., 2012. Direct and productivity-mediated indirect effects of fertilization, mowing and grazing on grassland species richness. Journal of Ecology 100, 1391–1399. https://doi.org/10.1111/j.1365-2745.2012.02020.x

Stevens, A., Ramirez-Lopez, L., 2022. An introduction to the prospectr package [WWW Document]. URL https://CRAN.R-project.org/package=prospectr

Tagliabue, G., Boschetti, M., Bramati, G., Candiani, G., Colombo, R., Nutini, F., Pompilio, L., Rivera-Caicedo, J.P., Rossi, M., Rossini, M., Verrelst, J., Panigada, C., 2022. Hybrid retrieval of crop traits from multi-temporal PRISMA hyperspectral imagery. ISPRS Journal of Photogrammetry and Remote Sensing 187, 362–377. https://doi.org/10.1016/j.isprsjprs.2022.03.014

The Nature Conservancy, 2023. Joseph H. Williams Tallgrass Prairie Preserve [WWW Document]. URL https://www.nature.org/en-us/get-involved/how-to-help/places-we-protect/tallgrass-prairie-preserve/ (accessed 3.29.23).

Van Vooren, L., Reubens, B., Broekx, S., Reheul, D., Verheyen, K., 2018. Assessing the impact of grassland management extensification in temperate areas on multiple ecosystem services and biodiversity. Agric Ecosyst Environ 267, 201–212. https://doi.org/10.1016/j.agee.2018.08.016

Vapnik, V., Golowich, S.E., Smola, A., 1997. Support vector method for function approximation, regression estimation, and signal processing. Adv Neural Inf Process Syst 281–287.

Verhoef, W., Jia, L., Xiao, Q., Su, Z., 2007. Unified Optical-Thermal Four-Stream Radiative Transfer Theory for Homogeneous Vegetation Canopies. IEEE Transactions on Geoscience and Remote Sensing 45, 1808–1822. https://doi.org/10.1109/TGRS.2007.895844

Verrelst, J., Alonso, L., Rivera Caicedo, J.P., Moreno, J., Camps-Valls, G., 2013a. Gaussian Process Retrieval of Chlorophyll Content From Imaging Spectroscopy Data. IEEE J Sel Top Appl Earth Obs Remote Sens 6, 867–874. https://doi.org/10.1109/JSTARS.2012.2222356

Verrelst, J., Camps-Valls, G., Muñoz-Marí, J., Rivera, J.P., Veroustraete, F., Clevers, J.G.P.W., Moreno, J., 2015. Optical remote sensing and the retrieval of terrestrial vegetation bio-geophysical properties – A review. ISPRS Journal of Photogrammetry and Remote Sensing 108, 273–290. https://doi.org/10.1016/j.isprsjprs.2015.05.005

Verrelst, J., Dethier, S., Rivera, J.P., Munoz-Mari, J., Camps-Valls, G., Moreno, J., 2016. Active Learning Methods for Efficient Hybrid Biophysical Variable Retrieval. IEEE Geoscience and Remote Sensing Letters 13, 1012–1016. https://doi.org/10.1109/LGRS.2016.2560799

Verrelst, J., Halabuk, A., Atzberger, C., Hank, T., Steinhauser, S., Berger, K., 2023. A comprehensive survey on quantifying non-photosynthetic vegetation cover and biomass from imaging spectroscopy. Ecol Indic 155, 110911. https://doi.org/10.1016/j.ecolind.2023.110911

Verrelst, J., Muñoz, J., Alonso, L., Delegido, J., Rivera, J.P., Camps-Valls, G., Moreno, J., 2012. Machine learning regression algorithms for biophysical parameter retrieval: Opportunities for Sentinel-2 and -3. Remote Sens Environ 118, 127–139. https://doi.org/10.1016/j.rse.2011.11.002

Verrelst, J., Rivera Caicedo, J., Muñoz-Marí, J., Camps-Valls, G., Moreno, J., 2017. SCOPE-Based Emulators for Fast Generation of Synthetic Canopy Reflectance and Sun-Induced Fluorescence Spectra. Remote Sens (Basel) 9, 927. https://doi.org/10.3390/rs9090927

Verrelst, J., Rivera-Caicedo, J.P., Reyes-Muñoz, P., Morata, M., Amin, E., Tagliabue, G., Panigada, C., Hank, T., Berger, K., 2021. Mapping landscape canopy nitrogen content from space using PRISMA data. ISPRS Journal of Photogrammetry and Remote Sensing 178, 382–395. https://doi.org/10.1016/j.isprsjprs.2021.06.017

Verrelst, J., Rivera, J.P., Leonenko, G., Alonso, L., Moreno, J., 2014. Optimizing LUT-Based RTM Inversion for Semiautomatic Mapping of Crop Biophysical Parameters from Sentinel-2 and -3 Data: Role of Cost Functions. IEEE Transactions on Geoscience and Remote Sensing 52, 257–269. https://doi.org/10.1109/TGRS.2013.2238242

Verrelst, J., Rivera, J.P., Moreno, J., Camps-Valls, G., 2013b. Gaussian processes uncertainty estimates in experimental Sentinel-2 LAI and leaf chlorophyll content retrieval. ISPRS Journal of Photogrammetry and Remote Sensing 86, 157–167. https://doi.org/10.1016/j.isprsjprs.2013.09.012

Viscarra Rossel, R.A., Behrens, T., Ben-Dor, E., Brown, D.J., Demattê, J.A.M., Shepherd, K.D., Shi, Z., Stenberg, B., Stevens, A., Adamchuk, V., Aïchi, H., Barthès, B.G., Bartholomeus, H.M., Bayer, A.D., Bernoux, M., Böttcher, K., Brodský, L., Du, C.W., Chappell, A., Fouad, Y., Genot, V., Gomez, C., Grunwald, S., Gubler, A., Guerrero, C., Hedley, C.B., Knadel, M., Morrás, H.J.M., Nocita, M., Ramirez-Lopez, L., Roudier, P., Campos, E.M.R., Sanborn, P., Sellitto, V.M., Sudduth, K.A., Rawlins, B.G., Walter, C., Winowiecki, L.A., Hong, S.Y., Ji, W., 2016. A global spectral library to characterize the world's soil. Earth Sci Rev 155, 198–230. https://doi.org/10.1016/j.earscirev.2016.01.012

Wang, G., Liu, S., Liu, T., Fu, Z., Yu, J., Xue, B., 2019. Modelling above-ground biomass based on vegetation indexes: a modified approach for biomass estimation in semi-arid grasslands. Int J Remote Sens 40, 3835–3854. https://doi.org/10.1080/01431161.2018.1553319

Wang, Z., Féret, J.-B., Liu, N., Sun, Z., Yang, L., Geng, S., Zhang, H., Chlus, A., Kruger, E.L., Townsend, P.A., 2023. Generality of leaf spectroscopic models for predicting key foliar functional traits across continents: A comparison between physically- and empirically-based approaches. Remote Sens Environ 293, 113614. https://doi.org/10.1016/j.rse.2023.113614

Wellstein, C., Chelli, S., Campetella, G., Bartha, S., Galiè, M., Spada, F., Canullo, R., 2013. Intraspecific phenotypic variability of plant functional traits in contrasting mountain grasslands habitats. Biodivers Conserv 22, 2353–2374. https://doi.org/10.1007/s10531-013-0484-6

White, R., Murray, S., Rohweder, M., 2000. Pilot Analysis of Global Ecosystems: Grassland Ecosystems. WRI Publications, Hapden Station, Baltimore, MD.

Wocher, M., Berger, K., Verrelst, J., Hank, T., 2022. Retrieval of carbon content and biomass from hyperspectral imagery over cultivated areas. ISPRS Journal of Photogrammetry and Remote Sensing 193, 104–114. https://doi.org/10.1016/j.isprsjprs.2022.09.003

Woodcock, C.E., 2002. Uncertainty in Remote Sensing, in: Foody, G.M., Atkinson, P.M. (Eds.), Uncertainty in Remote Sensing and GIS. Wiley, Chichester, pp. 19–24. https://doi.org/10.1002/0470035269.ch2

Xu, D., Guo, X., Li, Z., Yang, X., Yin, H., 2014. Measuring the dead component of mixed grassland with Landsat imagery. Remote Sens Environ 142, 33–43. https://doi.org/10.1016/j.rse.2013.11.017

Yuan, H., Ma, R., Atzberger, C., Li, F., Loiselle, S., Luo, J., 2015. Estimating Forest fAPAR from Multispectral Landsat-8 Data Using the Invertible Forest Reflectance Model INFORM. Remote Sens (Basel) 7, 7425–7446. https://doi.org/10.3390/rs70607425

Yuhas, R., Goetz, A., Boardman, J., 1992. Discrimination among semi-arid landscape endmembers using the spectral angle mapper (SAM) algorithm, in: Summaries of the Third Annual JPL Airborne Geoscience Workshop. Volume 1: AVIRIS Workshop. JPL, pp. 147–149.

Zeng, Y., Hao, D., Park, T., Zhu, P., Huete, A., Myneni, R., Knyazikhin, Y., Qi, J., Nemani, R.R., Li, F., Huang, J., Gao, Y., Li, B., Ji, F., Köhler, P., Frankenberg, C., Berry, J.A., Chen, M., 2023. Structural complexity biases vegetation greenness measures. Nat Ecol Evol 7, 1790–1798. https://doi.org/10.1038/s41559-023-02187-6

Zhang, F., Bennett, J.A., Zhang, B., Zhao, T., Bai, K., Zhao, M., Han, G., 2023. Responses of grassland productivity to mowing intensity and precipitation variability in a temperate steppe. Oecologia 201, 259–268. https://doi.org/10.1007/s00442-022-05305-6

Zhao, Y., Liu, Z., Wu, J., 2020. Grassland ecosystem services: a systematic review of research advances and future directions. Landsc Ecol 35, 793–814. https://doi.org/10.1007/s10980-020-00980-3

Zhou, K., Liu, Z., Qiao, Y., Xiang, T., Loy, C.C., 2022. Domain Generalization: A Survey. IEEE Trans Pattern Anal Mach Intell 1–20. https://doi.org/10.1109/TPAMI.2022.3195549

Zupanc, A., 2017. Improving Cloud Detection with Machine Learning [WWW Document]. URL https://medium.com/sentinel-hub/improving-cloud-detection-with-machine-learning-c09dc5d7cf13 (accessed 9.28.21).

Appendix A

Section A.1: Pre-processing of APEX data

Remote sensing data for the 365 plots inside the Swiss National Park (SNP) were acquired on 24 June 2010, 26 June 2011, 29 June 2012, and 12 July 2013 with the Airborne Prism Experiment (APEX) imaging spectrometer (Jehle et al., 2010; Schaepman et al., 2015). Of 334 spectral bands in the wavelength region from 380 to 2500 nm, 285 (2011), 301 (2011), 299 (2012), and 284 bands (2013) remained after noise removal. APEX data were resampled to 2 m pixel size using nearest neighbor interpolation and the parametric geocoding procedure PARGE (Schläpfer and Richter, 2002) and the airborne atmospheric and topographic correction model ATCOR-4 (Richter and Schläpfer, 2002) were used for geometric and atmospheric correction, respectively (Schweiger et al., 2015). We considered the 33 plots in 2010 and 9 plots in 2011 covered by two flight strips as individual samples, resulting in 407 samples. APEX spectral reflectance was resampled to the Sentinel-2 bands (ESA, 2015) using the prospectR R package *v0.2.6* (Stevens and Ramirez-Lopez, 2022) individually for each year because of changing APEX spectral response functions.

Section A.2: Outliers of ALB/HAI/SCH sites

The following condition (Equation A.1) was used to determine if a sample from the ALB/HAI/SCH sites was discarded due to an unusual biomass-Normalized Difference Vegetation Index (NDVI) relation while accounting for the saturation effect of NDVI (Huete et al., 1997; Van Der Meer et al., 2001):

$$NDVI < \frac{biomass\,[g\,m^{-2}]}{400}\ AND\ NDVI < 0.8 \quad \text{(A.1)}$$

The condition was met for 13 samples of 12 different plots (Figure A.1), for which we removed all samples from 2017-2020.

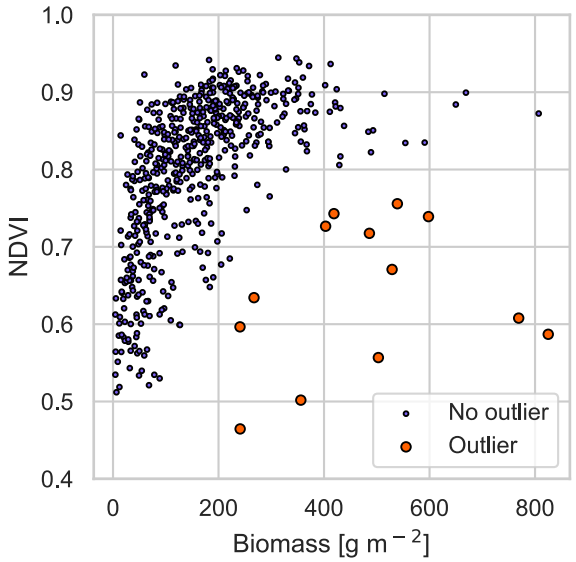

Figure A.1: Biomass content of the ALB, HAI, and SCH samples before sample selection plotted against the Normalized Difference Vegetation Index (NDVI). ALB: Schwäbische Alb, HAI: Hainich-Dün, SCH: Schorfheide-Chorin.

Section A.3: Local performance of hybrid models without the use of AL

Look-up tables (LUTs) generated with radiative transfer models (RTMs) such as PROSAIL are subject to inherent ill-posedness as the inversion does not necessarily lead to a unique solution (Combal et al., 2003). Additionally, such a LUT might include spectra simulated based on ecologically meaningless parameter combinations. Hence, prior knowledge can be used to subset the LUT based on correlations between plant traits (Schiefer et al., 2021). In this study, we used prior knowledge to define the value ranges and distributions of the selectable parameters, but we did not use prior information to further subset the LUT since covariances between traits might be site-specific and generating different LUTs for the study sites would have prevented any meaningful analysis of transferability. Instead, Active Learning (AL) was used to select the most informative spectra from the LUT (Verrelst et al., 2016). Correspondingly, not using AL leads to models being trained on the full LUT containing redundant and/or unrealistic information and drastically diminished model performance as illustrated in Figure A.2. Furthermore, without AL, model training is also independent of the optimization data, since no optimization of the training data takes place. Therefore, the inclusion of hybrid models without the use of AL for the systematic model comparison was waived.

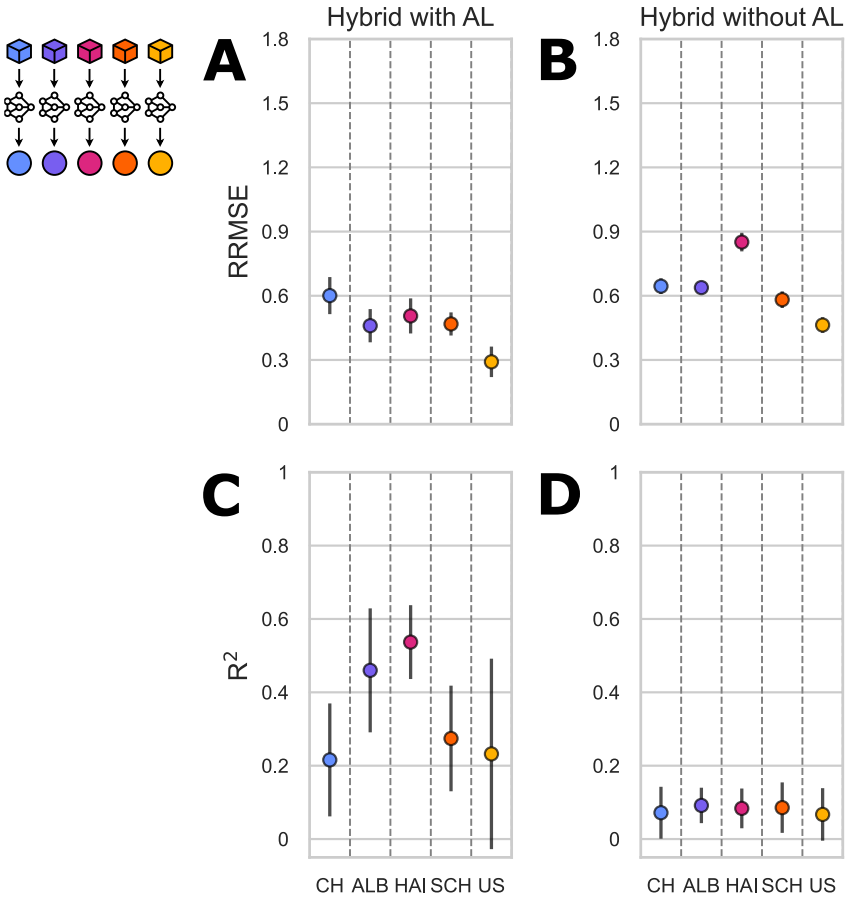

Figure A.2: Mean relative root-mean-square error (RRMSE, A, B) and coefficient of determination (R^2, C, D) ± 1 standard deviation for the local hybrid models with (A, C) and without (B, D) the use of Active Learning (AL) with an initial training set size of 2%. CH: Switzerland, ALB: Schwäbische Alb, HAI: Hainich-Dün, SCH: Schorfheide-Chorin, US: United States.

Section A.4: Cross-validation performance of local empirical models

Table A.1: Cross-validation performance of local empirical models. The parameters correspond to the best-performing combination of parameters tested during the fivefold cross-validation. CH: Switzerland, ALB: Schwäbische Alb, HAI: Hainich-Dün, SCH: Schorfheide-Chorin, US: United States, RFR: Random Forest regression, SVR: Support Vector regression, XGB: Extreme Gradient Boosting regression, GPR: Gaussian Process regression, R^2: coefficient of determination, RMSE: root-mean-square error, RRMSE: relative root-mean-square error. Nomenclature of parameter names for RFR, SVR, and GPR according to Pedregosa et al. (2012), for XGB according to Chen and Guestrin (2016).

Site	Model	Seed	Parameters	R^2	RMSE [g m^{-2}]	RRMSE
CH	RFR	1	'max_depth': None, 'max_features': 'sqrt', 'max_leaf_nodes': None, 'min_samples_leaf': 1, 'n_estimators': 100	0.262	97.383	0.567
CH	RFR	2	'max_depth': 5, 'max_features': 'sqrt', 'max_leaf_nodes': None, 'min_samples_leaf': 1, 'n_estimators': 100	0.22	97.707	0.559
CH	RFR	3	'max_depth': None, 'max_features': 10, 'max_leaf_nodes': 10, 'min_samples_leaf': 2, 'n_estimators': 100	0.184	104.372	0.595
CH	RFR	4	'max_depth': None, 'max_features': 10, 'max_leaf_nodes': None, 'min_samples_leaf': 2, 'n_estimators': 100	0.25	98.643	0.561
CH	RFR	5	'max_depth': 10, 'max_features': 10, 'max_leaf_nodes': None, 'min_samples_leaf': 1, 'n_estimators': 200	0.239	97.227	0.553
CH	RFR	6	'max_depth': 10, 'max_features': 'sqrt', 'max_leaf_nodes': None, 'min_samples_leaf': 1, 'n_estimators': 100	0.221	94.349	0.55
CH	RFR	7	'max_depth': None, 'max_features': 10, 'max_leaf_nodes': 10, 'min_samples_leaf': 2, 'n_estimators': 100	0.254	100.899	0.571
CH	RFR	8	'max_depth': 5, 'max_features': 'sqrt', 'max_leaf_nodes': 20, 'min_samples_leaf': 1, 'n_estimators': 200	0.217	99.517	0.578
CH	RFR	9	'max_depth': 5, 'max_features': 'sqrt', 'max_leaf_nodes': None, 'min_samples_leaf': 5, 'n_estimators': 200	0.172	104.461	0.593
CH	RFR	10	'max_depth': None, 'max_features': 'sqrt', 'max_leaf_nodes': None, 'min_samples_leaf': 2, 'n_estimators': 500	0.243	97.024	0.548
CH	SVR	1	'svr__C': 10, 'svr__epsilon': 0.01, 'svr__gamma': 'scale', 'svr__kernel': 'linear'	0.323	95.135	0.555
CH	SVR	2	'svr__C': 1, 'svr__epsilon': 1, 'svr__gamma': 'scale', 'svr__kernel': 'linear'	0.22	96.989	0.554
CH	SVR	3	'svr__C': 100, 'svr__epsilon': 1, 'svr__gamma': 'scale', 'svr__kernel': 'linear'	0.182	96.688	0.558
CH	SVR	4	'svr__C': 1, 'svr__epsilon': 1, 'svr__gamma': 'scale', 'svr__kernel': 'linear'	0.22	98.606	0.566
CH	SVR	5	'svr__C': 100, 'svr__epsilon': 0.01, 'svr__gamma': 'auto', 'svr__kernel': 'rbf'	0.294	93.806	0.527
CH	SVR	6	'svr__C': 10, 'svr__epsilon': 0.01, 'svr__gamma': 'scale', 'svr__kernel': 'linear'	0.228	96.36	0.563
CH	SVR	7	'svr__C': 100, 'svr__epsilon': 1, 'svr__gamma': 'scale', 'svr__kernel': 'linear'	0.296	93.581	0.531
CH	SVR	8	'svr__C': 1, 'svr__epsilon': 1, 'svr__gamma': 'scale', 'svr__kernel': 'linear'	0.259	96.224	0.555
CH	SVR	9	'svr__C': 10, 'svr__epsilon': 0.1, 'svr__gamma': 'scale', 'svr__kernel': 'linear'	0.227	96.138	0.549
CH	SVR	10	'svr__C': 1, 'svr__epsilon': 1, 'svr__gamma': 'scale', 'svr__kernel': 'linear'	0.205	97.674	0.555
CH	XGB	1	'xgb__colsample_bytree': 0.8, 'xgb__gamma': 0, 'xgb__learning_rate': 0.01, 'xgb__max_depth': 7, 'xgb__n_estimators': 300, 'xgb__subsample': 1.0	0.198	96.853	0.574
CH	XGB	2	'xgb__colsample_bytree': 0.8, 'xgb__gamma': 0, 'xgb__learning_rate': 0.1, 'xgb__max_depth': 3, 'xgb__n_estimators': 100, 'xgb__subsample': 0.8	0.217	99.454	0.567
CH	XGB	3	'xgb__colsample_bytree': 0.8, 'xgb__gamma': 0, 'xgb__learning_rate': 0.1, 'xgb__max_depth': 9, 'xgb__n_estimators': 100, 'xgb__subsample': 1.0	0.181	102.339	0.603
CH	XGB	4	'xgb__colsample_bytree': 0.8, 'xgb__gamma': 0.2, 'xgb__learning_rate': 0.2, 'xgb__max_depth': 7, 'xgb__n_estimators': 100, 'xgb__subsample': 0.8	0.243	98.511	0.562
CH	XGB	5	'xgb__colsample_bytree': 1.0, 'xgb__gamma': 0.2, 'xgb__learning_rate': 0.2, 'xgb__max_depth': 7, 'xgb__n_estimators': 200, 'xgb__subsample': 0.8	0.225	90.404	0.523
CH	XGB	6	'xgb__colsample_bytree': 0.8, 'xgb__gamma': 0.1, 'xgb__learning_rate': 0.1, 'xgb__max_depth': 7, 'xgb__n_estimators': 300, 'xgb__subsample': 0.8	0.266	90.79	0.529
CH	XGB	7	'xgb__colsample_bytree': 0.8, 'xgb__gamma': 0, 'xgb__learning_rate': 0.01, 'xgb__max_depth': 3, 'xgb__n_estimators': 300, 'xgb__subsample': 1.0	0.16	98.689	0.579
CH	XGB	8	'xgb__colsample_bytree': 0.8, 'xgb__gamma': 0.1, 'xgb__learning_rate': 0.1, 'xgb__max_depth': 7, 'xgb__n_estimators': 300, 'xgb__subsample': 1.0	0.229	93.968	0.555
CH	XGB	9	'xgb__colsample_bytree': 0.8, 'xgb__gamma': 0, 'xgb__learning_rate': 0.1, 'xgb__max_depth': 7, 'xgb__n_estimators': 100, 'xgb__subsample': 0.8	0.157	101.16	0.583
CH	XGB	10	'xgb__colsample_bytree': 1.0, 'xgb__gamma': 0.1, 'xgb__learning_rate': 0.1, 'xgb__max_depth': 5, 'xgb__n_estimators': 300, 'xgb__subsample': 0.8	0.249	97.957	0.562
CH	GPR	1	1.04**2 * RBF(length_scale=0.555)	0.03	112.276	0.669
CH	GPR	2	1.09**2 * RBF(length_scale=0.614)	0.034	113.143	0.66
CH	GPR	3	1.11**2 * RBF(length_scale=0.717)	0.046	116.921	0.679
CH	GPR	4	1.05**2 * RBF(length_scale=0.542)	0.091	117.013	0.691

CH	GPR	5	1.05**2 * RBF(length_scale=0.663)	0.071	111.359	0.644
CH	GPR	6	1.07**2 * RBF(length_scale=0.643)	0.089	110.957	0.655
CH	GPR	7	1.06**2 * RBF(length_scale=0.699)	0.075	111.392	0.646
CH	GPR	8	1.06**2 * RBF(length_scale=0.677)	0.054	107.571	0.631
CH	GPR	9	1.07**2 * RBF(length_scale=0.607)	0.063	119.623	0.693
CH	GPR	10	1.06**2 * RBF(length_scale=0.603)	0.043	114.67	0.672
ALB	RFR	1	'max_depth': None, 'max_features': 'sqrt', 'max_leaf_nodes': None, 'min_samples_leaf': 5, 'n_estimators': 100	0.492	61.884	0.447
ALB	RFR	2	'max_depth': None, 'max_features': 'sqrt', 'max_leaf_nodes': None, 'min_samples_leaf': 5, 'n_estimators': 500	0.389	62.498	0.463
ALB	RFR	3	'max_depth': None, 'max_features': 'sqrt', 'max_leaf_nodes': 10, 'min_samples_leaf': 5, 'n_estimators': 100	0.47	60.956	0.444
ALB	RFR	4	'max_depth': 5, 'max_features': 10, 'max_leaf_nodes': 10, 'min_samples_leaf': 5, 'n_estimators': 200	0.473	59.714	0.439
ALB	RFR	5	'max_depth': 5, 'max_features': 10, 'max_leaf_nodes': 10, 'min_samples_leaf': 1, 'n_estimators': 100	0.491	57.978	0.418
ALB	RFR	6	'max_depth': None, 'max_features': 'sqrt', 'max_leaf_nodes': 10, 'min_samples_leaf': 2, 'n_estimators': 100	0.598	54.306	0.388
ALB	RFR	7	'max_depth': 5, 'max_features': 'sqrt', 'max_leaf_nodes': 20, 'min_samples_leaf': 1, 'n_estimators': 100	0.599	54.284	0.395
ALB	RFR	8	'max_depth': None, 'max_features': 10, 'max_leaf_nodes': 10, 'min_samples_leaf': 5, 'n_estimators': 200	0.487	61.801	0.451
ALB	RFR	9	'max_depth': 5, 'max_features': 10, 'max_leaf_nodes': 10, 'min_samples_leaf': 5, 'n_estimators': 200	0.511	60.256	0.437
ALB	RFR	10	'max_depth': None, 'max_features': 10, 'max_leaf_nodes': None, 'min_samples_leaf': 5, 'n_estimators': 100	0.484	61.236	0.445
ALB	SVR	1	'svr__C': 10, 'svr__epsilon': 0.01, 'svr__gamma': 'scale', 'svr__kernel': 'linear'	0.527	60.243	0.435
ALB	SVR	2	'svr__C': 10, 'svr__epsilon': 0.5, 'svr__gamma': 'scale', 'svr__kernel': 'linear'	0.465	58.95	0.435
ALB	SVR	3	'svr__C': 10, 'svr__epsilon': 0.01, 'svr__gamma': 'scale', 'svr__kernel': 'linear'	0.488	59.269	0.431
ALB	SVR	4	'svr__C': 10, 'svr__epsilon': 1, 'svr__gamma': 'scale', 'svr__kernel': 'linear'	0.502	59.348	0.434
ALB	SVR	5	'svr__C': 10, 'svr__epsilon': 0.01, 'svr__gamma': 'scale', 'svr__kernel': 'linear'	0.572	54.454	0.393
ALB	SVR	6	'svr__C': 100, 'svr__epsilon': 1, 'svr__gamma': 1, 'svr__kernel': 'rbf'	0.6	56.361	0.406
ALB	SVR	7	'svr__C': 10, 'svr__epsilon': 1, 'svr__gamma': 'scale', 'svr__kernel': 'linear'	0.624	55.656	0.406
ALB	SVR	8	'svr__C': 10, 'svr__epsilon': 1, 'svr__gamma': 'scale', 'svr__kernel': 'linear'	0.512	63.062	0.458
ALB	SVR	9	'svr__C': 100, 'svr__epsilon': 0.01, 'svr__gamma': 'scale', 'svr__kernel': 'linear'	0.571	59.17	0.428
ALB	SVR	10	'svr__C': 100, 'svr__epsilon': 1, 'svr__gamma': 'scale', 'svr__kernel': 'rbf'	0.517	59.66	0.436
ALB	XGB	1	'xgb__colsample_bytree': 1.0, 'xgb__gamma': 0.1, 'xgb__learning_rate': 0.2, 'xgb__max_depth': 5, 'xgb__n_estimators': 100, 'xgb__subsample': 0.8	0.494	63.028	0.454
ALB	XGB	2	'xgb__colsample_bytree': 0.8, 'xgb__gamma': 0.2, 'xgb__learning_rate': 0.01, 'xgb__max_depth': 3, 'xgb__n_estimators': 200, 'xgb__subsample': 0.8	0.366	63.793	0.47
ALB	XGB	3	'xgb__colsample_bytree': 1.0, 'xgb__gamma': 0.1, 'xgb__learning_rate': 0.1, 'xgb__max_depth': 3, 'xgb__n_estimators': 100, 'xgb__subsample': 1.0	0.525	60.109	0.44
ALB	XGB	4	'xgb__colsample_bytree': 0.8, 'xgb__gamma': 0, 'xgb__learning_rate': 0.01, 'xgb__max_depth': 5, 'xgb__n_estimators': 200, 'xgb__subsample': 0.8	0.509	57.863	0.424
ALB	XGB	5	'xgb__colsample_bytree': 1.0, 'xgb__gamma': 0, 'xgb__learning_rate': 0.01, 'xgb__max_depth': 3, 'xgb__n_estimators': 300, 'xgb__subsample': 1.0	0.506	56.811	0.411
ALB	XGB	6	'xgb__colsample_bytree': 1.0, 'xgb__gamma': 0.2, 'xgb__learning_rate': 0.1, 'xgb__max_depth': 3, 'xgb__n_estimators': 100, 'xgb__subsample': 0.8	0.62	51.448	0.367
ALB	XGB	7	'xgb__colsample_bytree': 0.8, 'xgb__gamma': 0, 'xgb__learning_rate': 0.01, 'xgb__max_depth': 3, 'xgb__n_estimators': 300, 'xgb__subsample': 0.8	0.627	51.687	0.375
ALB	XGB	8	'xgb__colsample_bytree': 1.0, 'xgb__gamma': 0, 'xgb__learning_rate': 0.01, 'xgb__max_depth': 3, 'xgb__n_estimators': 300, 'xgb__subsample': 0.8	0.502	61.415	0.448
ALB	XGB	9	'xgb__colsample_bytree': 1.0, 'xgb__gamma': 0.1, 'xgb__learning_rate': 0.2, 'xgb__max_depth': 5, 'xgb__n_estimators': 100, 'xgb__subsample': 0.8	0.56	58.001	0.416
ALB	XGB	10	'xgb__colsample_bytree': 1.0, 'xgb__gamma': 0, 'xgb__learning_rate': 0.01, 'xgb__max_depth': 3, 'xgb__n_estimators': 200, 'xgb__subsample': 0.8	0.499	60.569	0.44
ALB	GPR	1	0.969**2 * RBF(length_scale=0.582)	0.364	70.641	0.51
ALB	GPR	2	0.988**2 * RBF(length_scale=0.571)	0.229	73.522	0.554
ALB	GPR	3	0.971**2 * RBF(length_scale=0.596)	0.312	73.961	0.551
ALB	GPR	4	1**2 * RBF(length_scale=0.602)	0.263	70.827	0.523
ALB	GPR	5	0.963**2 * RBF(length_scale=0.637)	0.346	69.188	0.506
ALB	GPR	6	0.954**2 * RBF(length_scale=0.728)	0.577	57.247	0.409
ALB	GPR	7	0.988**2 * RBF(length_scale=0.69)	0.418	66.398	0.487
ALB	GPR	8	0.96**2 * RBF(length_scale=0.603)	0.327	70.746	0.512
ALB	GPR	9	0.981**2 * RBF(length_scale=0.68)	0.503	61.572	0.445

ALB	GPR	10	0.978**2 * RBF(length_scale=0.592)	0.437	67.059	0.49
HAI	RFR	1	'max_depth': 10, 'max_features': 'sqrt', 'max_leaf_nodes': 20, 'min_samples_leaf': 2, 'n_estimators': 500	0.601	58.344	0.484
HAI	RFR	2	'max_depth': 5, 'max_features': 'sqrt', 'max_leaf_nodes': None, 'min_samples_leaf': 2, 'n_estimators': 200	0.567	58.231	0.481
HAI	RFR	3	'max_depth': 5, 'max_features': 'sqrt', 'max_leaf_nodes': 20, 'min_samples_leaf': 1, 'n_estimators': 200	0.494	60.211	0.51
HAI	RFR	4	'max_depth': 5, 'max_features': 'sqrt', 'max_leaf_nodes': None, 'min_samples_leaf': 5, 'n_estimators': 200	0.626	55.599	0.471
HAI	RFR	5	'max_depth': None, 'max_features': 'sqrt', 'max_leaf_nodes': 20, 'min_samples_leaf': 1, 'n_estimators': 100	0.563	57.184	0.48
HAI	RFR	6	'max_depth': 10, 'max_features': 'sqrt', 'max_leaf_nodes': None, 'min_samples_leaf': 1, 'n_estimators': 100	0.677	50.357	0.443
HAI	RFR	7	'max_depth': None, 'max_features': 'sqrt', 'max_leaf_nodes': None, 'min_samples_leaf': 5, 'n_estimators': 100	0.546	59.045	0.504
HAI	RFR	8	'max_depth': 5, 'max_features': 'sqrt', 'max_leaf_nodes': None, 'min_samples_leaf': 1, 'n_estimators': 500	0.593	56.409	0.471
HAI	RFR	9	'max_depth': 15, 'max_features': 'sqrt', 'max_leaf_nodes': None, 'min_samples_leaf': 1, 'n_estimators': 100	0.555	60.494	0.516
HAI	RFR	10	'max_depth': None, 'max_features': 'sqrt', 'max_leaf_nodes': None, 'min_samples_leaf': 5, 'n_estimators': 100	0.544	59.877	0.509
HAI	SVR	1	'svr__C': 100, 'svr__epsilon': 0.1, 'svr__gamma': 'scale', 'svr__kernel': 'linear'	0.64	55.258	0.461
HAI	SVR	2	'svr__C': 100, 'svr__epsilon': 1, 'svr__gamma': 'scale', 'svr__kernel': 'linear'	0.591	55.823	0.463
HAI	SVR	3	'svr__C': 100, 'svr__epsilon': 1, 'svr__gamma': 'scale', 'svr__kernel': 'linear'	0.637	52.765	0.447
HAI	SVR	4	'svr__C': 100, 'svr__epsilon': 0.1, 'svr__gamma': 'scale', 'svr__kernel': 'linear'	0.67	51.742	0.438
HAI	SVR	5	'svr__C': 100, 'svr__epsilon': 1, 'svr__gamma': 'scale', 'svr__kernel': 'linear'	0.572	55.933	0.469
HAI	SVR	6	'svr__C': 100, 'svr__epsilon': 1, 'svr__gamma': 'scale', 'svr__kernel': 'linear'	0.646	50.297	0.441
HAI	SVR	7	'svr__C': 100, 'svr__epsilon': 1, 'svr__gamma': 'scale', 'svr__kernel': 'linear'	0.624	53.9	0.458
HAI	SVR	8	'svr__C': 100, 'svr__epsilon': 1, 'svr__gamma': 'scale', 'svr__kernel': 'linear'	0.687	50.765	0.423
HAI	SVR	9	'svr__C': 100, 'svr__epsilon': 1, 'svr__gamma': 'scale', 'svr__kernel': 'linear'	0.579	59.724	0.506
HAI	SVR	10	'svr__C': 100, 'svr__epsilon': 0.5, 'svr__gamma': 'scale', 'svr__kernel': 'linear'	0.631	53.207	0.447
HAI	XGB	1	'xgb__colsample_bytree': 1.0, 'xgb__gamma': 0.2, 'xgb__learning_rate': 0.2, 'xgb__max_depth': 3, 'xgb__n_estimators': 300, 'xgb__subsample': 1.0	0.597	59.358	0.491
HAI	XGB	2	'xgb__colsample_bytree': 1.0, 'xgb__gamma': 0, 'xgb__learning_rate': 0.2, 'xgb__max_depth': 3, 'xgb__n_estimators': 100, 'xgb__subsample': 0.8	0.571	58.098	0.48
HAI	XGB	3	'xgb__colsample_bytree': 0.8, 'xgb__gamma': 0, 'xgb__learning_rate': 0.01, 'xgb__max_depth': 3, 'xgb__n_estimators': 300, 'xgb__subsample': 0.8	0.476	61.115	0.517
HAI	XGB	4	'xgb__colsample_bytree': 0.8, 'xgb__gamma': 0, 'xgb__learning_rate': 0.01, 'xgb__max_depth': 3, 'xgb__n_estimators': 300, 'xgb__subsample': 1.0	0.587	59.375	0.501
HAI	XGB	5	'xgb__colsample_bytree': 1.0, 'xgb__gamma': 0.1, 'xgb__learning_rate': 0.1, 'xgb__max_depth': 3, 'xgb__n_estimators': 100, 'xgb__subsample': 0.8	0.508	64.257	0.54
HAI	XGB	6	'xgb__colsample_bytree': 0.8, 'xgb__gamma': 0, 'xgb__learning_rate': 0.01, 'xgb__max_depth': 3, 'xgb__n_estimators': 300, 'xgb__subsample': 1.0	0.62	54.179	0.475
HAI	XGB	7	'xgb__colsample_bytree': 0.8, 'xgb__gamma': 0.1, 'xgb__learning_rate': 0.2, 'xgb__max_depth': 9, 'xgb__n_estimators': 100, 'xgb__subsample': 0.8	0.483	64.233	0.548
HAI	XGB	8	'xgb__colsample_bytree': 0.8, 'xgb__gamma': 0, 'xgb__learning_rate': 0.1, 'xgb__max_depth': 3, 'xgb__n_estimators': 100, 'xgb__subsample': 0.8	0.611	56.071	0.467
HAI	XGB	9	'xgb__colsample_bytree': 0.8, 'xgb__gamma': 0, 'xgb__learning_rate': 0.01, 'xgb__max_depth': 3, 'xgb__n_estimators': 200, 'xgb__subsample': 0.8	0.484	64.76	0.548
HAI	XGB	10	'xgb__colsample_bytree': 0.8, 'xgb__gamma': 0, 'xgb__learning_rate': 0.01, 'xgb__max_depth': 3, 'xgb__n_estimators': 200, 'xgb__subsample': 0.8	0.464	64.489	0.545
HAI	GPR	1	1.13**2 * RBF(length_scale=0.956)	0.491	68.263	0.569
HAI	GPR	2	1.05**2 * RBF(length_scale=0.939)	0.564	61.494	0.498
HAI	GPR	3	1.04**2 * RBF(length_scale=0.817)	0.443	65.875	0.557
HAI	GPR	4	1.01**2 * RBF(length_scale=0.866)	0.541	62.848	0.531
HAI	GPR	5	1.04**2 * RBF(length_scale=0.87)	0.489	61.989	0.516
HAI	GPR	6	0.944**2 * RBF(length_scale=0.82)	0.477	59.248	0.52
HAI	GPR	7	1.06**2 * RBF(length_scale=0.87)	0.469	66.942	0.564
HAI	GPR	8	1.03**2 * RBF(length_scale=0.835)	0.479	64.916	0.544
HAI	GPR	9	1.09**2 * RBF(length_scale=0.963)	0.512	62.062	0.53
HAI	GPR	10	1.03**2 * RBF(length_scale=0.853)	0.449	65.897	0.559
SCH	RFR	1	'max_depth': None, 'max_features': 'sqrt', 'max_leaf_nodes': 10, 'min_samples_leaf': 2, 'n_estimators': 200	0.354	95.411	0.432
SCH	RFR	2	'max_depth': 5, 'max_features': 'sqrt', 'max_leaf_nodes': 10, 'min_samples_leaf': 5, 'n_estimators': 100	0.328	94.618	0.427
SCH	RFR	3	'max_depth': 5, 'max_features': 'sqrt', 'max_leaf_nodes': 10, 'min_samples_leaf': 2, 'n_estimators': 100	0.434	90.285	0.402
SCH	RFR	4	'max_depth': 5, 'max_features': 'sqrt', 'max_leaf_nodes': None, 'min_samples_leaf': 1, 'n_estimators': 100	0.331	98.242	0.435

SCH	RFR	5	'max_depth': None, 'max_features': 'sqrt', 'max_leaf_nodes': 10, 'min_samples_leaf': 1, 'n_estimators': 100	0.343	97.047	0.445
SCH	RFR	6	'max_depth': 5, 'max_features': 10, 'max_leaf_nodes': 10, 'min_samples_leaf': 5, 'n_estimators': 100	0.39	94.588	0.421
SCH	RFR	7	'max_depth': None, 'max_features': 'sqrt', 'max_leaf_nodes': 10, 'min_samples_leaf': 2, 'n_estimators': 200	0.361	101.901	0.456
SCH	RFR	8	'max_depth': 10, 'max_features': 'sqrt', 'max_leaf_nodes': None, 'min_samples_leaf': 2, 'n_estimators': 100	0.408	94.495	0.423
SCH	RFR	9	'max_depth': 10, 'max_features': 'sqrt', 'max_leaf_nodes': None, 'min_samples_leaf': 2, 'n_estimators': 500	0.323	100.8	0.448
SCH	RFR	10	'max_depth': 5, 'max_features': 'sqrt', 'max_leaf_nodes': 20, 'min_samples_leaf': 2, 'n_estimators': 100	0.333	101.181	0.454
SCH	SVR	1	'svr__C': 100, 'svr__epsilon': 1, 'svr__gamma': 'scale', 'svr__kernel': 'rbf'	0.354	93.693	0.423
SCH	SVR	2	'svr__C': 100, 'svr__epsilon': 1, 'svr__gamma': 'scale', 'svr__kernel': 'linear'	0.361	93.28	0.418
SCH	SVR	3	'svr__C': 100, 'svr__epsilon': 1, 'svr__gamma': 'scale', 'svr__kernel': 'rbf'	0.421	93.033	0.413
SCH	SVR	4	'svr__C': 100, 'svr__epsilon': 0.01, 'svr__gamma': 'scale', 'svr__kernel': 'rbf'	0.425	91.405	0.404
SCH	SVR	5	'svr__C': 100, 'svr__epsilon': 1, 'svr__gamma': 'scale', 'svr__kernel': 'rbf'	0.368	92.754	0.421
SCH	SVR	6	'svr__C': 100, 'svr__epsilon': 1, 'svr__gamma': 'scale', 'svr__kernel': 'linear'	0.428	92.56	0.41
SCH	SVR	7	'svr__C': 100, 'svr__epsilon': 0.01, 'svr__gamma': 'scale', 'svr__kernel': 'rbf'	0.362	100.513	0.445
SCH	SVR	8	'svr__C': 100, 'svr__epsilon': 1, 'svr__gamma': 'scale', 'svr__kernel': 'linear'	0.474	94.222	0.425
SCH	SVR	9	'svr__C': 100, 'svr__epsilon': 1, 'svr__gamma': 'scale', 'svr__kernel': 'rbf'	0.408	95.513	0.426
SCH	SVR	10	'svr__C': 100, 'svr__epsilon': 0.01, 'svr__gamma': 'scale', 'svr__kernel': 'rbf'	0.454	92.601	0.416
SCH	XGB	1	'xgb__colsample_bytree': 1.0, 'xgb__gamma': 0, 'xgb__learning_rate': 0.01, 'xgb__max_depth': 3, 'xgb__n_estimators': 300, 'xgb__subsample': 1.0	0.313	97.182	0.439
SCH	XGB	2	'xgb__colsample_bytree': 0.8, 'xgb__gamma': 0, 'xgb__learning_rate': 0.01, 'xgb__max_depth': 3, 'xgb__n_estimators': 200, 'xgb__subsample': 0.8	0.271	99.375	0.451
SCH	XGB	3	'xgb__colsample_bytree': 0.8, 'xgb__gamma': 0.1, 'xgb__learning_rate': 0.01, 'xgb__max_depth': 7, 'xgb__n_estimators': 200, 'xgb__subsample': 1.0	0.425	92.165	0.41
SCH	XGB	4	'xgb__colsample_bytree': 0.8, 'xgb__gamma': 0, 'xgb__learning_rate': 0.01, 'xgb__max_depth': 3, 'xgb__n_estimators': 300, 'xgb__subsample': 0.8	0.302	98.417	0.436
SCH	XGB	5	'xgb__colsample_bytree': 1.0, 'xgb__gamma': 0, 'xgb__learning_rate': 0.01, 'xgb__max_depth': 3, 'xgb__n_estimators': 200, 'xgb__subsample': 0.8	0.303	97.967	0.448
SCH	XGB	6	'xgb__colsample_bytree': 0.8, 'xgb__gamma': 0, 'xgb__learning_rate': 0.01, 'xgb__max_depth': 3, 'xgb__n_estimators': 200, 'xgb__subsample': 1.0	0.41	94.208	0.42
SCH	XGB	7	'xgb__colsample_bytree': 0.8, 'xgb__gamma': 0, 'xgb__learning_rate': 0.01, 'xgb__max_depth': 3, 'xgb__n_estimators': 300, 'xgb__subsample': 0.8	0.363	105.444	0.473
SCH	XGB	8	'xgb__colsample_bytree': 0.8, 'xgb__gamma': 0, 'xgb__learning_rate': 0.01, 'xgb__max_depth': 3, 'xgb__n_estimators': 300, 'xgb__subsample': 0.8	0.392	94.985	0.422
SCH	XGB	9	'xgb__colsample_bytree': 1.0, 'xgb__gamma': 0, 'xgb__learning_rate': 0.01, 'xgb__max_depth': 3, 'xgb__n_estimators': 200, 'xgb__subsample': 0.8	0.291	103.28	0.459
SCH	XGB	10	'xgb__colsample_bytree': 1.0, 'xgb__gamma': 0, 'xgb__learning_rate': 0.01, 'xgb__max_depth': 3, 'xgb__n_estimators': 300, 'xgb__subsample': 0.8	0.314	102.488	0.461
SCH	GPR	1	1.03**2 * RBF(length_scale=0.542)	0.055	112.547	0.511
SCH	GPR	2	1**2 * RBF(length_scale=0.0912)	0	116.645	0.531
SCH	GPR	3	1.05**2 * RBF(length_scale=0.664)	0.028	116.241	0.518
SCH	GPR	4	1.05**2 * RBF(length_scale=0.624)	0.067	119.988	0.532
SCH	GPR	5	1.04**2 * RBF(length_scale=0.653)	0.146	110.328	0.505
SCH	GPR	6	1.04**2 * RBF(length_scale=0.618)	0.009	121.548	0.542
SCH	GPR	7	1.07**2 * RBF(length_scale=0.817)	0.149	119.432	0.537
SCH	GPR	8	1.04**2 * RBF(length_scale=0.679)	0.221	106.116	0.476
SCH	GPR	9	1.06**2 * RBF(length_scale=0.831)	0.245	105.753	0.473
SCH	GPR	10	1.05**2 * RBF(length_scale=0.671)	0.051	120.172	0.539
US	RFR	1	'max_depth': None, 'max_features': 10, 'max_leaf_nodes': 10, 'min_samples_leaf': 1, 'n_estimators': 100	0.433	68.608	0.267
US	RFR	2	'max_depth': 5, 'max_features': 10, 'max_leaf_nodes': 10, 'min_samples_leaf': 2, 'n_estimators': 200	0.444	63.617	0.25
US	RFR	3	'max_depth': None, 'max_features': 10, 'max_leaf_nodes': None, 'min_samples_leaf': 5, 'n_estimators': 500	0.379	67.218	0.259
US	RFR	4	'max_depth': 5, 'max_features': 10, 'max_leaf_nodes': 10, 'min_samples_leaf': 2, 'n_estimators': 200	0.461	70.669	0.281
US	RFR	5	'max_depth': 5, 'max_features': 10, 'max_leaf_nodes': 10, 'min_samples_leaf': 2, 'n_estimators': 100	0.451	66.11	0.254
US	RFR	6	'max_depth': None, 'max_features': 'sqrt', 'max_leaf_nodes': 10, 'min_samples_leaf': 2, 'n_estimators': 200	0.422	64.712	0.261
US	RFR	7	'max_depth': None, 'max_features': 10, 'max_leaf_nodes': 20, 'min_samples_leaf': 1, 'n_estimators': 100	0.377	74.124	0.29
US	RFR	8	'max_depth': None, 'max_features': 10, 'max_leaf_nodes': None, 'min_samples_leaf': 5, 'n_estimators': 100	0.395	67.47	0.26
US	RFR	9	'max_depth': None, 'max_features': 10, 'max_leaf_nodes': 10, 'min_samples_leaf': 1, 'n_estimators': 100	0.417	68.961	0.266

US	RFR	10	'max_depth': None, 'max_features': 10, 'max_leaf_nodes': None, 'min_samples_leaf': 5, 'n_estimators': 100	0.308	71.819	0.279
US	SVR	1	'svr__C': 100, 'svr__epsilon': 1, 'svr__gamma': 'scale', 'svr__kernel': 'linear'	0.494	62.487	0.24
US	SVR	2	'svr__C': 100, 'svr__epsilon': 0.01, 'svr__gamma': 'scale', 'svr__kernel': 'linear'	0.602	50.272	0.197
US	SVR	3	'svr__C': 100, 'svr__epsilon': 0.01, 'svr__gamma': 'scale', 'svr__kernel': 'linear'	0.496	61.333	0.235
US	SVR	4	'svr__C': 100, 'svr__epsilon': 1, 'svr__gamma': 'scale', 'svr__kernel': 'linear'	0.531	60.381	0.236
US	SVR	5	'svr__C': 100, 'svr__epsilon': 1, 'svr__gamma': 'scale', 'svr__kernel': 'linear'	0.547	60.469	0.232
US	SVR	6	'svr__C': 100, 'svr__epsilon': 0.5, 'svr__gamma': 'scale', 'svr__kernel': 'linear'	0.569	52.136	0.207
US	SVR	7	'svr__C': 100, 'svr__epsilon': 0.1, 'svr__gamma': 'scale', 'svr__kernel': 'linear'	0.562	60.417	0.236
US	SVR	8	'svr__C': 100, 'svr__epsilon': 1, 'svr__gamma': 'scale', 'svr__kernel': 'linear'	0.432	64.762	0.248
US	SVR	9	'svr__C': 100, 'svr__epsilon': 1, 'svr__gamma': 'scale', 'svr__kernel': 'linear'	0.455	64.825	0.247
US	SVR	10	'svr__C': 100, 'svr__epsilon': 1, 'svr__gamma': 'scale', 'svr__kernel': 'linear'	0.449	63.514	0.244
US	XGB	1	'xgb__colsample_bytree': 0.8, 'xgb__gamma': 0, 'xgb__learning_rate': 0.01, 'xgb__max_depth': 5, 'xgb__n_estimators': 200, 'xgb__subsample': 0.8	0.411	69.243	0.268
US	XGB	2	'xgb__colsample_bytree': 1.0, 'xgb__gamma': 0, 'xgb__learning_rate': 0.2, 'xgb__max_depth': 3, 'xgb__n_estimators': 100, 'xgb__subsample': 0.8	0.398	66.15	0.258
US	XGB	3	'xgb__colsample_bytree': 1.0, 'xgb__gamma': 0, 'xgb__learning_rate': 0.1, 'xgb__max_depth': 3, 'xgb__n_estimators': 300, 'xgb__subsample': 0.8	0.375	67.86	0.258
US	XGB	4	'xgb__colsample_bytree': 0.8, 'xgb__gamma': 0, 'xgb__learning_rate': 0.01, 'xgb__max_depth': 5, 'xgb__n_estimators': 200, 'xgb__subsample': 0.8	0.376	76.427	0.302
US	XGB	5	'xgb__colsample_bytree': 1.0, 'xgb__gamma': 0, 'xgb__learning_rate': 0.01, 'xgb__max_depth': 3, 'xgb__n_estimators': 200, 'xgb__subsample': 1.0	0.502	64.874	0.252
US	XGB	6	'xgb__colsample_bytree': 1.0, 'xgb__gamma': 0.2, 'xgb__learning_rate': 0.1, 'xgb__max_depth': 3, 'xgb__n_estimators': 300, 'xgb__subsample': 0.8	0.403	66.616	0.267
US	XGB	7	'xgb__colsample_bytree': 1.0, 'xgb__gamma': 0.2, 'xgb__learning_rate': 0.01, 'xgb__max_depth': 7, 'xgb__n_estimators': 200, 'xgb__subsample': 0.8	0.35	74.251	0.291
US	XGB	8	'xgb__colsample_bytree': 1.0, 'xgb__gamma': 0, 'xgb__learning_rate': 0.01, 'xgb__max_depth': 3, 'xgb__n_estimators': 300, 'xgb__subsample': 1.0	0.364	67.505	0.258
US	XGB	9	'xgb__colsample_bytree': 1.0, 'xgb__gamma': 0.1, 'xgb__learning_rate': 0.2, 'xgb__max_depth': 7, 'xgb__n_estimators': 100, 'xgb__subsample': 1.0	0.355	68.738	0.261
US	XGB	10	'xgb__colsample_bytree': 1.0, 'xgb__gamma': 0, 'xgb__learning_rate': 0.01, 'xgb__max_depth': 5, 'xgb__n_estimators': 200, 'xgb__subsample': 1.0	0.384	67.266	0.263
US	GPR	1	1.2**2 * RBF(length_scale=0.816)	0.255	83.361	0.323
US	GPR	2	1.06**2 * RBF(length_scale=0.696)	0.294	68.962	0.269
US	GPR	3	1.14**2 * RBF(length_scale=0.79)	0.21	80.838	0.31
US	GPR	4	1.12**2 * RBF(length_scale=0.725)	0.147	88.532	0.347
US	GPR	5	1.21**2 * RBF(length_scale=0.898)	0.207	85.777	0.33
US	GPR	6	1.06**2 * RBF(length_scale=0.661)	0.248	71.481	0.283
US	GPR	7	1.11**2 * RBF(length_scale=0.646)	0.182	87.213	0.341
US	GPR	8	1.1**2 * RBF(length_scale=0.744)	0.213	82.567	0.314
US	GPR	9	1.19**2 * RBF(length_scale=0.814)	0.167	82.955	0.317
US	GPR	10	1.1**2 * RBF(length_scale=0.718)	0.156	80.403	0.313

56

Section A.5: Cross-validation performance of local physically-based models

Table A.2: Cross-validation performance of local physically-based models. The parameters correspond to the best-performing combination of parameters tested during the fivefold cross-validation. CH: Switzerland, ALB: Schwäbische Alb, HAI: Hainich-Dün, SCH: Schorfheide-Chorin, US: United States, R^2: coefficient of determination, RMSE: root-mean-square error, RRMSE: relative root-mean-square error.

Site	Seed	Cost function	Percentage of solutions	R^2	RMSE [g m^{-2}]	RRMSE
CH	1	min_contrast_1	1	0.221	95.683	0.556
CH	2	min_contrast_1	1	0.214	96.421	0.558
CH	3	min_contrast_1	1	0.149	107.756	0.617
CH	4	min_contrast_1	1	0.142	104.529	0.602
CH	5	min_contrast_1	1	0.207	102.279	0.589
CH	6	min_contrast_1	1	0.211	96.402	0.558
CH	7	min_contrast_1	1	0.208	101.18	0.583
CH	8	min_contrast_1	1	0.192	98.848	0.573
CH	9	min_contrast_1	1	0.23	101.751	0.583
CH	10	min_contrast_2	1	0.263	97.142	0.558
ALB	1	neyman_chi_square_divergence	1	0.419	72.6	0.521
ALB	2	neyman_chi_square_divergence	1	0.392	70.695	0.512
ALB	3	neyman_chi_square_divergence	1	0.401	73.617	0.525
ALB	4	neyman_chi_square_divergence	1	0.399	71.542	0.518
ALB	5	neyman_chi_square_divergence	1	0.491	67.975	0.491
ALB	6	neyman_chi_square_divergence	1	0.519	67.184	0.483
ALB	7	neyman_chi_square_divergence	1	0.488	68.575	0.496
ALB	8	neyman_chi_square_divergence	1	0.404	71.385	0.511
ALB	9	neyman_chi_square_divergence	1	0.424	70.498	0.505
ALB	10	neyman_chi_square_divergence	1	0.406	70.858	0.508
HAI	1	neyman_chi_square_divergence	1	0.535	76.289	0.653
HAI	2	neyman_chi_square_divergence	1	0.502	79.265	0.68
HAI	3	neyman_chi_square_divergence	1	0.488	77.544	0.67
HAI	4	neyman_chi_square_divergence	1	0.521	79.296	0.682
HAI	5	neyman_chi_square_divergence	1	0.471	79.608	0.683
HAI	6	neyman_chi_square_divergence	1	0.56	74.294	0.65
HAI	7	neyman_chi_square_divergence	1	0.496	78.714	0.679
HAI	8	neyman_chi_square_divergence	1	0.494	78.26	0.673
HAI	9	neyman_chi_square_divergence	1	0.513	79.514	0.678
HAI	10	neyman_chi_square_divergence	1	0.465	80.354	0.691
SCH	1	laplace_distribution	10	0.232	100.658	0.459
SCH	2	laplace_distribution	10	0.258	99.444	0.451
SCH	3	laplace_distribution	10	0.253	105.421	0.475
SCH	4	laplace_distribution	10	0.252	105.525	0.475
SCH	5	laplace_distribution	10	0.25	99.303	0.451
SCH	6	laplace_distribution	10	0.265	104.778	0.471

SCH	7	laplace_distribution	10	0.237	107.39	0.481
SCH	8	laplace_distribution	10	0.249	105.4	0.473
SCH	9	laplace_distribution	10	0.234	107.052	0.48
SCH	10	laplace_distribution	10	0.235	106.999	0.481
US	1	pearson_chi_square	0.01	0.11	179.487	0.684
US	2	pearson_chi_square	0.01	0.102	173.848	0.67
US	3	min_contrast_4	10	0.411	182.307	0.695
US	4	min_contrast_4	10	0.394	182.016	0.694
US	5	pearson_chi_square	0.01	0.119	176.744	0.674
US	6	pearson_chi_square	0.01	0.101	174.832	0.673
US	7	min_contrast_4	10	0.419	180.943	0.689
US	8	min_contrast_4	10	0.417	181.294	0.692
US	9	min_contrast_4	10	0.434	181.748	0.693
US	10	pearson_chi_square	0.01	0.117	175.263	0.671

Section A.6: Cross-validation performance of local hybrid models

Table A.3: Cross-validation performance of local hybrid models. The parameters correspond to the best-performing combination of parameters tested during the fivefold cross-validation using Active Learning with an initial training set size of 2%. CH: Switzerland, ALB: Schwäbische Alb, HAI: Hainich-Dün, SCH: Schorfheide-Chorin, US: United States, GPR: Gaussian Process regression, R^2: coefficient of determination, RMSE: root-mean-square error, RRMSE: relative root-mean-square error. Nomenclature of parameter names for GPR according to Pedregosa et al. (2012).

Site	Model	Seed	Parameters	R^2	RMSE [g m^{-2}]	RRMSE
CH	GPR	1	2.21**2 * RBF(length_scale=1.42)	0.499	75.556	0.439
CH	GPR	2	1.38**2 * RBF(length_scale=1.19)	0.452	79.347	0.459
CH	GPR	3	2.3**2 * RBF(length_scale=1.31)	0.352	91.03	0.521
CH	GPR	4	1.65**2 * RBF(length_scale=1.54)	0.391	86.625	0.499
CH	GPR	5	1.4**2 * RBF(length_scale=1.12)	0.443	83.088	0.478
CH	GPR	6	1.35**2 * RBF(length_scale=0.905)	0.294	90.317	0.523
CH	GPR	7	2.17**2 * RBF(length_scale=1.44)	0.454	83.176	0.479
CH	GPR	8	1.86**2 * RBF(length_scale=1.39)	0.528	75.341	0.437
CH	GPR	9	2.01**2 * RBF(length_scale=1.55)	0.373	88.788	0.509
CH	GPR	10	1.88**2 * RBF(length_scale=1.51)	0.416	85.856	0.493
ALB	GPR	1	1.48**2 * RBF(length_scale=1.53)	0.598	54.526	0.391
ALB	GPR	2	1.55**2 * RBF(length_scale=1.18)	0.522	57.823	0.418
ALB	GPR	3	1.71**2 * RBF(length_scale=1.43)	0.59	55.424	0.396
ALB	GPR	4	1.23**2 * RBF(length_scale=1.06)	0.553	55.795	0.404
ALB	GPR	5	1.22**2 * RBF(length_scale=1.05)	0.651	49.486	0.357
ALB	GPR	6	1.24**2 * RBF(length_scale=0.967)	0.662	50.024	0.36
ALB	GPR	7	1.22**2 * RBF(length_scale=0.924)	0.585	54.581	0.395
ALB	GPR	8	1.46**2 * RBF(length_scale=1.77)	0.607	53.931	0.386
ALB	GPR	9	1.38**2 * RBF(length_scale=1.05)	0.605	54.212	0.388
ALB	GPR	10	1.39**2 * RBF(length_scale=1.13)	0.557	57.082	0.409
HAI	GPR	1	1.11**2 * RBF(length_scale=0.986)	0.626	55.158	0.472
HAI	GPR	2	1.61**2 * RBF(length_scale=1.39)	0.567	57.636	0.494
HAI	GPR	3	1.56**2 * RBF(length_scale=1.17)	0.558	58.089	0.502
HAI	GPR	4	1.23**2 * RBF(length_scale=1.22)	0.599	56.084	0.483
HAI	GPR	5	1.18**2 * RBF(length_scale=0.916)	0.558	58.565	0.503
HAI	GPR	6	1.34**2 * RBF(length_scale=0.889)	0.669	46.253	0.405
HAI	GPR	7	1.36**2 * RBF(length_scale=0.949)	0.551	59.404	0.512
HAI	GPR	8	1.22**2 * RBF(length_scale=1.2)	0.593	55.635	0.478
HAI	GPR	9	1.35**2 * RBF(length_scale=0.994)	0.582	58.676	0.5
HAI	GPR	10	1.07**2 * RBF(length_scale=0.729)	0.439	64.907	0.558
SCH	GPR	1	1.43**2 * RBF(length_scale=1.66)	0.42	87.105	0.397
SCH	GPR	2	2.41**2 * RBF(length_scale=1.88)	0.413	87.669	0.398
SCH	GPR	3	1.1**2 * RBF(length_scale=0.739)	0.265	103.892	0.468
SCH	GPR	4	1.67**2 * RBF(length_scale=1.46)	0.42	92.083	0.414
SCH	GPR	5	1.28**2 * RBF(length_scale=1.18)	0.419	88.073	0.4

SCH	GPR	6	1.22**2 * RBF(length_scale=0.963)	0.358	97.48	0.438
SCH	GPR	7	2.21**2 * RBF(length_scale=1.73)	0.347	98.593	0.442
SCH	GPR	8	1.87**2 * RBF(length_scale=1.72)	0.472	87.585	0.393
SCH	GPR	9	1.13**2 * RBF(length_scale=0.843)	0.313	101.202	0.454
SCH	GPR	10	1.5**2 * RBF(length_scale=1.22)	0.422	95.264	0.428
US	GPR	1	1**2 * RBF(length_scale=0.15)	0	87.721	0.334
US	GPR	2	1**2 * RBF(length_scale=0.0601)	0	78.583	0.303
US	GPR	3	1**2 * RBF(length_scale=0.107)	0	87.481	0.334
US	GPR	4	2.88**2 * RBF(length_scale=1.72)	0.522	62.153	0.237
US	GPR	5	1.73**2 * RBF(length_scale=1.58)	0.523	60.741	0.232
US	GPR	6	1**2 * RBF(length_scale=0.215)	0	78.953	0.304
US	GPR	7	2.27**2 * RBF(length_scale=1.37)	0.652	53.078	0.202
US	GPR	8	1**2 * RBF(length_scale=0.371)	0	87.852	0.335
US	GPR	9	1.67**2 * RBF(length_scale=1.35)	0.652	52.129	0.199
US	GPR	10	1**2 * RBF(length_scale=0.119)	0	85.523	0.328

70

Section A.7: Cross-validation performance of global empirical models

Table A.4: Cross-validation performance of global empirical models. The parameters correspond to the best-performing combination of parameters tested during the fivefold cross-validation. CH: Switzerland, ALB: Schwäbische Alb, HAI: Hainich-Dün, SCH: Schorfheide-Chorin, US: United States, RFR: Random Forest regression, SVR: Support Vector regression, XGB: Extreme Gradient Boosting regression, GPR: Gaussian Process regression, R^2: coefficient of determination, RMSE: root-mean-square error, RRMSE: relative root-mean-square error. Nomenclature of parameter names for RFR, SVR, and GPR according to Pedregosa et al. (2012), for XGB according to Chen and Guestrin (2016).

Site	Model	Parameters	R^2	RMSE [g m^{-2}]	RRMSE
All except for CH	RFR	'max_depth': None, 'max_features': 'sqrt', 'max_leaf_nodes': None, 'min_samples_leaf': 2, 'n_estimators': 200	0.506	79.86	0.433
All except for CH	SVR	'svr__C': 100, 'svr__epsilon': 0.1, 'svr__gamma': 'scale', 'svr__kernel': 'rbf'	0.522	78.95	0.427
All except for CH	XGB	'xgb__colsample_bytree': 1.0, 'xgb__gamma': 0.1, 'xgb__learning_rate': 0.01, 'xgb__max_depth': 3, 'xgb__n_estimators': 300, 'xgb__subsample': 0.8	0.5	80.664	0.437
All except for CH	GPR	1**2 * RBF(length_scale=0.0279)	0.398	88.272	0.478
All except for ALB	RFR	'max_depth': 10, 'max_features': 'sqrt', 'max_leaf_nodes': None, 'min_samples_leaf': 1, 'n_estimators': 100	0.399	90.335	0.467
All except for ALB	SVR	'svr__C': 100, 'svr__epsilon': 1, 'svr__gamma': 'scale', 'svr__kernel': 'rbf'	0.379	92.708	0.479
All except for ALB	XGB	'xgb__colsample_bytree': 1.0, 'xgb__gamma': 0.2, 'xgb__learning_rate': 0.1, 'xgb__max_depth': 9, 'xgb__n_estimators': 100, 'xgb__subsample': 0.8	0.377	93.213	0.482
All except for ALB	GPR	1**2 * RBF(length_scale=0.0285)	0.083	109.705	0.567
All except for HAI	RFR	'max_depth': 10, 'max_features': 'sqrt', 'max_leaf_nodes': None, 'min_samples_leaf': 2, 'n_estimators': 500	0.328	91.829	0.462
All except for HAI	SVR	'svr__C': 100, 'svr__epsilon': 1, 'svr__gamma': 'scale', 'svr__kernel': 'rbf'	0.359	90.446	0.454
All except for HAI	XGB	'xgb__colsample_bytree': 1.0, 'xgb__gamma': 0, 'xgb__learning_rate': 0.01, 'xgb__max_depth': 3, 'xgb__n_estimators': 300, 'xgb__subsample': 0.8	0.294	94.275	0.474
All except for HAI	GPR	1**2 * RBF(length_scale=0.0297)	0.001	111.558	0.562
All except for SCH	RFR	'max_depth': 10, 'max_features': 10, 'max_leaf_nodes': None, 'min_samples_leaf': 1, 'n_estimators': 500	0.49	77.84	0.449
All except for SCH	SVR	'svr__C': 100, 'svr__epsilon': 1, 'svr__gamma': 'scale', 'svr__kernel': 'rbf'	0.439	82.674	0.477
All except for SCH	XGB	'xgb__colsample_bytree': 1.0, 'xgb__gamma': 0.2, 'xgb__learning_rate': 0.01, 'xgb__max_depth': 7, 'xgb__n_estimators': 300, 'xgb__subsample': 0.8	0.463	79.584	0.459
All except for SCH	GPR	1**2 * RBF(length_scale=0.0273)	0.298	90.679	0.525
All except for US	RFR	'max_depth': 15, 'max_features': 'sqrt', 'max_leaf_nodes': None, 'min_samples_leaf': 2, 'n_estimators': 200	0.349	89.073	0.547
All except for US	SVR	'svr__C': 100, 'svr__epsilon': 1, 'svr__gamma': 'auto', 'svr__kernel': 'rbf'	0.366	89.059	0.546
All except for US	XGB	'xgb__colsample_bytree': 0.8, 'xgb__gamma': 0, 'xgb__learning_rate': 0.01, 'xgb__max_depth': 3, 'xgb__n_estimators': 300, 'xgb__subsample': 0.8	0.324	90.521	0.556
All except for US	GPR	1**2 * RBF(length_scale=0.0292)	0.161	101.078	0.62

Section A.8: Cross-validation performance of global physically-based models

Table A.5: Cross-validation performance of global physically-based models. The parameters correspond to the best-performing combination of parameters tested during the fivefold cross-validation. CH: Switzerland, ALB: Schwäbische Alb, HAI: Hainich-Dün, SCH: Schorfheide-Chorin, US: United States, R^2: coefficient of determination, RMSE: root-mean-square error, RRMSE: relative root-mean-square error.

Site	Cost function	Percentage of solutions	R^2	RMSE [g m^{-2}]	RRMSE
All except for CH	laplace_distribution	1	0.034	120.649	0.653
All except for ALB	min_contrast_4	10	0.025	126.039	0.652
All except for HAI	min_contrast_4	10	0.025	124.348	0.625
All except for SCH	laplace_distribution	1	0.009	119.915	0.695
All except for US	min_contrast_1	1	0.266	93.696	0.576

Section A.9: Cross-validation performance of global hybrid models

Table A.6: Cross-validation performance of global hybrid models. The parameters correspond to the best-performing combination of parameters tested during the fivefold cross-validation using Active Learning with an initial training set size of 2%. CH: Switzerland, ALB: Schwäbische Alb, HAI: Hainich-Dün, SCH: Schorfheide-Chorin, US: United States, GPR: Gaussian Process regression, R^2: coefficient of determination, RMSE: root-mean-square error, RRMSE: relative root-mean-square error. Nomenclature of parameter names for GPR according to Pedregosa et al. (2012).

Site	Model	Parameters	R^2	RMSE [g m^{-2}]	RRMSE
All except for CH	GPR	1.39**2 * RBF(length_scale=1.29)	0.427	85.269	0.462
All except for ALB	GPR	1.82**2 * RBF(length_scale=1.41)	0.31	95.682	0.495
All except for HAI	GPR	1.26**2 * RBF(length_scale=1.11)	0.237	97.987	0.492
All except for SCH	GPR	1.63**2 * RBF(length_scale=1.26)	0.368	86.338	0.5
All except for US	GPR	1.16**2 * RBF(length_scale=1.09)	0.332	89.463	0.55

Section A.10: Testing performance of local and transferred empirical models: RFR

Table A.7: Testing performance of local and transferred empirical Random Forest regression (RFR) models. The parameters correspond to the best-performing combination of parameters tested during the fivefold cross-validation. CH: Switzerland, ALB: Schwäbische Alb, HAI: Hainich-Dün, SCH: Schorfheide-Chorin, US: United States, R^2: coefficient of determination, RMSE: root-mean-square error, sRMSE: systematic component of RMSE, uRMSE: unsystematic component of RMSE, RRMSE: relative root-mean-square error, MBE: mean bias error.

		Training site				
Prediction site	**Metric**	**CH**	**ALB**	**HAI**	**SCH**	**US**
CH	**R^2**	0.30 ± 0.14	0.15 ± 0.02	0.01 ± 0.01	0.15 ± 0.02	0.01 ± 0.01
	RMSE	97.67 ± 14.48	120.81 ± 2.34	142.25 ± 6.22	112.16 ± 5.87	231.97 ± 32.68
	sRMSE	113.35 ± 9.02	127.81 ± 2.37	140.14 ± 6.24	112.57 ± 1.81	219.95 ± 26.43
	uRMSE	59.82 ± 8.76	41.61 ± 3.19	23.47 ± 6.62	29.93 ± 6.00	71.03 ± 27.47
	RRMSE	0.56 ± 0.08	0.70 ± 0.01	0.82 ± 0.04	0.65 ± 0.03	1.34 ± 0.19
	MBE	-1.62 ± 14.43	-65.16 ± 4.60	-86.25 ± 10.08	22.32 ± 9.96	189.73 ± 30.65
ALB	**R^2**	0.28 ± 0.08	0.51 ± 0.17	0.34 ± 0.02	0.49 ± 0.03	0.30 ± 0.02
	RMSE	126.00 ± 13.26	61.60 ± 10.74	73.85 ± 1.20	104.79 ± 8.47	260.84 ± 43.11
	sRMSE	132.69 ± 11.92	85.05 ± 4.28	87.37 ± 0.61	116.88 ± 4.64	260.01 ± 38.75
	uRMSE	40.51 ± 7.35	55.77 ± 15.19	46.59 ± 2.52	50.43 ± 9.42	46.06 ± 12.45
	RRMSE	0.91 ± 0.10	0.44 ± 0.07	0.53 ± 0.01	0.75 ± 0.06	1.87 ± 0.31
	MBE	101.83 ± 15.73	3.44 ± 12.53	-22.47 ± 2.40	80.84 ± 6.72	245.55 ± 41.03
HAI	**R^2**	0.32 ± 0.07	0.45 ± 0.02	0.64 ± 0.11	0.43 ± 0.05	0.22 ± 0.05
	RMSE	138.66 ± 14.88	63.99 ± 1.42	50.73 ± 12.60	101.03 ± 4.03	293.26 ± 41.64
	sRMSE	145.82 ± 14.20	85.35 ± 0.16	82.50 ± 9.68	114.20 ± 2.13	292.95 ± 39.55
	uRMSE	44.38 ± 6.74	56.44 ± 1.60	64.28 ± 5.88	52.93 ± 4.83	32.06 ± 12.20
	RRMSE	1.20 ± 0.13	0.55 ± 0.01	0.44 ± 0.10	0.87 ± 0.03	2.53 ± 0.36
	MBE	117.78 ± 17.85	4.41 ± 2.84	-4.10 ± 6.45	76.01 ± 3.20	279.96 ± 41.41
SCH	**R^2**	0.19 ± 0.06	0.31 ± 0.02	0.16 ± 0.02	0.32 ± 0.09	0.09 ± 0.01
	RMSE	114.93 ± 5.97	123.22 ± 1.85	139.90 ± 1.74	103.30 ± 10.26	227.35 ± 45.71
	sRMSE	124.93 ± 5.18	138.81 ± 1.69	147.01 ± 0.98	120.49 ± 11.52	226.85 ± 41.93
	uRMSE	48.12 ± 8.52	63.90 ± 1.65	44.88 ± 4.71	60.01 ± 16.54	39.01 ± 12.37
	RRMSE	0.52 ± 0.03	0.56 ± 0.01	0.63 ± 0.01	0.46 ± 0.04	1.02 ± 0.21
	MBE	33.07 ± 20.17	-71.83 ± 3.28	-86.43 ± 1.67	0.70 ± 11.84	191.27 ± 49.71
US	**R^2**	0.16 ± 0.14	0.32 ± 0.08	0.17 ± 0.16	0.28 ± 0.09	0.47 ± 0.16
	RMSE	173.22 ± 9.53	225.50 ± 3.77	226.10 ± 2.65	173.05 ± 8.70	64.73 ± 11.41
	sRMSE	175.60 ± 9.71	227.59 ± 3.44	226.95 ± 3.07	176.04 ± 8.23	84.35 ± 12.85
	uRMSE	26.53 ± 12.43	30.41 ± 4.20	20.87 ± 6.78	31.94 ± 3.65	51.43 ± 17.73
	RRMSE	0.66 ± 0.04	0.86 ± 0.01	0.86 ± 0.01	0.66 ± 0.03	0.25 ± 0.04
	MBE	-153.32 ± 11.21	-211.03 ± 3.71	-210.25 ± 3.37	-153.95 ± 9.37	0.12 ± 11.91

Section A.11: Testing performance of local and transferred empirical models: SVR

Table A.8: Testing performance of local and transferred empirical Support Vector regression (SVR) models. The parameters correspond to the best-performing combination of parameters tested during the fivefold cross-validation. CH: Switzerland, ALB: Schwäbische Alb, HAI: Hainich-Dün, SCH: Schorfheide-Chorin, US: United States, R^2: coefficient of determination, RMSE: root-mean-square error, sRMSE: systematic component of RMSE, uRMSE: unsystematic component of RMSE, RRMSE: relative root-mean-square error, MBE: mean bias error.

		Training site				
Prediction site	**Metric**	**CH**	**ALB**	**HAI**	**SCH**	**US**
CH	**R^2**	0.31 ± 0.12	0.26 ± 0.13	0.01 ± 0.01	0.11 ± 0.16	0.06 ± 0.04
	RMSE	96.29 ± 6.44	149.67 ± 19.71	195.16 ± 16.16	132.08 ± 27.73	293.03 ± 57.49
	sRMSE	113.92 ± 9.04	158.61 ± 23.47	185.72 ± 17.25	132.78 ± 33.06	276.07 ± 48.37
	uRMSE	58.90 ± 16.63	53.39 ± 16.13	57.92 ± 14.39	33.89 ± 17.02	94.87 ± 42.37
	RRMSE	0.55 ± 0.03	0.86 ± 0.11	1.12 ± 0.09	0.76 ± 0.16	1.69 ± 0.33
	MBE	-13.29 ± 13.09	-111.13 ± 36.03	-148.94 ± 20.88	-33.73 ± 73.95	251.96 ± 53.69
ALB	**R^2**	0.46 ± 0.12	0.54 ± 0.21	0.47 ± 0.02	0.49 ± 0.04	0.25 ± 0.16
	RMSE	97.08 ± 16.87	59.48 ± 13.07	74.84 ± 3.45	89.75 ± 5.74	280.34 ± 30.59
	sRMSE	109.51 ± 15.79	85.21 ± 4.86	93.83 ± 2.46	106.39 ± 4.62	280.43 ± 29.37
	uRMSE	55.63 ± 2.48	59.73 ± 12.97	56.52 ± 1.47	57.02 ± 0.99	38.65 ± 18.03
	RRMSE	0.70 ± 0.12	0.43 ± 0.09	0.54 ± 0.02	0.64 ± 0.04	2.01 ± 0.22
	MBE	67.46 ± 23.94	-6.35 ± 12.74	-40.95 ± 5.37	64.65 ± 7.68	267.23 ± 30.84
HAI	**R^2**	0.39 ± 0.04	0.49 ± 0.05	0.65 ± 0.08	0.48 ± 0.05	0.33 ± 0.15
	RMSE	107.06 ± 17.05	62.67 ± 2.62	52.62 ± 11.00	88.42 ± 5.75	281.21 ± 27.60
	sRMSE	115.94 ± 14.23	85.91 ± 0.48	83.64 ± 10.87	105.76 ± 3.62	283.83 ± 26.66
	uRMSE	51.46 ± 5.24	58.60 ± 3.47	64.67 ± 6.39	57.80 ± 2.59	42.84 ± 10.99
	RRMSE	0.92 ± 0.15	0.54 ± 0.02	0.45 ± 0.08	0.76 ± 0.05	2.42 ± 0.24
	MBE	77.08 ± 20.47	-10.15 ± 5.00	-13.82 ± 9.06	62.53 ± 6.07	270.58 ± 27.97
SCH	**R^2**	0.33 ± 0.08	0.35 ± 0.06	0.24 ± 0.02	0.42 ± 0.15	0.18 ± 0.07
	RMSE	108.79 ± 10.83	129.53 ± 3.18	139.75 ± 2.47	94.39 ± 8.53	224.30 ± 24.65
	sRMSE	122.02 ± 2.28	146.39 ± 2.76	150.82 ± 1.61	120.78 ± 11.39	226.29 ± 23.89
	uRMSE	60.96 ± 4.19	67.90 ± 6.16	56.62 ± 2.66	73.64 ± 17.66	30.70 ± 17.05
	RRMSE	0.49 ± 0.05	0.58 ± 0.01	0.63 ± 0.01	0.42 ± 0.04	1.01 ± 0.11
	MBE	-14.42 ± 23.94	-85.56 ± 4.82	-92.86 ± 2.62	-8.22 ± 12.60	191.96 ± 28.19
US	**R^2**	0.30 ± 0.03	0.27 ± 0.10	0.32 ± 0.05	0.23 ± 0.05	0.59 ± 0.08
	RMSE	212.61 ± 50.25	259.17 ± 42.80	272.06 ± 35.13	206.50 ± 124.22	56.89 ± 12.09
	sRMSE	216.26 ± 49.34	261.03 ± 44.64	275.78 ± 35.18	201.94 ± 127.46	84.09 ± 12.92
	uRMSE	37.24 ± 10.22	38.86 ± 11.65	44.91 ± 4.87	36.01 ± 10.46	61.61 ± 7.79
	RRMSE	0.81 ± 0.19	0.99 ± 0.16	1.04 ± 0.13	0.79 ± 0.47	0.22 ± 0.04
	MBE	-197.74 ± 53.27	-245.99 ± 48.23	-262.03 ± 37.05	-173.23 ± 140.11	5.06 ± 9.42

Section A.12: Testing performance of local and transferred empirical models: XGB

Table A.9: Testing performance of local and transferred empirical Extreme Gradient Boosting (XGB) regression models. The parameters correspond to the best-performing combination of parameters tested during the fivefold cross-validation. CH: Switzerland, ALB: Schwäbische Alb, HAI: Hainich-Dün, SCH: Schorfheide-Chorin, US: United States, R^2: coefficient of determination, RMSE: root-mean-square error, sRMSE: systematic component of RMSE, uRMSE: unsystematic component of RMSE, RRMSE: relative root-mean-square error, MBE: mean bias error.

		Training site				
Prediction site	**Metric**	**CH**	**ALB**	**HAI**	**SCH**	**US**
CH	**R^2**	0.21 ± 0.12	0.14 ± 0.04	0.03 ± 0.02	0.12 ± 0.02	0.01 ± 0.01
	RMSE	108.91 ± 14.41	120.79 ± 3.77	135.00 ± 7.13	118.44 ± 9.55	245.19 ± 28.16
	sRMSE	114.75 ± 9.07	126.57 ± 3.28	122.35 ± 8.47	115.46 ± 4.44	226.56 ± 20.67
	uRMSE	45.54 ± 17.66	36.60 ± 9.39	55.24 ± 13.55	32.39 ± 14.39	92.17 ± 25.75
	RRMSE	0.62 ± 0.08	0.70 ± 0.02	0.78 ± 0.04	0.68 ± 0.05	1.41 ± 0.16
	MBE	-4.43 ± 22.19	-62.52 ± 6.61	-50.27 ± 19.49	32.21 ± 15.07	197.58 ± 23.88
ALB	**R^2**	0.26 ± 0.08	0.52 ± 0.14	0.27 ± 0.04	0.43 ± 0.05	0.29 ± 0.04
	RMSE	160.89 ± 25.32	62.46 ± 9.74	80.56 ± 5.19	110.64 ± 11.96	276.58 ± 47.77
	sRMSE	160.00 ± 25.02	85.18 ± 4.05	85.99 ± 1.05	119.77 ± 6.70	271.73 ± 40.69
	uRMSE	30.33 ± 12.62	55.91 ± 12.22	31.39 ± 11.26	44.40 ± 11.66	48.92 ± 35.67
	RRMSE	1.16 ± 0.18	0.45 ± 0.07	0.58 ± 0.04	0.79 ± 0.09	1.99 ± 0.34
	MBE	134.91 ± 29.78	5.48 ± 12.68	-15.09 ± 5.91	84.81 ± 9.27	257.94 ± 42.81
HAI	**R^2**	0.28 ± 0.10	0.42 ± 0.03	0.60 ± 0.12	0.39 ± 0.07	0.21 ± 0.07
	RMSE	171.69 ± 29.31	66.22 ± 2.31	54.35 ± 12.33	104.55 ± 5.87	309.70 ± 49.19
	sRMSE	170.75 ± 27.39	85.31 ± 0.16	82.40 ± 9.71	115.71 ± 2.53	305.52 ± 44.89
	uRMSE	29.35 ± 16.82	53.67 ± 2.76	60.99 ± 7.58	48.62 ± 8.13	48.84 ± 29.02
	RRMSE	1.48 ± 0.25	0.57 ± 0.02	0.47 ± 0.09	0.90 ± 0.05	2.67 ± 0.42
	MBE	146.87 ± 32.43	1.04 ± 4.03	-1.05 ± 6.02	78.21 ± 3.66	293.04 ± 46.78
SCH	**R^2**	0.15 ± 0.05	0.30 ± 0.03	0.16 ± 0.03	0.28 ± 0.11	0.08 ± 0.02
	RMSE	143.38 ± 24.47	122.21 ± 1.83	138.84 ± 3.83	105.79 ± 10.74	245.25 ± 54.24
	sRMSE	144.35 ± 18.33	137.27 ± 1.59	145.15 ± 3.27	120.40 ± 11.45	240.77 ± 50.72
	uRMSE	41.01 ± 15.05	62.41 ± 3.65	42.00 ± 4.92	54.61 ± 18.41	42.26 ± 27.55
	RRMSE	0.65 ± 0.11	0.55 ± 0.01	0.63 ± 0.02	0.48 ± 0.04	1.11 ± 0.24
	MBE	73.97 ± 39.45	-68.78 ± 3.22	-83.11 ± 5.78	1.31 ± 10.30	207.36 ± 58.12
US	**R^2**	0.11 ± 0.07	0.01 ± 0.01	0.09 ± 0.11	0.20 ± 0.10	0.48 ± 0.14
	RMSE	188.78 ± 15.31	230.54 ± 10.24	218.55 ± 8.05	161.57 ± 10.24	70.77 ± 16.44
	sRMSE	190.10 ± 14.80	229.73 ± 9.88	218.53 ± 8.71	164.25 ± 9.59	85.74 ± 12.11
	uRMSE	28.13 ± 7.24	18.67 ± 5.59	25.85 ± 6.50	27.59 ± 10.06	57.22 ± 15.89
	RRMSE	0.72 ± 0.06	0.88 ± 0.04	0.84 ± 0.03	0.62 ± 0.04	0.27 ± 0.06
	MBE	-169.64 ± 16.38	-213.05 ± 10.63	-201.01 ± 9.52	-140.22 ± 11.11	8.79 ± 16.87

Section A.13: Testing performance of local and transferred empirical models: GPR

Table A.10: Testing performance of local and transferred empirical Gaussian Process regression (GPR) models. The parameters correspond to the best-performing combination of parameters tested during the fivefold cross-validation. CH: Switzerland, ALB: Schwäbische Alb, HAI: Hainich-Dün, SCH: Schorfheide-Chorin, US: United States, R^2: coefficient of determination, RMSE: root-mean-square error, sRMSE: systematic component of RMSE, uRMSE: unsystematic component of RMSE, RRMSE: relative root-mean-square error, MBE: mean bias error.

		Training site				
Prediction site	**Metric**	**CH**	**ALB**	**HAI**	**SCH**	**US**
CH	**R^2**	0.08 ± 0.05	0.04 ± 0.02	0.00 ± 0.01	0.01 ± 0.01	0.01 ± 0.00
	RMSE	111.15 ± 11.89	119.06 ± 0.86	127.48 ± 0.77	120.40 ± 0.54	141.09 ± 0.68
	sRMSE	112.90 ± 8.85	116.71 ± 0.31	126.56 ± 0.30	119.92 ± 0.44	141.15 ± 0.67
	uRMSE	29.83 ± 7.91	23.29 ± 3.44	14.59 ± 4.63	10.04 ± 6.02	4.10 ± 0.51
	RRMSE	0.64 ± 0.06	0.69 ± 0.00	0.73 ± 0.00	0.69 ± 0.00	0.81 ± 0.00
	MBE	-2.56 ± 6.57	-37.63 ± 0.98	-62.02 ± 0.58	47.10 ± 1.32	87.98 ± 1.09
ALB	**R^2**	0.08 ± 0.05	0.40 ± 0.17	0.30 ± 0.03	0.16 ± 0.06	0.03 ± 0.01
	RMSE	120.96 ± 8.61	68.44 ± 10.35	73.29 ± 2.35	117.93 ± 3.14	149.15 ± 0.93
	sRMSE	106.10 ± 4.70	84.25 ± 4.60	85.62 ± 0.56	121.40 ± 3.34	149.21 ± 0.91
	uRMSE	57.35 ± 11.71	49.63 ± 11.75	44.02 ± 4.02	27.76 ± 8.15	4.34 ± 1.28
	RRMSE	0.87 ± 0.06	0.49 ± 0.07	0.53 ± 0.02	0.85 ± 0.02	1.07 ± 0.01
	MBE	62.85 ± 7.90	3.40 ± 3.12	-13.74 ± 3.73	87.03 ± 4.69	122.53 ± 1.11
HAI	**R^2**	0.10 ± 0.02	0.31 ± 0.02	0.54 ± 0.17	0.18 ± 0.08	0.02 ± 0.00
	RMSE	139.71 ± 10.59	72.53 ± 1.41	58.39 ± 15.42	119.74 ± 6.59	169.59 ± 1.21
	sRMSE	124.83 ± 6.69	85.96 ± 0.43	83.06 ± 9.53	124.76 ± 4.28	169.53 ± 1.13
	uRMSE	62.36 ± 10.70	46.09 ± 1.54	57.05 ± 9.37	32.59 ± 11.80	4.80 ± 2.47
	RRMSE	1.20 ± 0.09	0.63 ± 0.01	0.50 ± 0.12	1.03 ± 0.06	1.46 ± 0.01
	MBE	90.08 ± 9.29	9.95 ± 3.68	-3.37 ± 11.12	90.80 ± 5.68	146.09 ± 1.31
SCH	**R^2**	0.03 ± 0.04	0.13 ± 0.01	0.16 ± 0.04	0.16 ± 0.11	0.01 ± 0.00
	RMSE	130.30 ± 5.04	132.47 ± 1.17	139.77 ± 3.58	114.35 ± 13.95	125.86 ± 0.39
	sRMSE	122.19 ± 1.57	138.90 ± 1.49	147.30 ± 2.73	120.78 ± 11.53	125.90 ± 0.36
	uRMSE	41.31 ± 19.05	41.74 ± 2.03	46.04 ± 6.08	42.75 ± 15.76	3.52 ± 1.53
	RRMSE	0.59 ± 0.02	0.60 ± 0.01	0.63 ± 0.02	0.51 ± 0.05	0.57 ± 0.00
	MBE	-24.84 ± 7.79	-71.68 ± 2.96	-86.85 ± 4.66	0.83 ± 12.62	39.83 ± 1.14
US	**R^2**	0.08 ± 0.05	0.04 ± 0.02	0.16 ± 0.04	0.09 ± 0.03	0.35 ± 0.07
	RMSE	124.71 ± 1.27	150.08 ± 0.78	170.72 ± 0.70	94.63 ± 0.49	71.05 ± 13.37
	sRMSE	123.64 ± 0.65	150.07 ± 0.70	170.33 ± 0.57	94.82 ± 0.49	84.52 ± 12.87
	uRMSE	14.83 ± 6.96	4.60 ± 1.81	11.10 ± 3.36	5.57 ± 2.35	45.13 ± 6.76
	RRMSE	0.48 ± 0.00	0.57 ± 0.00	0.65 ± 0.00	0.36 ± 0.00	0.27 ± 0.05
	MBE	-88.80 ± 0.88	-123.02 ± 0.86	-146.93 ± 0.65	-39.81 ± 1.23	2.37 ± 12.21

Section A.14: Testing performance of local and transferred physically-based models

Table A.11: Testing performance of local and transferred physically-based models. The parameters correspond to the best-performing combination of parameters tested during the fivefold cross-validation. CH: Switzerland, ALB: Schwäbische Alb, HAI: Hainich-Dün, SCH: Schorfheide-Chorin, US: United States, R^2: coefficient of determination, RMSE: root-mean-square error, sRMSE: systematic component of RMSE, uRMSE: unsystematic component of RMSE, RRMSE: relative root-mean-square error, MBE: mean bias error.

		Calibration site				
Prediction site	**Metric**	**CH**	**ALB**	**HAI**	**SCH**	**US**
CH	**R^2**	0.26 ± 0.17	0.14 ± 0.00	0.14 ± 0.00	0.12 ± 0.00	0.13 ± 0.00
	RMSE	102.57 ± 16.64	105.26 ± 0.00	105.26 ± 0.00	104.55 ± 0.00	111.23 ± 6.82
	sRMSE	115.97 ± 11.28	112.62 ± 0.00	112.62 ± 0.00	109.99 ± 0.00	111.71 ± 1.21
	uRMSE	56.88 ± 12.05	40.06 ± 0.00	40.06 ± 0.00	34.17 ± 0.00	35.29 ± 0.87
	RRMSE	0.59 ± 0.09	0.61 ± 0.00	0.61 ± 0.00	0.60 ± 0.00	0.64 ± 0.04
	MBE	-24.33 ± 15.87	-24.61 ± 0.00	-24.61 ± 0.00	-3.44 ± 0.00	-18.58 ± 7.28
ALB	**R^2**	0.41 ± 0.00	0.43 ± 0.17	0.43 ± 0.00	0.45 ± 0.00	0.22 ± 0.21
	RMSE	74.27 ± 0.25	73.17 ± 7.39	71.13 ± 0.00	87.55 ± 0.00	95.30 ± 9.71
	sRMSE	91.30 ± 0.15	90.63 ± 4.41	89.28 ± 0.00	103.76 ± 0.00	94.25 ± 7.34
	uRMSE	53.10 ± 0.09	51.44 ± 13.34	53.95 ± 0.00	55.69 ± 0.00	56.83 ± 2.11
	RRMSE	0.53 ± 0.00	0.52 ± 0.05	0.51 ± 0.00	0.63 ± 0.00	0.68 ± 0.07
	MBE	34.97 ± 0.37	32.34 ± 9.65	29.33 ± 0.00	60.49 ± 0.00	19.05 ± 37.63
HAI	**R^2**	0.53 ± 0.00	0.53 ± 0.00	0.66 ± 0.10	0.50 ± 0.00	0.26 ± 0.23
	RMSE	80.00 ± 0.20	76.46 ± 0.00	68.05 ± 7.50	98.54 ± 0.00	97.42 ± 2.45
	sRMSE	99.66 ± 0.12	96.69 ± 0.00	93.07 ± 7.16	115.10 ± 0.00	99.09 ± 12.78
	uRMSE	59.42 ± 0.06	59.18 ± 0.00	63.13 ± 6.46	59.47 ± 0.00	54.68 ± 4.44
	RRMSE	0.69 ± 0.00	0.66 ± 0.00	0.59 ± 0.05	0.85 ± 0.00	0.84 ± 0.02
	MBE	51.81 ± 0.23	45.83 ± 0.00	42.64 ± 7.51	77.44 ± 0.00	41.44 ± 31.11
SCH	**R^2**	0.21 ± 0.00	0.20 ± 0.00	0.20 ± 0.00	0.30 ± 0.04	0.12 ± 0.12
	RMSE	114.19 ± 0.09	116.67 ± 0.00	116.67 ± 0.00	103.95 ± 11.54	133.47 ± 27.96
	sRMSE	125.42 ± 0.08	127.32 ± 0.00	127.32 ± 0.00	120.51 ± 11.65	130.78 ± 11.16
	uRMSE	51.87 ± 0.01	50.98 ± 0.00	50.98 ± 0.00	60.75 ± 5.32	66.61 ± 10.26
	RRMSE	0.51 ± 0.00	0.53 ± 0.00	0.53 ± 0.00	0.47 ± 0.04	0.60 ± 0.13
	MBE	-40.07 ± 0.25	-45.64 ± 0.00	-45.64 ± 0.00	-9.99 ± 6.58	-45.40 ± 31.62
US	**R^2**	0.45 ± 0.00	0.44 ± 0.00	0.44 ± 0.00	0.43 ± 0.00	0.30 ± 0.24
	RMSE	196.60 ± 1.42	196.25 ± 0.00	196.25 ± 0.00	184.59 ± 0.00	185.01 ± 11.81
	sRMSE	201.31 ± 1.51	201.00 ± 0.00	201.00 ± 0.00	190.55 ± 0.00	187.33 ± 10.73
	uRMSE	43.27 ± 0.53	43.42 ± 0.00	43.42 ± 0.00	47.29 ± 0.00	36.63 ± 5.86
	RRMSE	0.75 ± 0.01	0.75 ± 0.00	0.75 ± 0.00	0.71 ± 0.00	0.71 ± 0.04
	MBE	-182.43 ± 1.66	-182.09 ± 0.00	-182.09 ± 0.00	-170.48 ± 0.00	-167.32 ± 6.38

Section A.15: Testing performance of local and transferred hybrid models

Table A.12: Testing performance of local and transferred hybrid models. The parameters correspond to the best-performing combination of parameters tested during the fivefold cross-validation using Active Learning with an initial training set size of 2%. CH: Switzerland, ALB: Schwäbische Alb, HAI: Hainich-Dün, SCH: Schorfheide-Chorin, US: United States, R^2: coefficient of determination, RMSE: root-mean-square error, sRMSE: systematic component of RMSE, uRMSE: unsystematic component of RMSE, RRMSE: relative root-mean-square error, MBE: mean bias error.

		Calibration site				
Prediction site	**Metric**	**CH**	**ALB**	**HAI**	**SCH**	**US**
CH	**R^2**	0.23 ± 0.14	0.02 ± 0.02	0.02 ± 0.03	0.03 ± 0.03	0.01 ± 0.01
	RMSE	112.22 ± 31.13	127.07 ± 7.94	125.43 ± 9.89	136.69 ± 13.00	164.02 ± 35.27
	sRMSE	113.87 ± 9.18	116.51 ± 7.64	117.34 ± 6.45	125.35 ± 13.19	146.02 ± 14.56
	uRMSE	54.73 ± 39.46	49.79 ± 13.76	44.33 ± 15.06	53.38 ± 17.36	58.53 ± 64.41
	RRMSE	0.64 ± 0.18	0.73 ± 0.05	0.72 ± 0.06	0.79 ± 0.07	0.94 ± 0.20
	MBE	-3.46 ± 17.01	-31.66 ± 21.59	-36.42 ± 18.12	36.96 ± 48.54	93.61 ± 20.14
ALB	**R^2**	0.07 ± 0.07	0.46 ± 0.18	0.34 ± 0.07	0.41 ± 0.09	0.03 ± 0.02
	RMSE	122.05 ± 8.44	64.39 ± 11.93	72.30 ± 4.12	107.21 ± 8.09	158.60 ± 28.14
	sRMSE	103.03 ± 10.46	84.85 ± 4.76	86.83 ± 1.25	118.81 ± 4.89	147.49 ± 33.86
	uRMSE	61.51 ± 21.43	54.13 ± 12.30	47.60 ± 5.58	50.35 ± 6.74	42.55 ± 41.87
	RRMSE	0.88 ± 0.06	0.46 ± 0.08	0.52 ± 0.03	0.77 ± 0.06	1.14 ± 0.20
	MBE	55.91 ± 19.27	-0.37 ± 11.47	-19.74 ± 5.34	83.55 ± 6.82	117.33 ± 42.37
HAI	**R^2**	0.03 ± 0.03	0.32 ± 0.04	0.54 ± 0.11	0.25 ± 0.06	0.02 ± 0.03
	RMSE	131.67 ± 12.72	72.81 ± 1.65	58.51 ± 11.47	110.02 ± 5.09	179.92 ± 31.30
	sRMSE	112.79 ± 15.17	86.15 ± 0.83	83.22 ± 9.76	115.72 ± 4.17	171.60 ± 35.17
	uRMSE	65.35 ± 16.62	45.90 ± 3.40	58.49 ± 6.67	35.08 ± 7.02	40.01 ± 41.06
	RRMSE	1.13 ± 0.11	0.63 ± 0.01	0.51 ± 0.09	0.95 ± 0.04	1.55 ± 0.27
	MBE	70.71 ± 24.06	0.42 ± 12.18	-9.55 ± 8.77	78.01 ± 6.21	146.89 ± 38.34
SCH	**R^2**	0.02 ± 0.02	0.23 ± 0.04	0.17 ± 0.07	0.27 ± 0.15	0.02 ± 0.03
	RMSE	142.90 ± 12.30	129.56 ± 8.21	144.81 ± 6.85	104.35 ± 14.22	144.01 ± 25.57
	sRMSE	129.70 ± 11.57	141.33 ± 6.42	152.09 ± 3.38	120.30 ± 11.46	132.76 ± 16.64
	uRMSE	58.91 ± 12.09	56.03 ± 4.71	44.91 ± 12.62	56.42 ± 18.15	46.69 ± 44.79
	RRMSE	0.64 ± 0.06	0.58 ± 0.04	0.65 ± 0.03	0.47 ± 0.06	0.65 ± 0.12
	MBE	-44.35 ± 27.74	-75.77 ± 12.38	-94.74 ± 5.45	-0.14 ± 8.90	39.24 ± 43.46
US	**R^2**	0.13 ± 0.10	0.12 ± 0.10	0.14 ± 0.11	0.19 ± 0.05	0.23 ± 0.26
	RMSE	184.27 ± 27.00	161.10 ± 38.01	155.40 ± 9.64	118.22 ± 23.46	76.40 ± 20.77
	sRMSE	171.80 ± 24.72	159.96 ± 38.99	148.05 ± 10.26	106.73 ± 19.36	84.04 ± 13.67
	uRMSE	63.41 ± 27.27	33.24 ± 13.22	45.41 ± 12.44	52.36 ± 23.27	22.45 ± 24.84
	RRMSE	0.70 ± 0.10	0.62 ± 0.15	0.59 ± 0.04	0.45 ± 0.09	0.29 ± 0.07
	MBE	-148.09 ± 28.52	-132.65 ± 46.57	-120.22 ± 12.54	-48.41 ± 44.96	0.49 ± 7.92

Section A.16: Testing performance of global models

Table A.13: Testing performance of global models. RFR: Random Forest regression, SVR: Support Vector regression, XGB: Extreme Gradient Boosting regression, GPR: Gaussian process regression, CH: Switzerland, ALB: Schwäbische Alb, HAI: Hainich-Dün, SCH: Schorfheide-Chorin, US: United States, R^2: coefficient of determination, RMSE: root-mean-square error, sRMSE: systematic component of RMSE, uRMSE: unsystematic component of RMSE, RRMSE: relative root-mean-square error, MBE: mean bias error.

		Model type					
Prediction site	**Metric**	**Empirical RFR**	**Empirical SVR**	**Empirical XGB**	**Empirical GPR**	**Physically-based**	**Hybrid**
CH	**R^2**	0	0.02	0	0	0.08	0
	RMSE	120.76	130.09	127.31	110.83	108.31	124.45
	sRMSE	110.28	111.77	110.95	110.83	110.73	112.64
	uRMSE	49.22	66.56	62.43	0	23.04	52.92
	RRMSE	0.7	0.75	0.73	0.64	0.62	0.72
	MBE	-2.51	-17.25	11.75	11	-12.76	22.71
ALB	**R^2**	0.41	0.49	0.42	0	0.43	0.43
	RMSE	82.9	68.51	83.38	100.75	85.6	74.31
	sRMSE	96.33	89.08	94.89	100.74	101.59	92.2
	uRMSE	49.06	56.93	45.28	1.41	54.72	54.58
	RRMSE	0.6	0.49	0.6	0.72	0.61	0.53
	MBE	46.55	28.87	43.51	54.13	56.67	37.3
HAI	**R^2**	0.44	0.43	0.34	0	0.49	0.42
	RMSE	85.81	76.13	93.5	119.47	94.98	73.71
	sRMSE	102.59	94.17	105.47	119.47	111.87	91.89
	uRMSE	56.22	55.43	48.81	0	59.12	54.87
	RRMSE	0.74	0.66	0.81	1.03	0.82	0.64
	MBE	57.15	40.11	62.07	83.08	72.55	34.41
SCH	**R^2**	0.28	0.27	0.29	0	0.22	0.18
	RMSE	117.09	127.69	116.49	129.1	111.52	134.26
	sRMSE	132.45	141.13	132.16	129.1	124.09	143.04
	uRMSE	61.9	60.12	62.42	0	54.43	49.34
	RRMSE	0.53	0.58	0.52	0.58	0.5	0.6
	MBE	-58.6	-76.21	-57.97	-49.32	-35.71	-79.54
US	**R^2**	0.28	0.05	0.2	0	0.45	0.25
	RMSE	211.53	224.32	211.52	130.9	197.08	136.03
	sRMSE	214.28	221.48	213.6	0	201.81	127.12
	uRMSE	34.21	35.59	29.74	0	43.45	48.43
	RRMSE	0.81	0.86	0.81	0.5	0.75	0.52
	MBE	-196.59	-204.11	-195.82	-98.89	-182.99	-93.37

Section A.17: Epistemic uncertainty

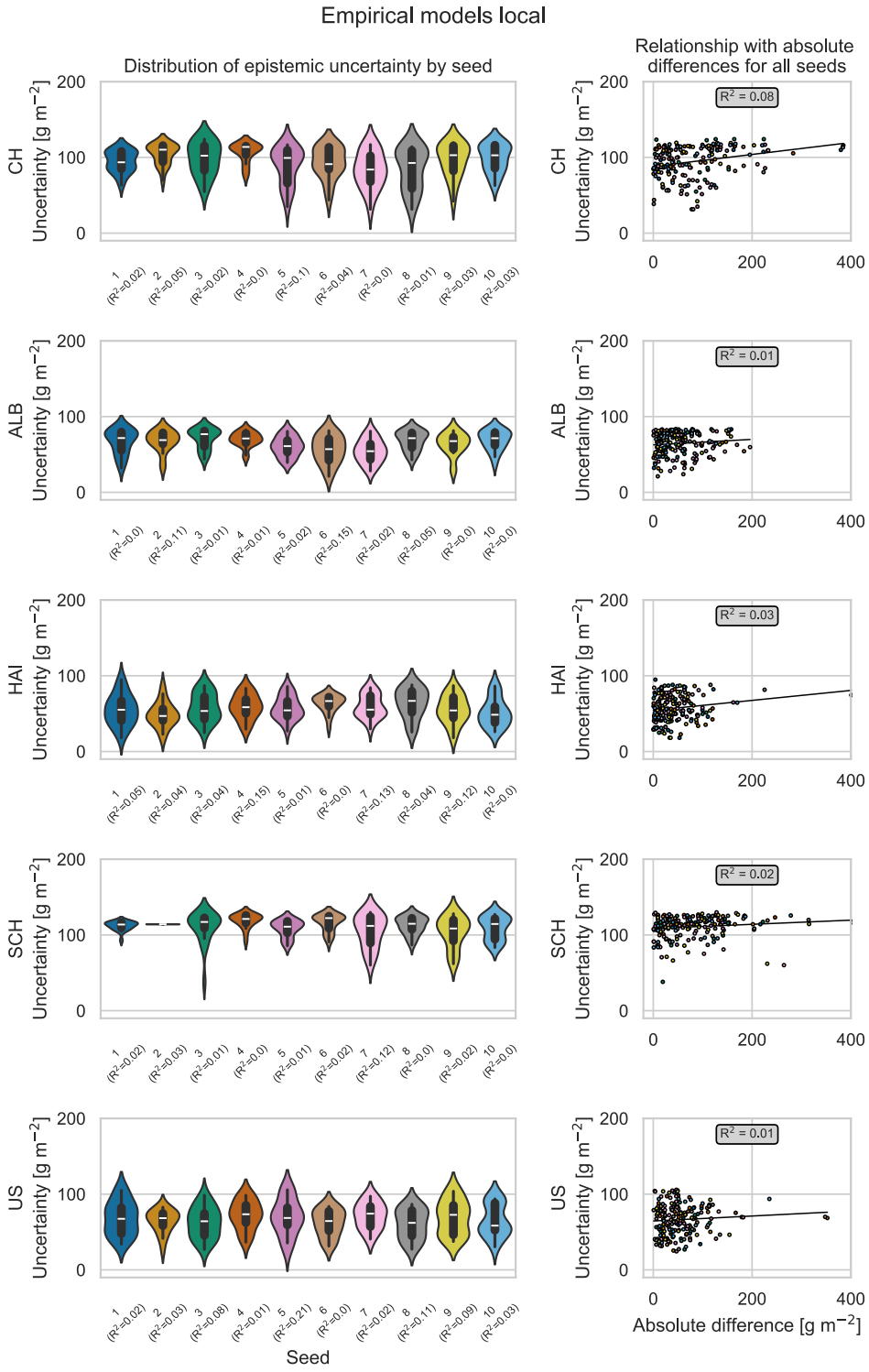

Figure A.3: Epistemic uncertainty of local empirical Gaussian process regression models. Absolute differences correspond to the absolute difference between measured and predicted biomass value. In case a model predicted a straight line (e.g., the prediction is constant), the calculation of the coefficient of determination (R^2) was not possible. The corresponding predictions were omitted for the calculation of the overall R^2 showed in the textbox in the right column. CH: Switzerland, ALB: Schwäbische Alb, HAI: Hainich-Dün, SCH: Schorfheide-Chorin, US: United States.

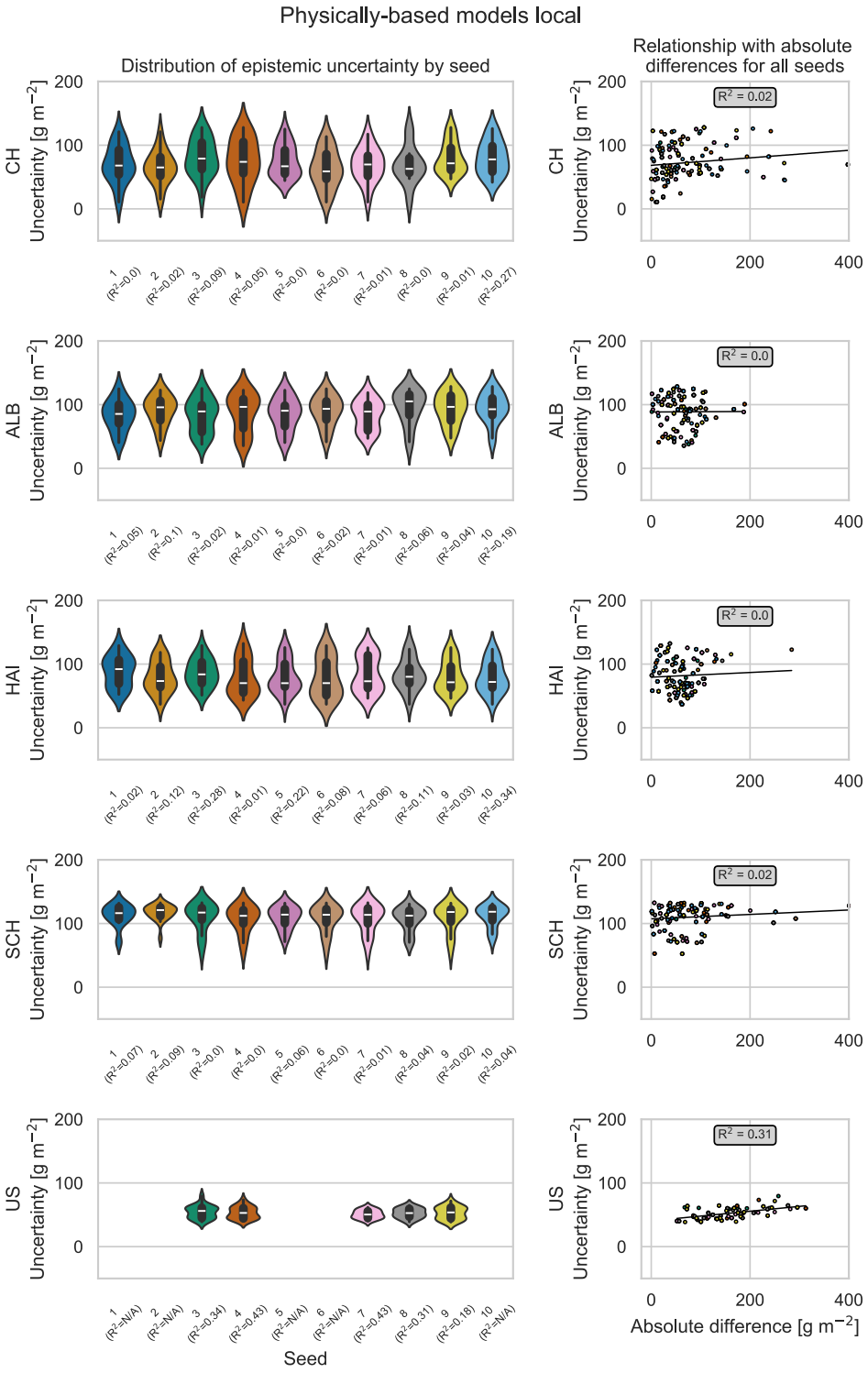

Figure A.4: Epistemic uncertainty of local physically-based models. Absolute differences correspond to the absolute difference between measured and predicted biomass value. If the percentage of solutions was equal to 0.01% (e.g., only 1 sample), no standard deviation and R^2 could be calculated. The corresponding predictions were omitted for the calculation of the overall R^2 showed in the textbox in the right column. CH: Switzerland, ALB: Schwäbische Alb, HAI: Hainich-Dün, SCH: Schorfheide-Chorin, US: United States.

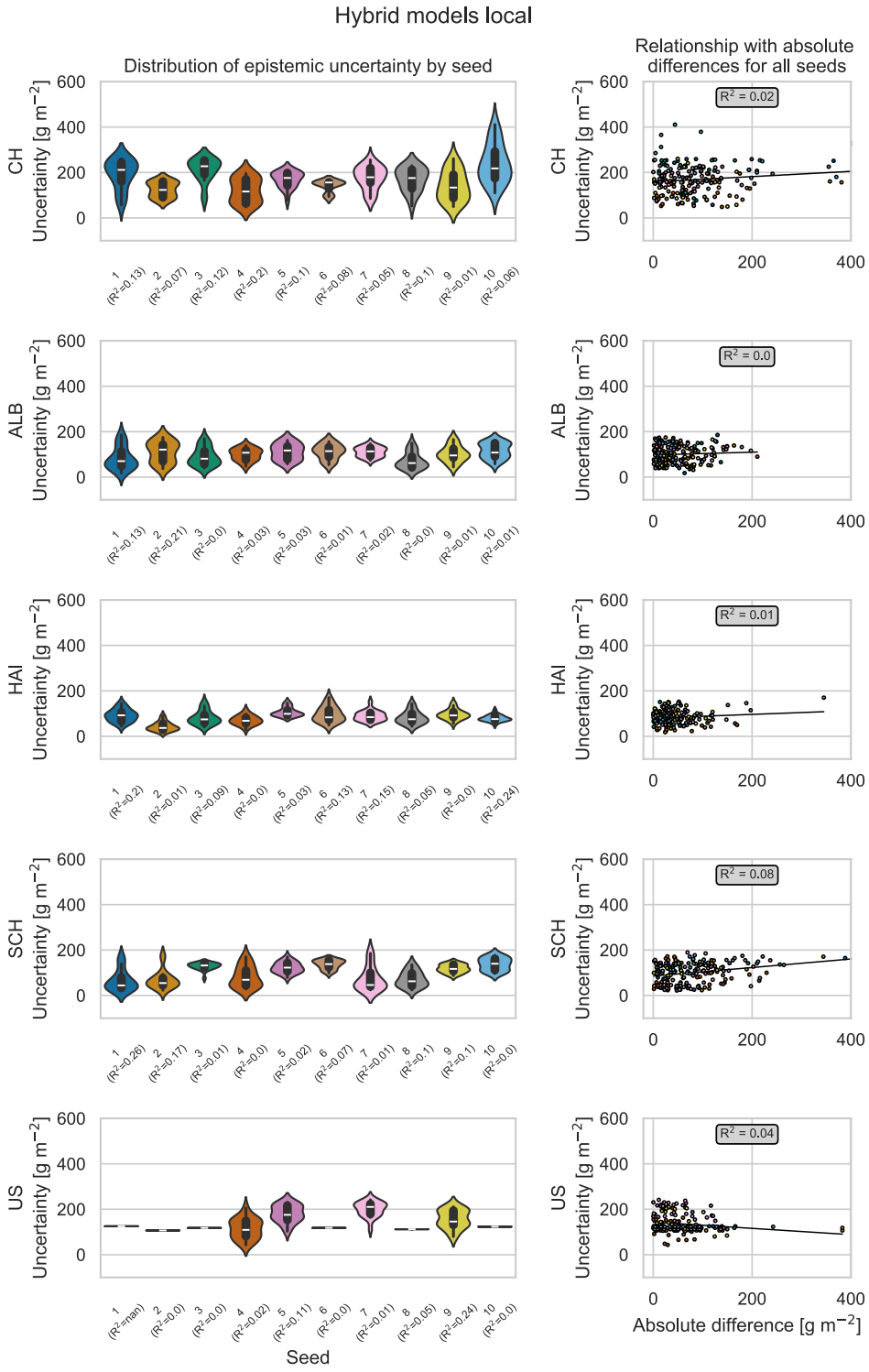

Figure A.5: Epistemic uncertainty of local hybrid models. Absolute differences correspond to the absolute difference between measured and predicted biomass value. In case a model predicted a straight line (e.g., the prediction is constant), the calculation of the coefficient of determination (R^2) was not possible. The corresponding predictions were omitted for the calculation of the overall R^2 showed in the textbox in the right column. CH: Switzerland, ALB: Schwäbische Alb, HAI: Hainich-Dün, SCH: Schorfheide-Chorin, US: United States.

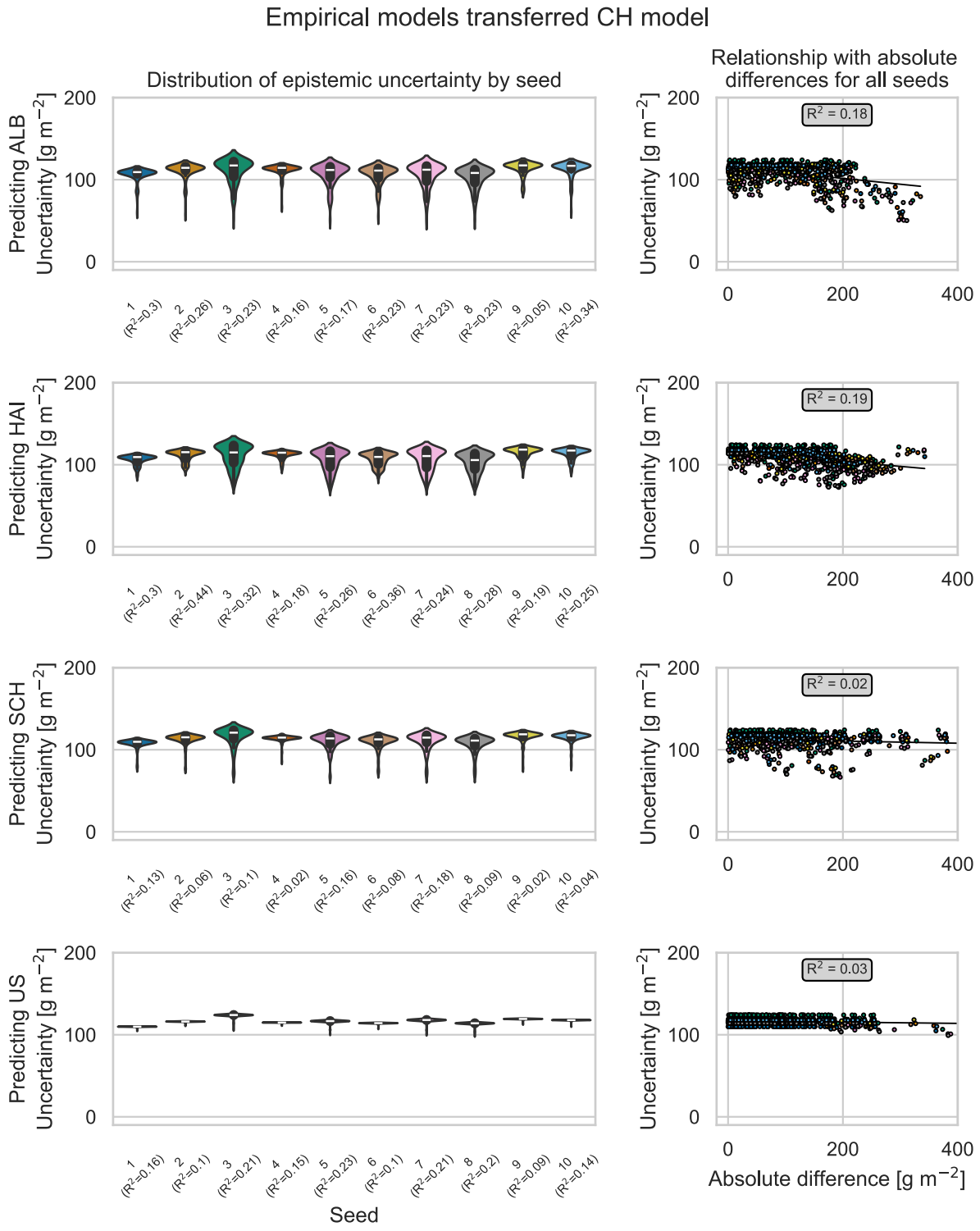

Figure A.6: Epistemic uncertainty of transferred empirical Gaussian process regression models for the CH site. Absolute differences correspond to the absolute difference between measured and predicted biomass value. In case a model predicted a straight line (e.g., the prediction is constant), the calculation of the coefficient of determination (R^2) was not possible. The corresponding predictions were omitted for the calculation of the overall R^2 showed in the textbox in the right column. CH: Switzerland, ALB: Schwäbische Alb, HAI: Hainich-Dün, SCH: Schorfheide-Chorin, US: United States.

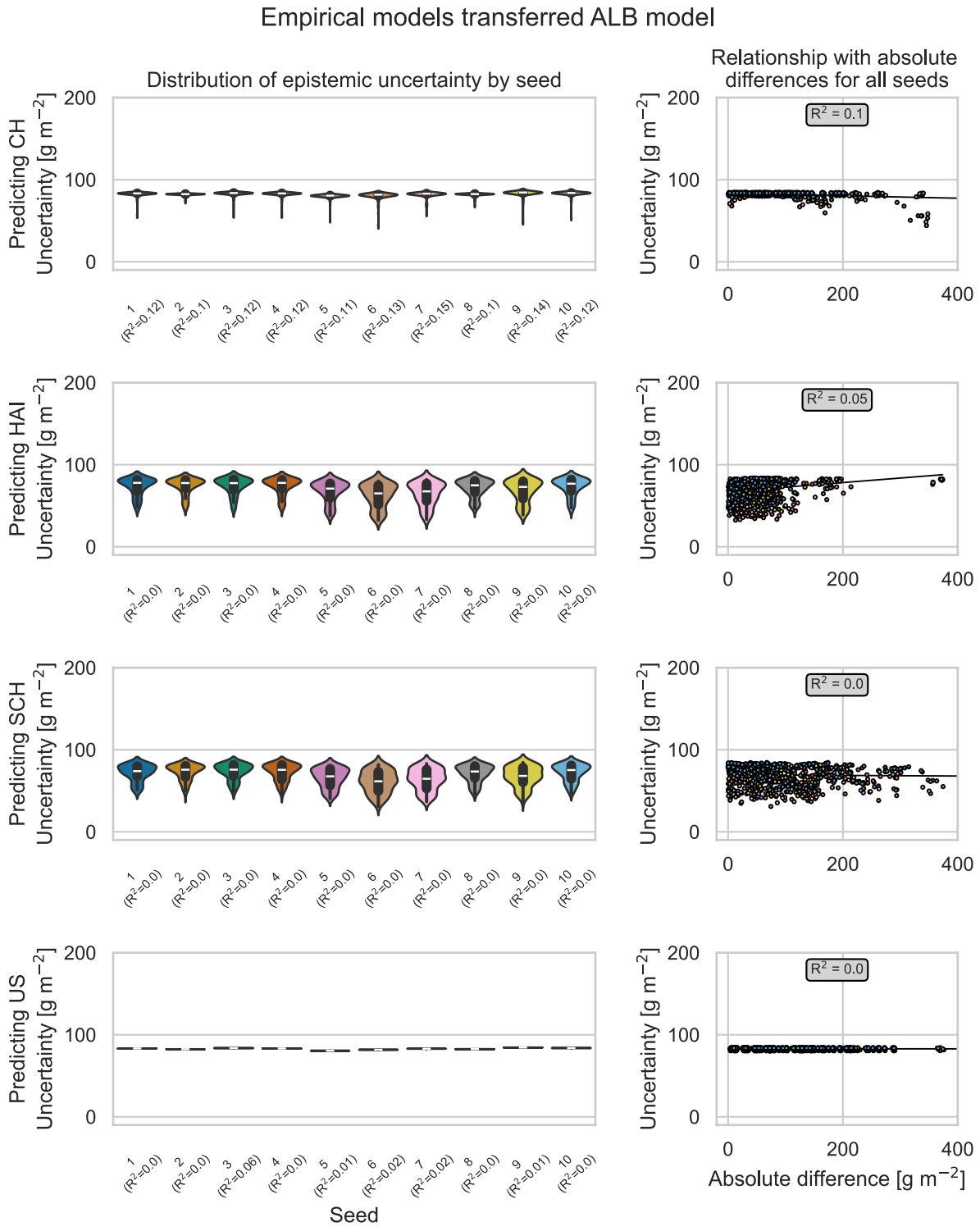

Figure A.7: Epistemic uncertainty of transferred empirical Gaussian process regression models for the ALB site. Absolute differences correspond to the absolute difference between measured and predicted biomass value. In case a model predicted a straight line (e.g., the prediction is constant), the calculation of the coefficient of determination (R^2) was not possible. The corresponding predictions were omitted for the calculation of the overall R^2 showed in the textbox in the right column. CH: Switzerland, ALB: Schwäbische Alb, HAI: Hainich-Dün, SCH: Schorfheide-Chorin, US: United States.

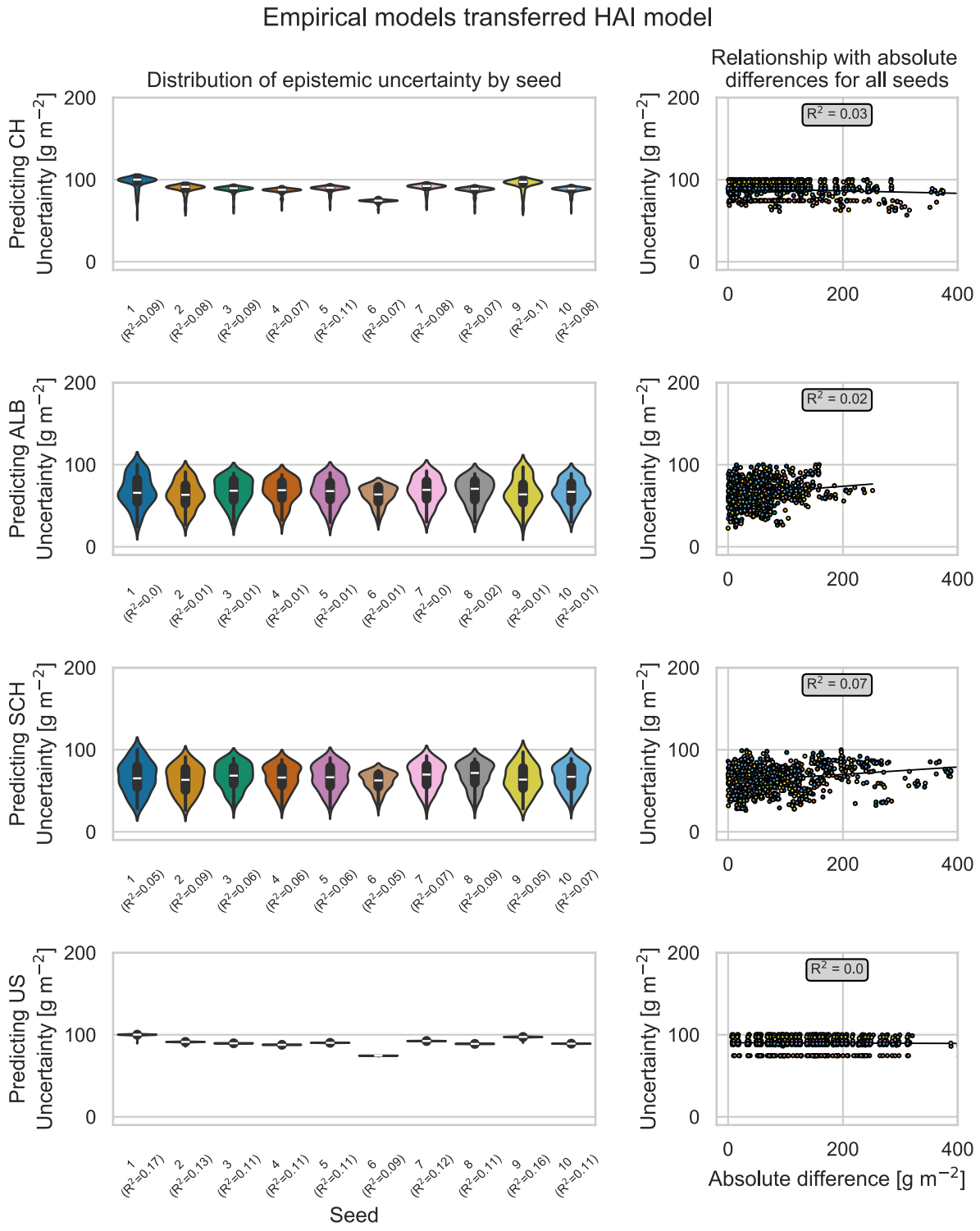

Figure A.8: Epistemic uncertainty of transferred empirical Gaussian process regression models for the HAI site. Absolute differences correspond to the absolute difference between measured and predicted biomass value. In case a model predicted a straight line (e.g., the prediction is constant), the calculation of the coefficient of determination (R^2) was not possible. The corresponding predictions were omitted for the calculation of the overall R^2 showed in the textbox in the right column. CH: Switzerland, ALB: Schwäbische Alb, HAI: Hainich-Dün, SCH: Schorfheide-Chorin, US: United States.

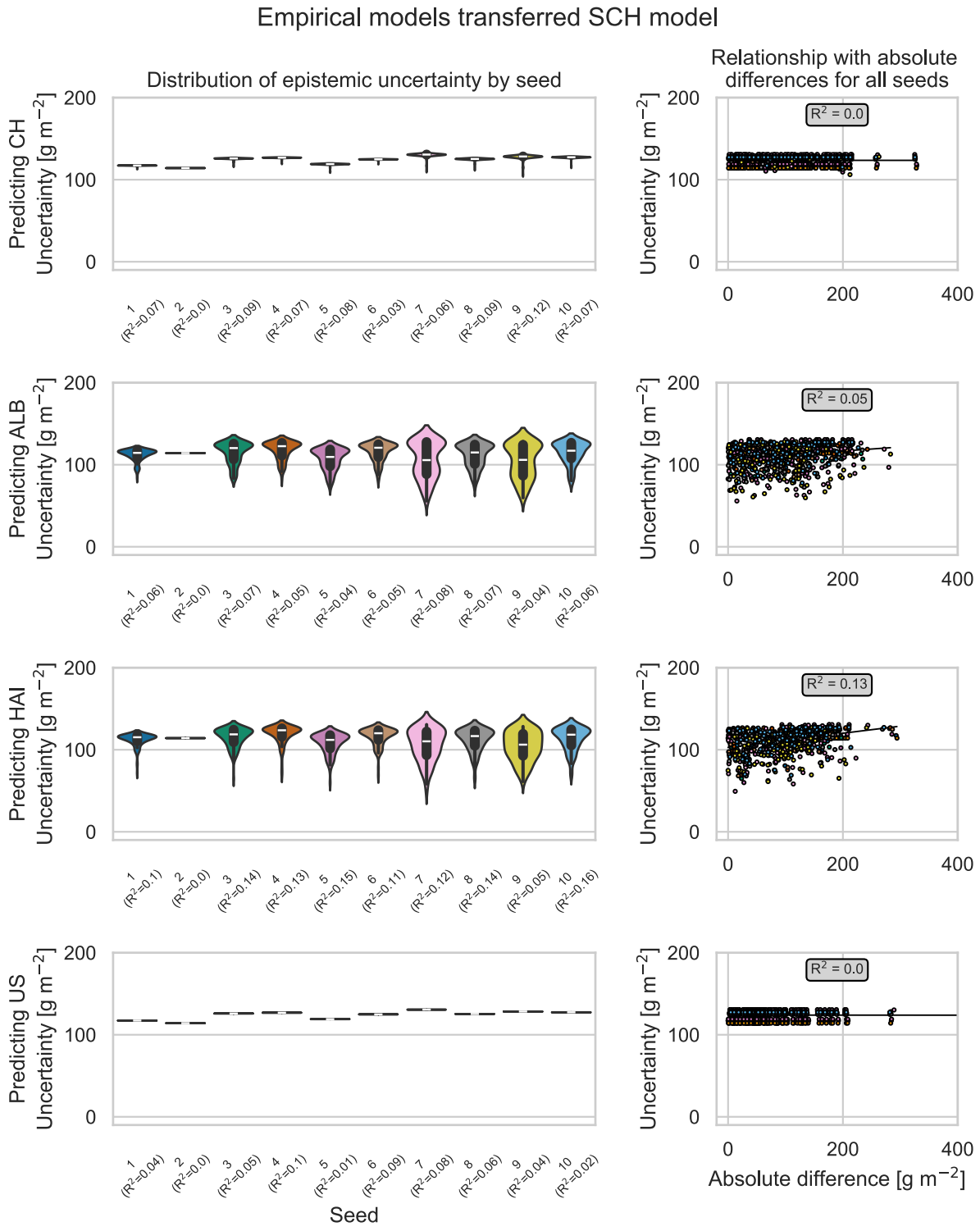

Figure A.9: Epistemic uncertainty of transferred empirical Gaussian process regression models for the SCH site. Absolute differences correspond to the absolute difference between measured and predicted biomass value. In case a model predicted a straight line (e.g., the prediction is constant), the calculation of the coefficient of determination (R^2) was not possible. The corresponding predictions were omitted for the calculation of the overall R^2 showed in the textbox in the right column. CH: Switzerland, ALB: Schwäbische Alb, HAI: Hainich-Dün, SCH: Schorfheide-Chorin, US: United States.

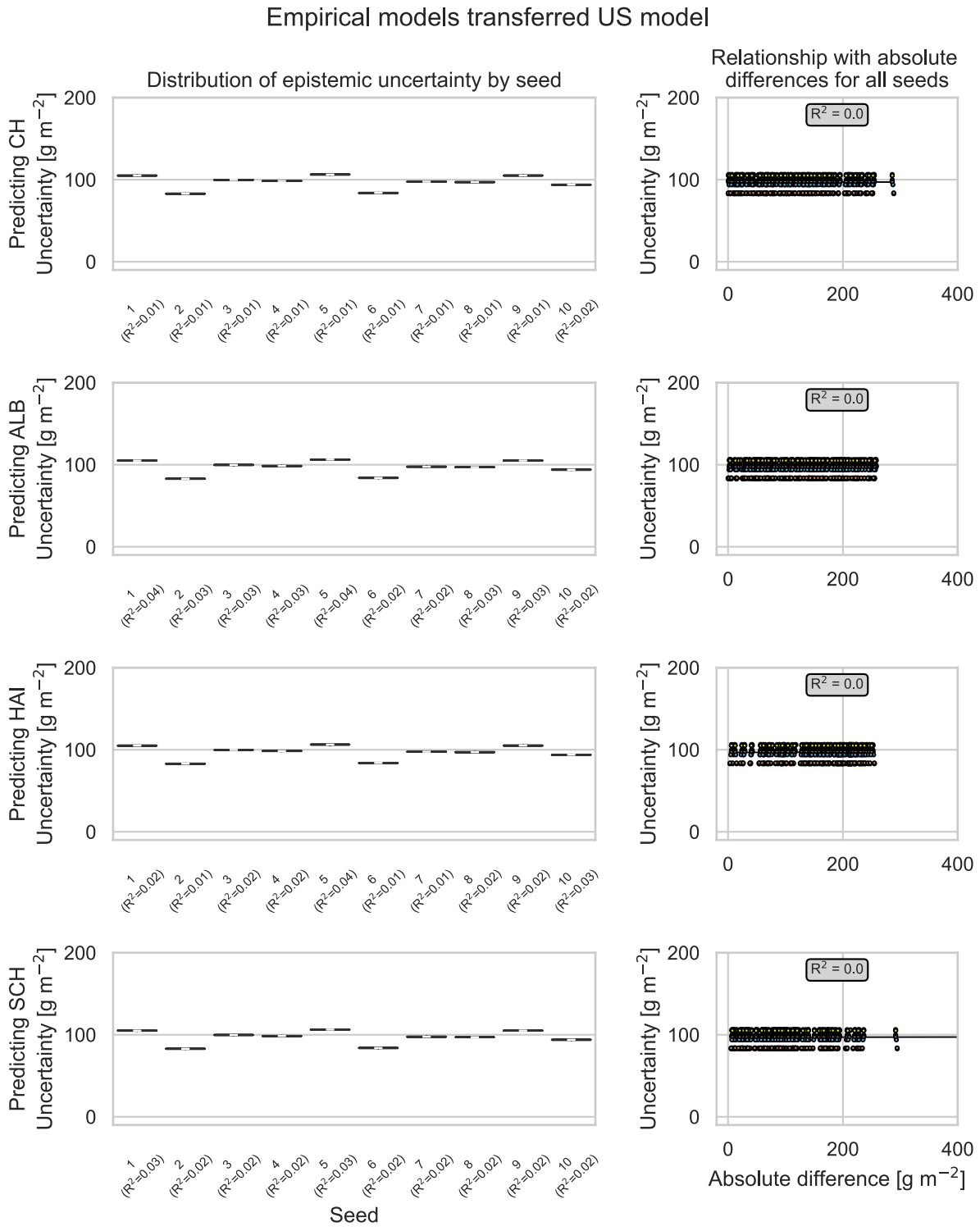

Figure A.10: Epistemic uncertainty of transferred empirical Gaussian process regression models for the US site. Absolute differences correspond to the absolute difference between measured and predicted biomass value. In case a model predicted a straight line (e.g., the prediction is constant), the calculation of the coefficient of determination (R^2) was not possible. The corresponding predictions were omitted for the calculation of the overall R^2 showed in the textbox in the right column. CH: Switzerland, ALB: Schwäbische Alb, HAI: Hainich-Dün, SCH: Schorfheide-Chorin, US: United States.

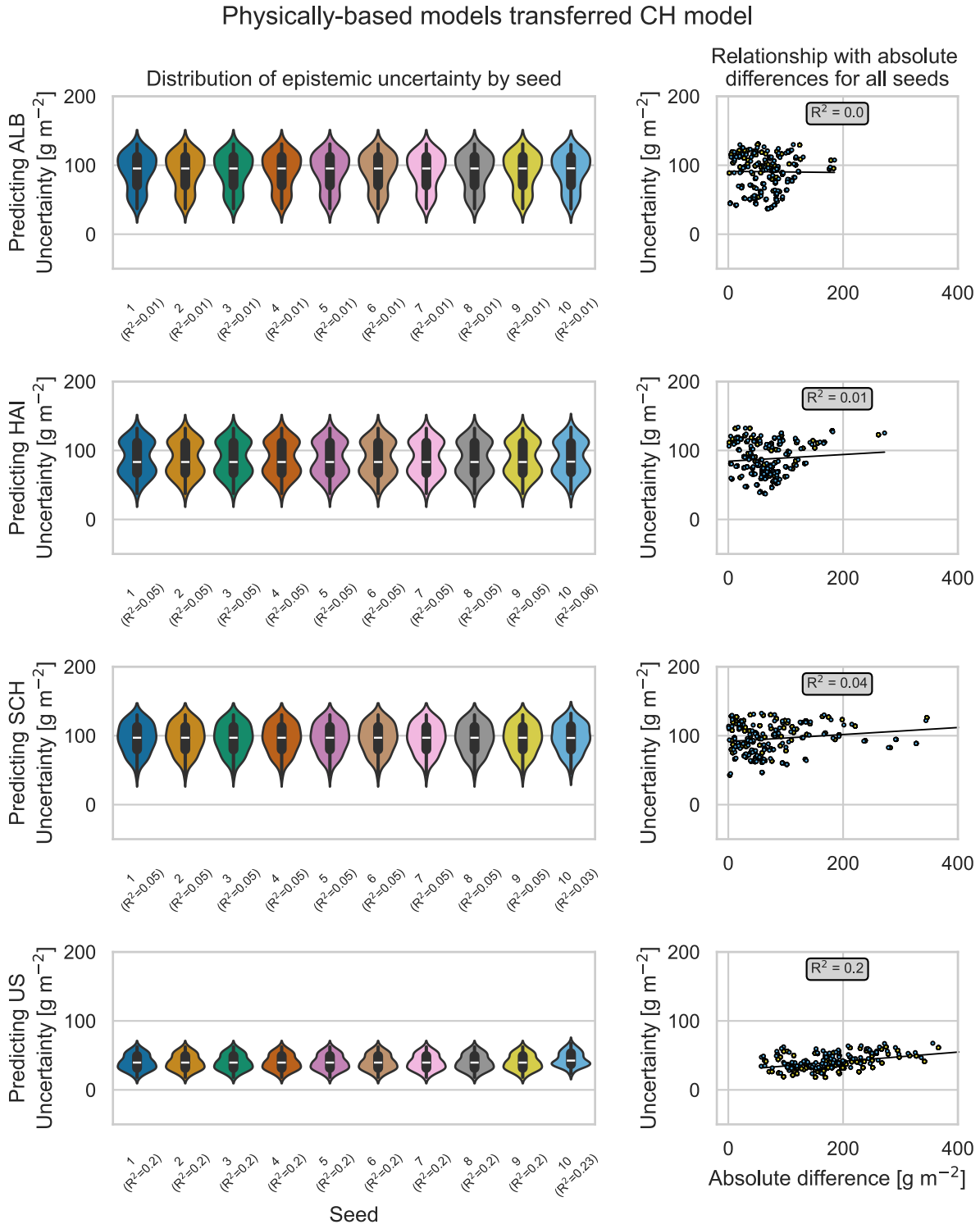

Figure A.11: Epistemic uncertainty of transferred physically-based models for the CH site. Absolute differences correspond to the absolute difference between measured and predicted biomass value. If the percentage of solutions was equal to 0.01% (e.g., only 1 sample), no standard deviation and R^2 could be calculated. The corresponding predictions were omitted for the calculation of the overall R^2 showed in the textbox in the right column. CH: Switzerland, ALB: Schwäbische Alb, HAI: Hainich-Dün, SCH: Schorfheide-Chorin, US: United States.

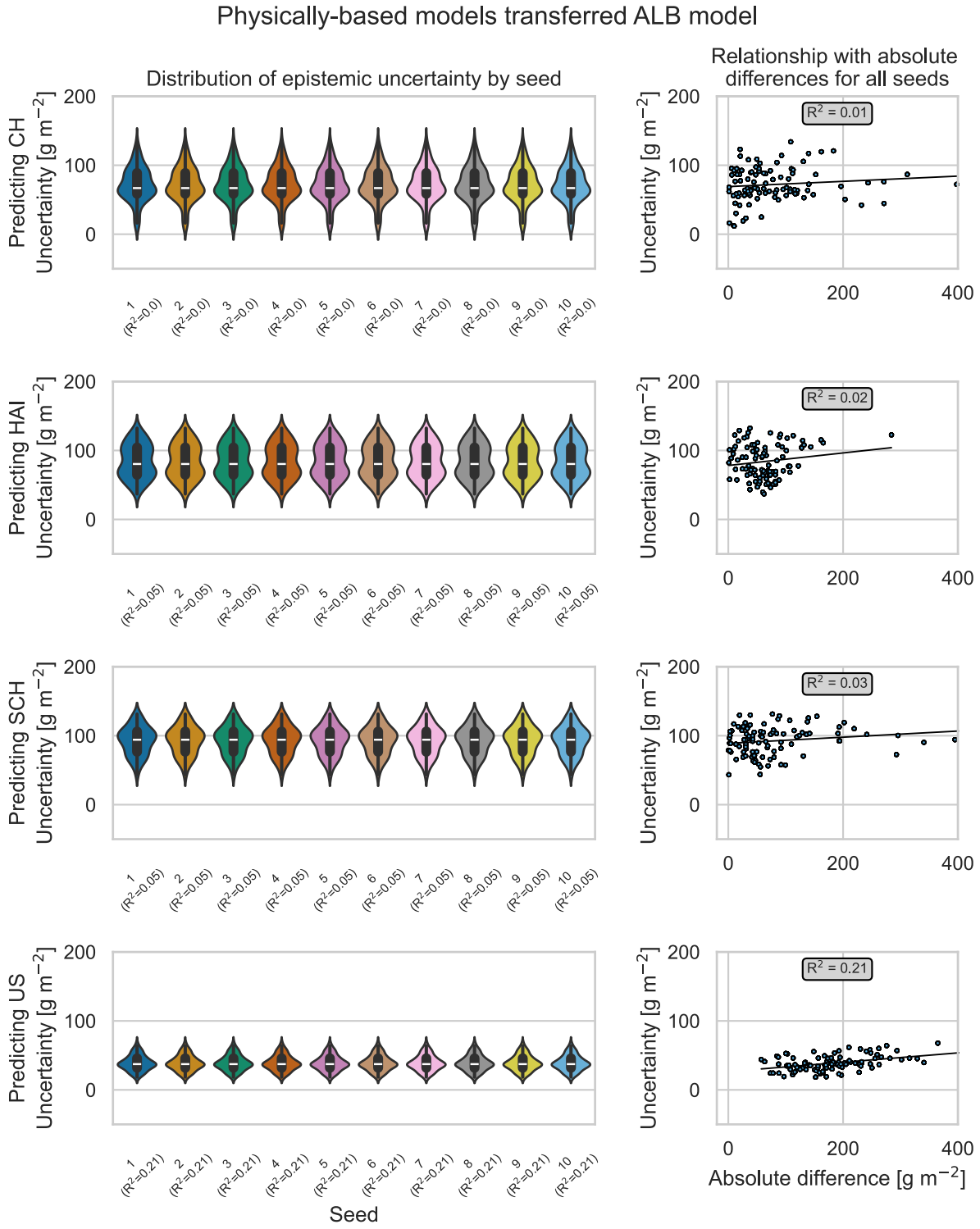

Figure A.12: Epistemic uncertainty of transferred physically-based models for the ALB site. Absolute differences correspond to the absolute difference between measured and predicted biomass value. If the percentage of solutions was equal to 0.01% (e.g., only 1 sample), no standard deviation and R^2 could be calculated. The corresponding predictions were omitted for the calculation of the overall R^2 showed in the textbox in the right column. CH: Switzerland, ALB: Schwäbische Alb, HAI: Hainich-Dün, SCH: Schorfheide-Chorin, US: United States.

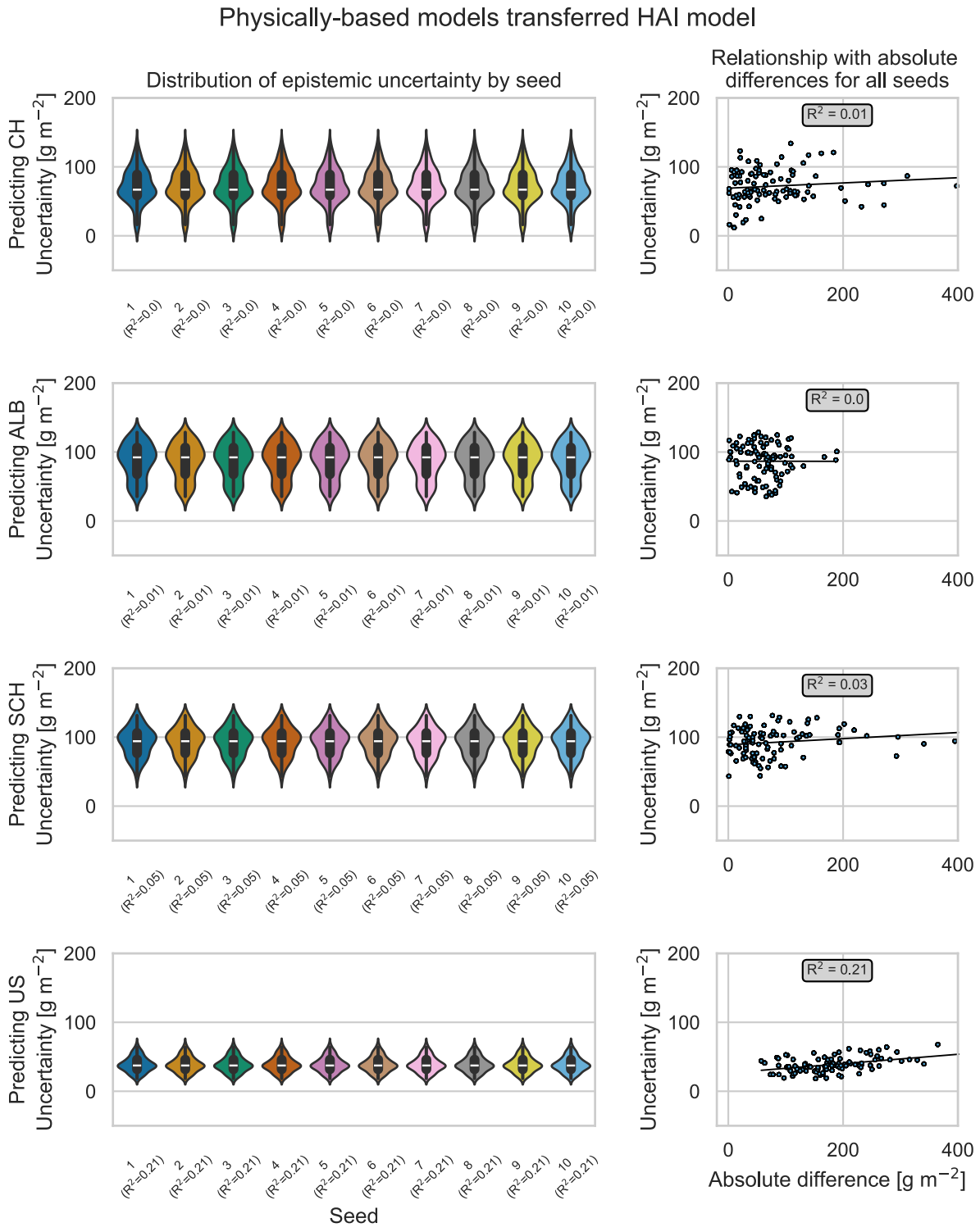

Figure A.13: Epistemic uncertainty of transferred physically-based models for the HAI site. Absolute differences correspond to the absolute difference between measured and predicted biomass value. If the percentage of solutions was equal to 0.01% (e.g., only 1 sample), no standard deviation and R^2 could be calculated. The corresponding predictions were omitted for the calculation of the overall R^2 showed in the textbox in the right column. CH: Switzerland, ALB: Schwäbische Alb, HAI: Hainich-Dün, SCH: Schorfheide-Chorin, US: United States.

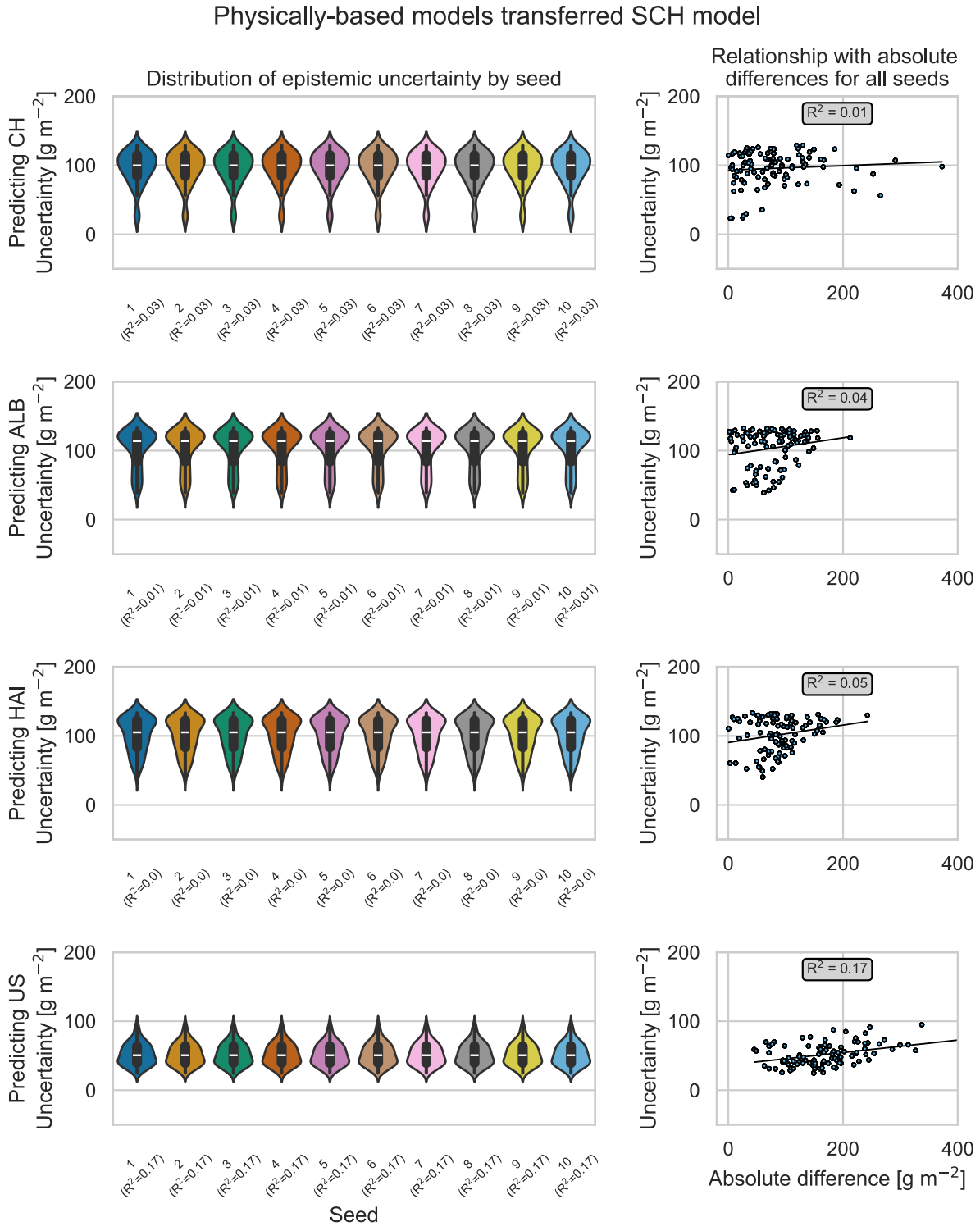

Figure A.14: Epistemic uncertainty of transferred physically-based models for the SCH site. Absolute differences correspond to the absolute difference between measured and predicted biomass value. If the percentage of solutions was equal to 0.01% (e.g., only 1 sample), no standard deviation and R^2 could be calculated. The corresponding predictions were omitted for the calculation of the overall R^2 showed in the textbox in the right column. CH: Switzerland, ALB: Schwäbische Alb, HAI: Hainich-Dün, SCH: Schorfheide-Chorin, US: United States.

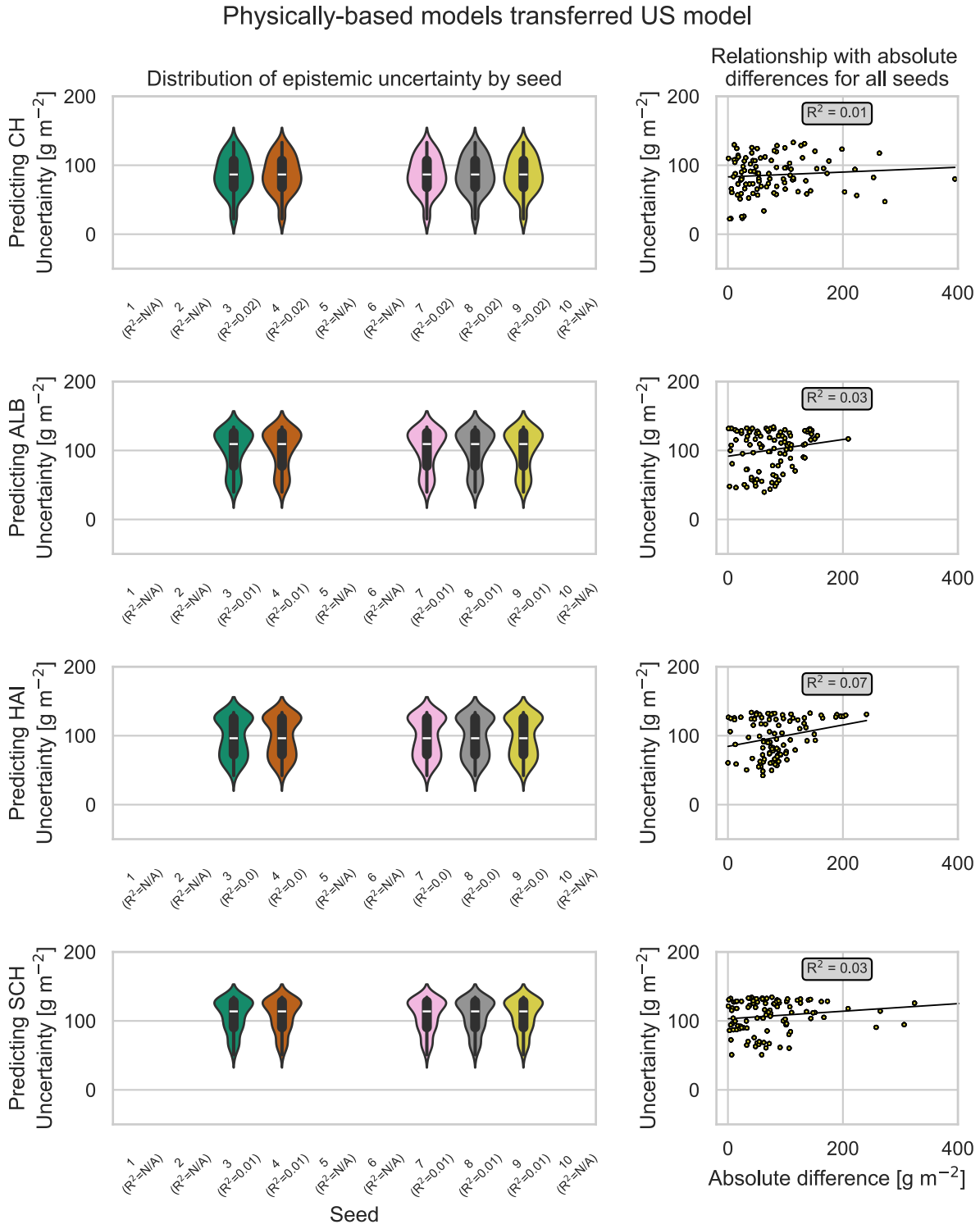

Figure A.15: Epistemic uncertainty of transferred physically-based models for the US site. Absolute differences correspond to the absolute difference between measured and predicted biomass value. If the percentage of solutions was equal to 0.01% (e.g., only 1 sample), no standard deviation and R^2 could be calculated. The corresponding predictions were omitted for the calculation of the overall R^2 showed in the textbox in the right column. CH: Switzerland, ALB: Schwäbische Alb, HAI: Hainich-Dün, SCH: Schorfheide-Chorin, US: United States.

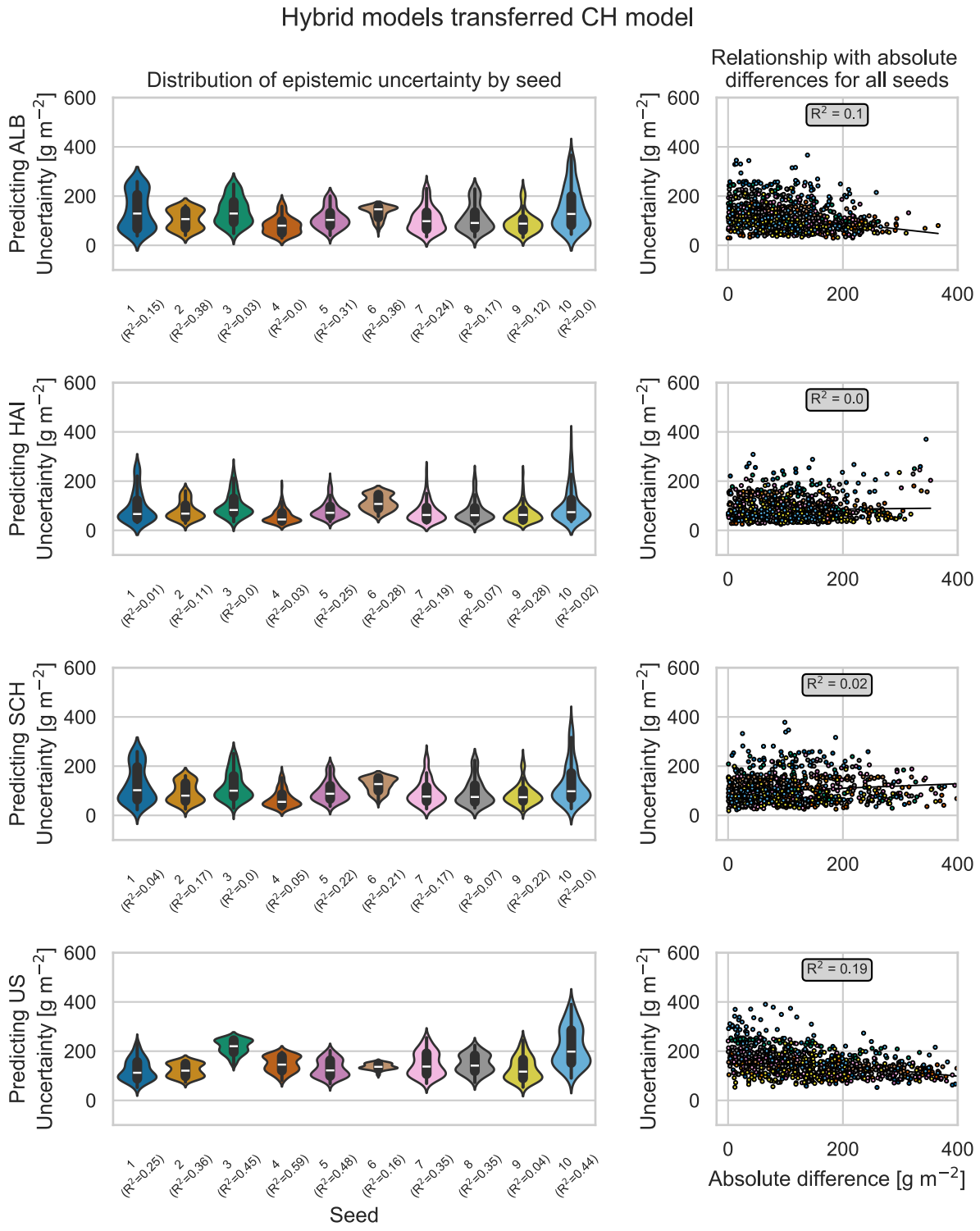

Figure A.16: Epistemic uncertainty of transferred hybrid models for the CH site. Absolute differences correspond to the absolute difference between measured and predicted biomass value. In case a model predicted a straight line (e.g., the prediction is constant), the calculation of the coefficient of determination (R^2) was not possible. The corresponding predictions were omitted for the calculation of the overall R^2 showed in the textbox in the right column. CH: Switzerland, ALB: Schwäbische Alb, HAI: Hainich-Dün, SCH: Schorfheide-Chorin, US: United States.

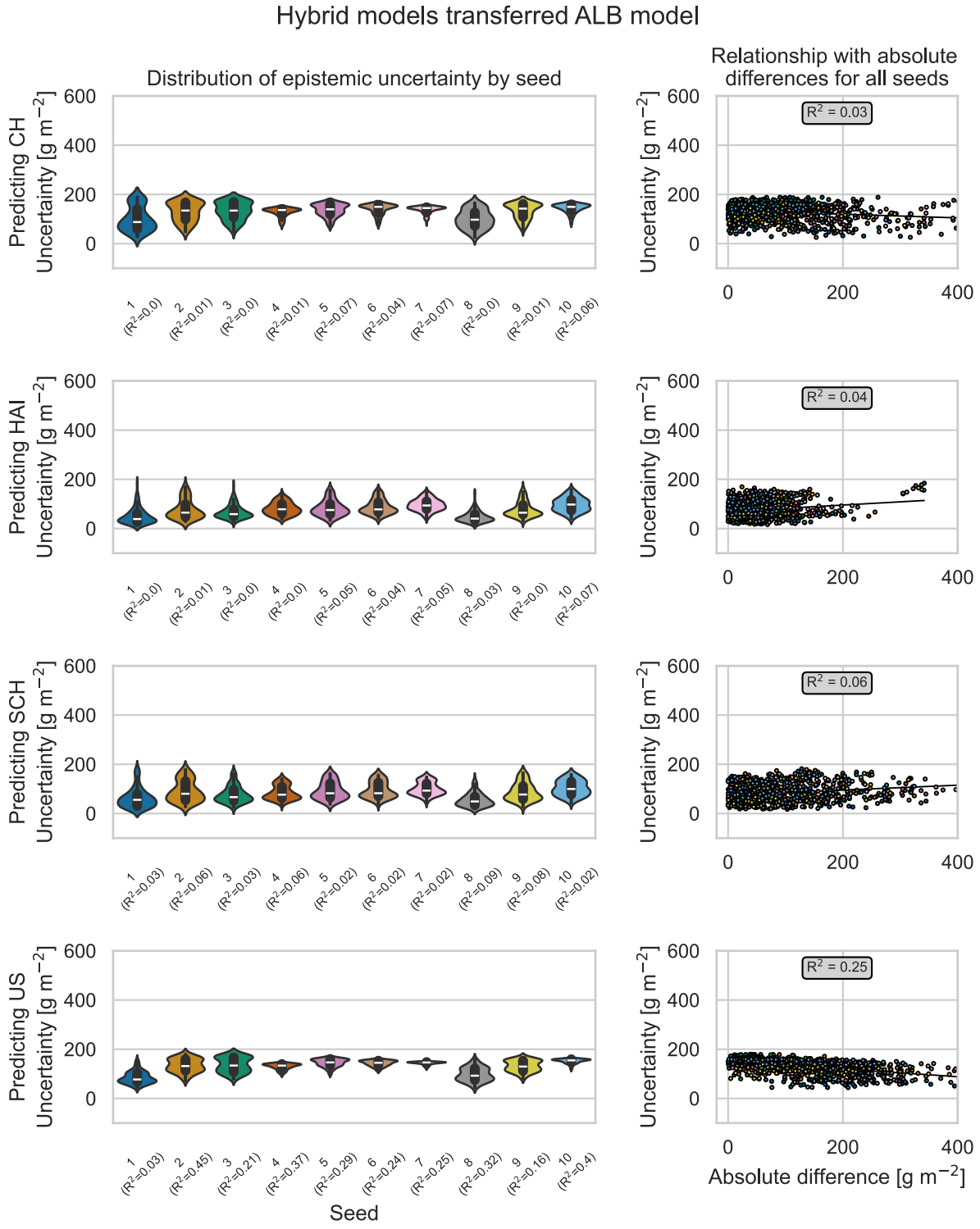

Figure A.17: Epistemic uncertainty of transferred hybrid models for the ALB site. Absolute differences correspond to the absolute difference between measured and predicted biomass value. In case a model predicted a straight line (e.g., the prediction is constant), the calculation of the coefficient of determination (R^2) was not possible. The corresponding predictions were omitted for the calculation of the overall R^2 showed in the textbox in the right column. CH: Switzerland, ALB: Schwäbische Alb, HAI: Hainich-Dün, SCH: Schorfheide-Chorin, US: United States.

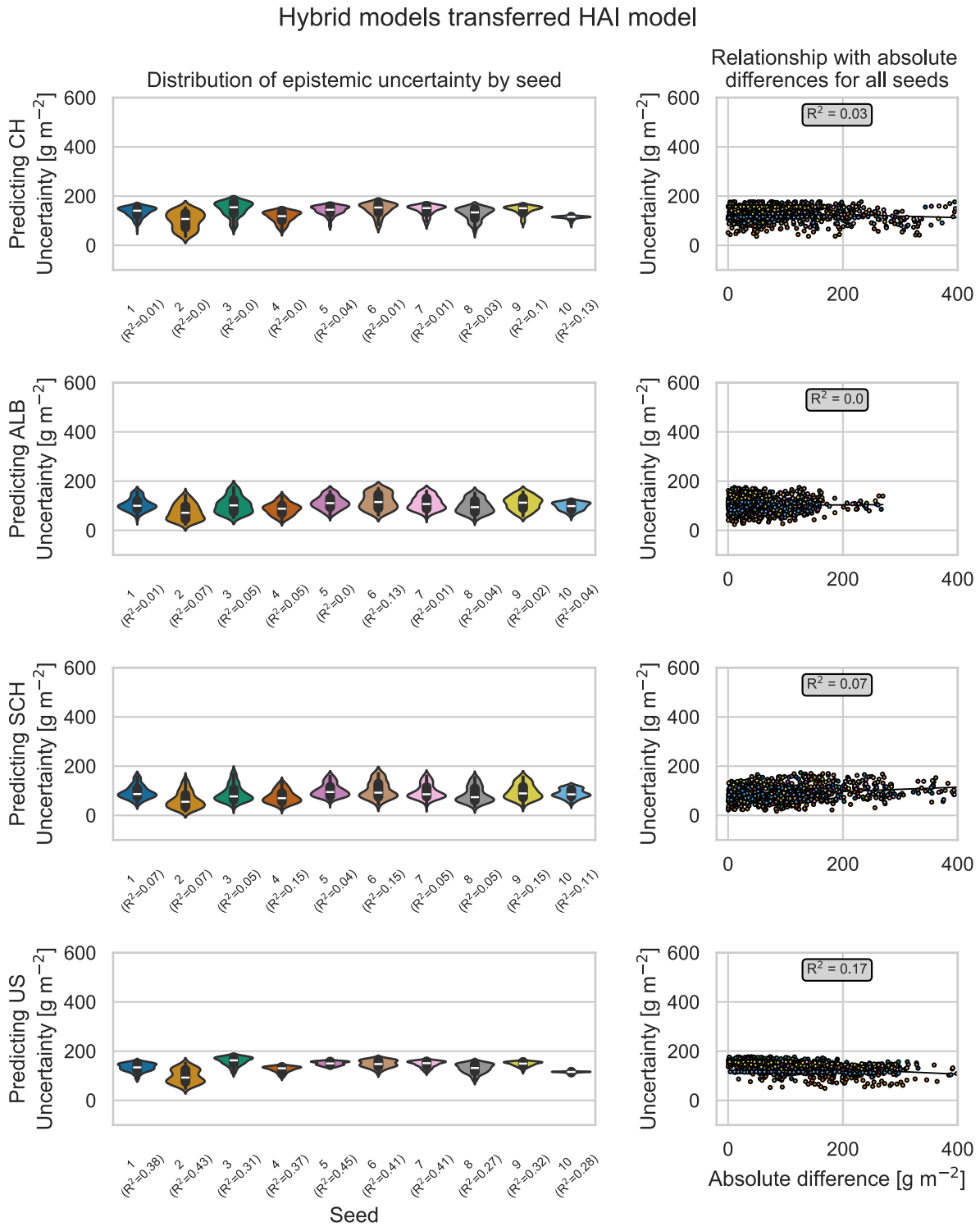

Figure A.18: Epistemic uncertainty of transferred hybrid models for the HAI site. Absolute differences correspond to the absolute difference between measured and predicted biomass value. In case a model predicted a straight line (e.g., the prediction is constant), the calculation of the coefficient of determination (R^2) was not possible. The corresponding predictions were omitted for the calculation of the overall R^2 showed in the textbox in the right column. CH: Switzerland, ALB: Schwäbische Alb, HAI: Hainich-Dün, SCH: Schorfheide-Chorin, US: United States.

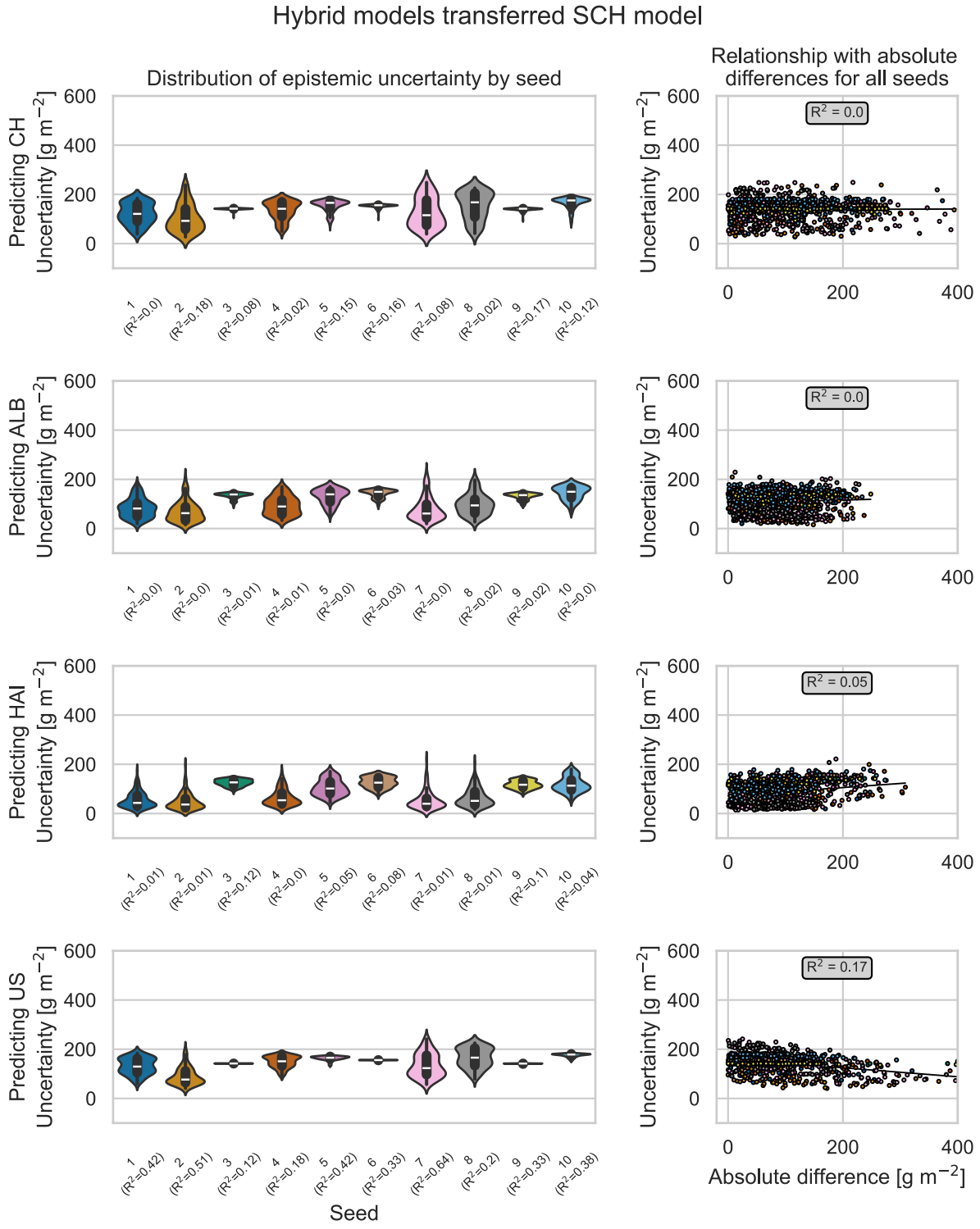

Figure A.19: Epistemic uncertainty of transferred hybrid models for the SCH site. Absolute differences correspond to the absolute difference between measured and predicted biomass value. In case a model predicted a straight line (e.g., the prediction is constant), the calculation of the coefficient of determination (R^2) was not possible. The corresponding predictions were omitted for the calculation of the overall R^2 showed in the textbox in the right column. CH: Switzerland, ALB: Schwäbische Alb, HAI: Hainich-Dün, SCH: Schorfheide-Chorin, US: United States.

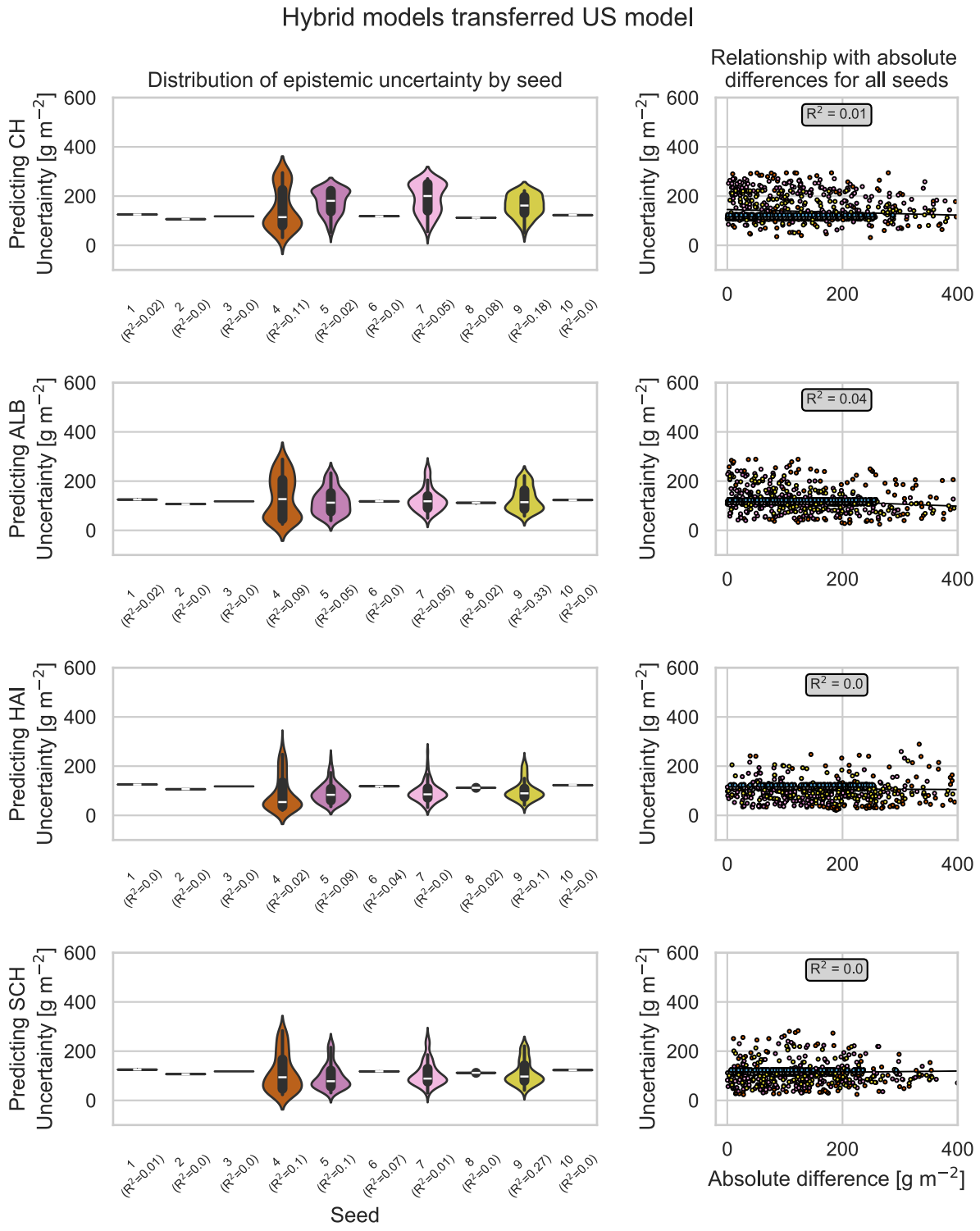

Figure A.20: Epistemic uncertainty of transferred hybrid models for the US site. Absolute differences correspond to the absolute difference between measured and predicted biomass value. In case a model predicted a straight line (e.g., the prediction is constant), the calculation of the coefficient of determination (R^2) was not possible. The corresponding predictions were omitted for the calculation of the overall R^2 showed in the textbox in the right column. CH: Switzerland, ALB: Schwäbische Alb, HAI: Hainich-Dün, SCH: Schorfheide-Chorin, US: United States.

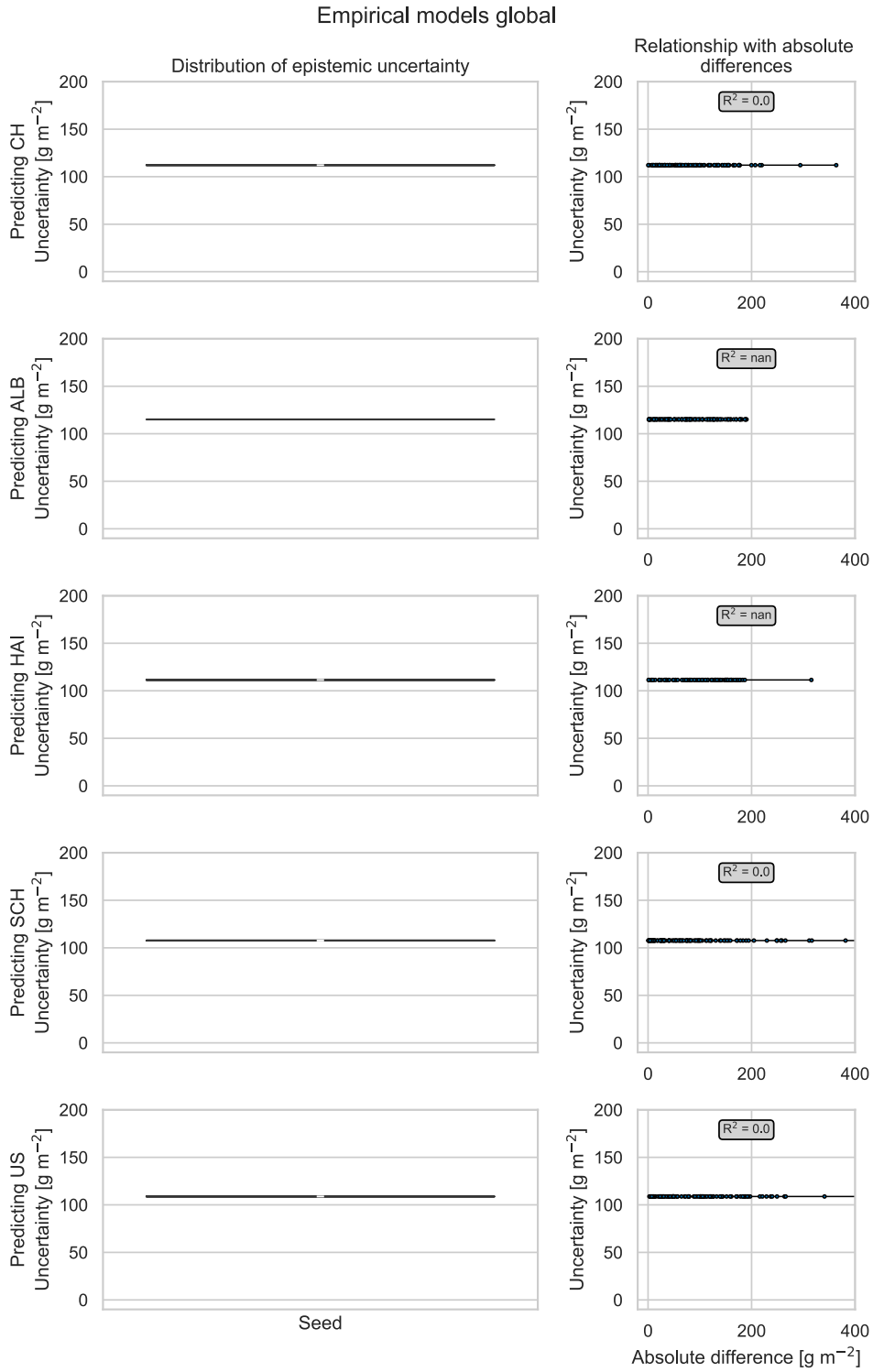

Figure A.21: Epistemic uncertainty of global empirical models. Absolute differences correspond to the absolute difference between measured and predicted biomass value. In case a model predicted a straight line (e.g., the prediction is constant), the calculation of the coefficient of determination (R^2) was not possible. The corresponding predictions were omitted for the calculation of the overall R^2 showed in the textbox in the right column. CH: Switzerland, ALB: Schwäbische Alb, HAI: Hainich-Dün, SCH: Schorfheide-Chorin, US: United States.

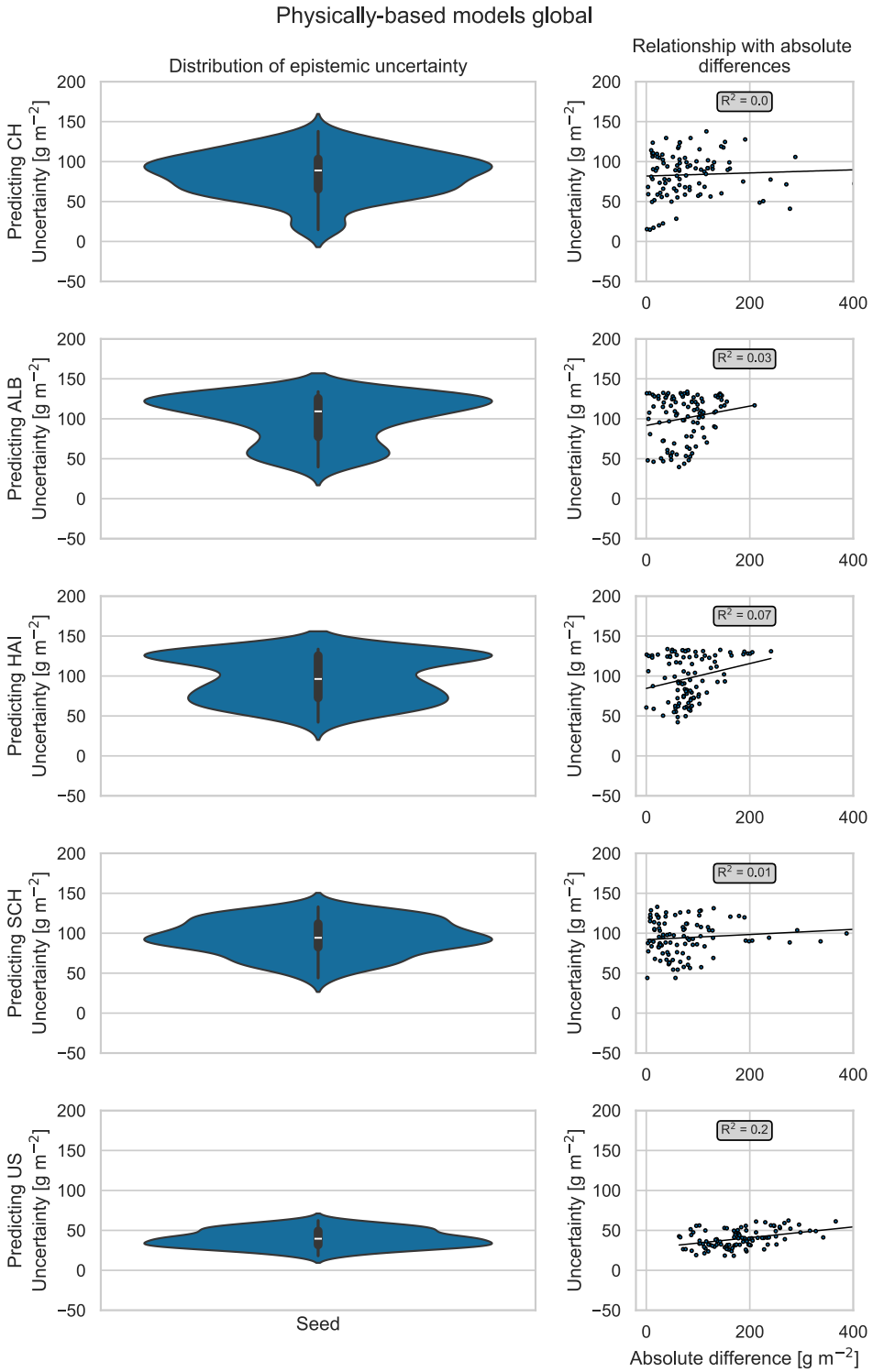

Figure A.22: Epistemic uncertainty of global physically-based models. Absolute differences correspond to the absolute difference between measured and predicted biomass value. If the percentage of solutions was equal to 0.01% (e.g., only 1 sample), no standard deviation and R^2 could be calculated. The corresponding predictions were omitted for the calculation of the overall R^2 showed in the textbox in the right column. CH: Switzerland, ALB: Schwäbische Alb, HAI: Hainich-Dün, SCH: Schorfheide-Chorin, US: United States.

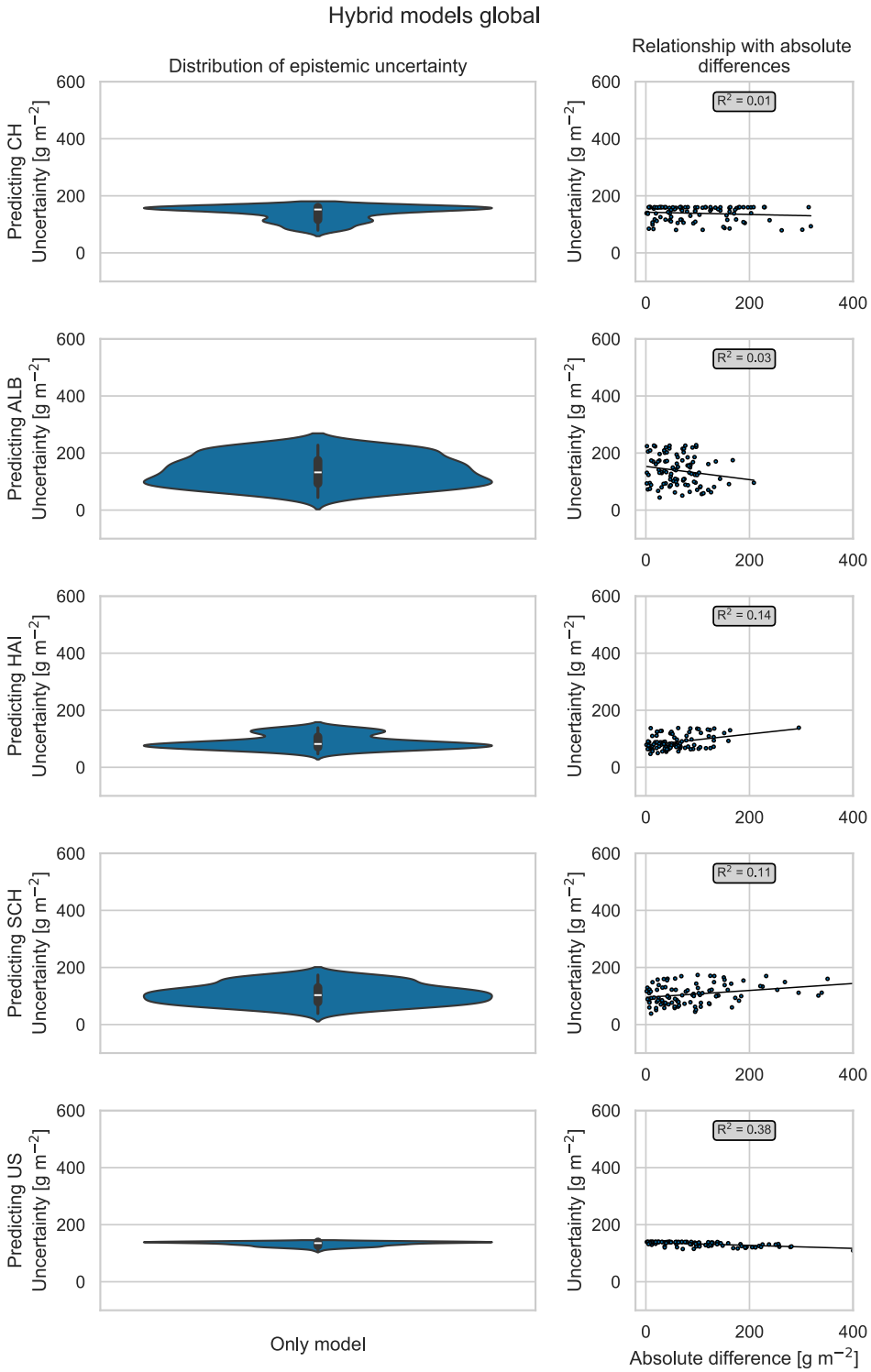

Figure A.23: Epistemic uncertainty of global hybrid models. Absolute differences correspond to the absolute difference between measured and predicted biomass value. In case a model predicted a straight line (e.g., the prediction is constant), the calculation of the coefficient of determination (R^2) was not possible. The corresponding predictions were omitted for the calculation of the overall R^2 showed in the textbox in the right column. CH: Switzerland, ALB: Schwäbische Alb, HAI: Hainich-Dün, SCH: Schorfheide-Chorin, US: United States.

Section A.18: Biomass and spectral variability by site

Table A.14: Properties of biomass (range and coefficient of variation (CV), calculated by dividing the variance by the mean) and the spectral bands (CV) by site, and mean relative root-mean-square error (RRMSE) and coefficient of determination (R^2) of best local empirical, physically-based, and hybrid models. For the empirical models, only the best-performing model in terms of lowest RRMSE is shown with the model specified in brackets. A missing R^2 indicates that its calculation was not possible due to predictions of constant values (=horizontal line). CH: Switzerland, ALB: Schwäbische Alb, HAI: Hainich-Dün, SCH: Schorfheide-Chorin, US: United States, RFR: Random Forest regression, SVR: Support Vector regression, XGB: Extreme Gradient Boosting regression, GPR: Gaussian Process regression.

Property	**Site**				
	CH	**ALB**	**HAI**	**SCH**	**US**
Biomass range [g m^{-2}]	540.49	379.00	502.37	643.00	518.60
Biomass CV [g m^{-2}]	70.73	52.40	64.18	64.78	28.41
490 nm band CV * 100	0.94	0.37	0.36	0.24	0.49
560 nm band CV * 100	0.56	0.20	0.18	0.15	0.08
665 nm band CV * 100	1.25	1.02	0.75	0.57	0.09
705 nm band CV * 100	0.60	0.40	0.34	0.24	0.23
740 nm band CV * 100	1.72	0.71	0.57	0.56	0.19
783 nm band CV * 100	2.15	1.24	1.03	1.01	0.26
842 nm band CV * 100	2.06	1.23	1.05	0.90	0.27
865 nm band CV * 100	2.14	1.09	0.92	0.89	0.27
1610 nm band CV * 100	0.98	1.00	0.78	0.65	0.37
2190 nm band CV * 100	0.99	1.09	0.84	0.61	0.46
Mean CV of all bands * 100	1.34	0.84	0.68	0.58	0.27
Mean RRMSE of best local empirical models	0.55 (SVR)	0.43 (SVR)	0.44 (RFR)	0.42 (SVR)	0.22 (SVR)
Mean R^2 of best local empirical models	0.31 (SVR)	0.54 (SVR)	0.64 (RFR)	0.42 (SVR)	0.59 (SVR)
Mean RRMSE of best local physically-based models	0.59	0.52	0.59	0.47	0.71
Mean R^2 of best local physically-based models	0.26	0.43	0.66	0.30	0.30
Mean RRMSE of best local hybrid models	0.64	0.46	0.51	0.47	0.29
Mean R^2 of best local hybrid models	0.23	0.46	0.54	0.27	0.23

Section A.19: Performances of local physically-based models with US-tailored LUT

Table A.15: Value ranges and distributions of PROSAIL input parameters when adjusting the upper bound of LMA to the conditions of the study site in the United States.

Parameter	Variable	Unit	Minimum value	Maximum value	Distribution
Leaf structure parameter	N	[-]	1.5	1.9	uniform
Chlorophyll content	CHL	[µg cm^{-2}]	5	75	uniform
Carotenoid content	CAR	[µg cm^{-2}]	2	60	uniform
Anthocyanin content	ANT	[µg cm^{-2}]	0	2	uniform
Brown pigment content	BROWN	[-]	0	1	uniform
Equivalent water thickness	EWT	[cm]	0.001	0.04	uniform
Leaf mass per area	LMA	[g cm^{-2}]	0.002	0.03	uniform
Angle for incident light at leaf surface	alpha	[°]	40	40	fixed
Leaf inclination distribution function	TypeLidf	[-]	2	2	fixed
Average leaf angle	LIDFa	[°]	40	70	uniform
Leaf area index	LAI	[-]	0.1	4	uniform
Hot spot parameter	q	[-]	0.01	0.1	uniform
Sun zenith angle	tts	[°]	25	75	uniform
Observer zenith angle	tto	[°]	0	0	fixed
Relative azimuth angle	psi	[°]	50	180	uniform
Dry/wet soil factor	psoil	[-]	0	1	uniform

290 *Table A.16: Cost function, percentage of solutions, coefficient of determination (R^2), root-mean-square error (RMSE), and*
291 *relative root-mean-square error (RRMSE) of best performing local physically-based models with US-tailored look-up table*
292 *(LUT) and the LUT used in this study. The last columns show the difference for the three metrics.CH: Switzerland, ALB:*
293 *Schwäbische Alb, HAI: Hainich-Dün, SCH: Schorfheide-Chorin, US: United States.*

		US-tailored LUT					LUT used in this study					Difference		
Site	Seed	Cost function	Percentage of solutions	R^2	RMSE [g m^{-2}]	RRMSE	Cost function	Percentage of solutions	R^2	RMSE [g m^{-2}]	RRMSE	R^2	RMSE [g m^{-2}]	RRMSE
CH	1	min_contrast_1	10	0.146	183.977	1.069	min_contrast_1	1	0.221	95.683	0.556	-0.075	88.294	0.513
CH	2	min_contrast_1	10	0.129	192.067	1.111	min_contrast_1	1	0.214	96.421	0.558	-0.085	95.646	0.553
CH	3	min_contrast_1	10	0.089	182.882	1.047	min_contrast_1	1	0.149	107.756	0.617	-0.06	75.126	0.43
CH	4	min_contrast_1	10	0.104	187.059	1.077	min_contrast_1	1	0.142	104.529	0.602	-0.038	82.53	0.475
CH	5	min_contrast_1	10	0.152	176.047	1.014	min_contrast_1	1	0.207	102.279	0.589	-0.055	73.768	0.425
CH	6	min_contrast_1	10	0.12	189.101	1.095	min_contrast_1	1	0.211	96.402	0.558	-0.091	92.699	0.537
CH	7	min_contrast_1	10	0.138	187.292	1.079	min_contrast_1	1	0.208	101.18	0.583	-0.07	86.112	0.496
CH	8	min_contrast_1	10	0.123	189.073	1.096	min_contrast_1	1	0.192	98.848	0.573	-0.069	90.225	0.523
CH	9	min_contrast_1	10	0.15	183.183	1.05	min_contrast_1	1	0.23	101.751	0.583	-0.08	81.432	0.467
CH	10	min_contrast_1	10	0.168	185.039	1.063	min_contrast_2	1	0.263	97.142	0.558	-0.095	87.897	0.505
ALB	1	min_contrast_1	0.01	0.004	175.498	1.258	neyman_chi_square_divergence	1	0.419	72.6	0.521	-0.415	102.898	0.737
ALB	2	min_contrast_1	0.01	0	169.204	1.225	neyman_chi_square_divergence	1	0.392	70.695	0.512	-0.392	98.509	0.713
ALB	3	min_contrast_1	0.01	-0.001	174.703	1.247	neyman_chi_square_divergence	1	0.401	73.617	0.525	-0.402	101.086	0.722
ALB	4	min_contrast_1	0.01	0	179.925	1.303	neyman_chi_square_divergence	1	0.399	71.542	0.518	-0.399	108.383	0.785
ALB	5	min_contrast_4	0.01	-0.002	166.653	1.203	neyman_chi_square_divergence	1	0.491	67.975	0.491	-0.493	98.678	0.712
ALB	6	min_contrast_1	0.01	-0.001	178.391	1.283	neyman_chi_square_divergence	1	0.519	67.184	0.483	-0.52	111.207	0.8
ALB	7	min_contrast_1	0.01	0	183.314	1.325	neyman_chi_square_divergence	1	0.488	68.575	0.496	-0.488	114.739	0.829
ALB	8	min_contrast_1	0.01	-0.001	175.728	1.258	neyman_chi_square_divergence	1	0.404	71.385	0.511	-0.405	104.343	0.747
ALB	9	min_contrast_1	0.01	0.003	165.669	1.187	neyman_chi_square_divergence	1	0.424	70.498	0.505	-0.421	95.171	0.682
ALB	10	min_contrast_1	0.01	-0.003	168.671	1.209	neyman_chi_square_divergence	1	0.406	70.858	0.508	-0.409	97.813	0.701
HAI	1	min_contrast_4	1	0.248	201.964	1.73	neyman_chi_square_divergence	1	0.535	76.289	0.653	-0.287	125.675	1.077
HAI	2	min_contrast_4	1	0.221	203.59	1.747	neyman_chi_square_divergence	1	0.502	79.265	0.68	-0.281	124.325	1.067
HAI	3	min_contrast_4	1	0.255	197.651	1.707	neyman_chi_square_divergence	1	0.488	77.544	0.67	-0.233	120.107	1.037
HAI	4	min_contrast_4	1	0.262	206.588	1.777	neyman_chi_square_divergence	1	0.521	79.296	0.682	-0.259	127.292	1.095
HAI	5	min_contrast_3	1	0.258	204.656	1.757	neyman_chi_square_divergence	1	0.471	79.608	0.683	-0.213	125.048	1.074

HAI	6	min_contrast_4	1	0.29	209.137	1.831	neyman_chi_square_divergence	1	0.56	74.294	0.65	-0.27	134.843	1.181
HAI	7	min_contrast_3	1	0.242	202.982	1.75	neyman_chi_square_divergence	1	0.496	78.714	0.679	-0.254	124.268	1.071
HAI	8	min_contrast_4	1	0.279	199.78	1.718	neyman_chi_square_divergence	1	0.494	78.26	0.673	-0.215	121.52	1.045
HAI	9	min_contrast_4	1	0.215	205.101	1.748	neyman_chi_square_divergence	1	0.513	79.514	0.678	-0.298	125.587	1.07
HAI	10	min_contrast_2	1	0.205	206.158	1.773	neyman_chi_square_divergence	1	0.465	80.354	0.691	-0.26	125.804	1.082
SCH	1	neyman_chi_square_divergence	1	0.077	152.84	0.696	laplace_distribution	10	0.232	100.658	0.459	-0.155	52.182	0.237
SCH	2	neyman_chi_square_divergence	1	0.081	151.254	0.686	laplace_distribution	10	0.258	99.444	0.451	-0.177	51.81	0.235
SCH	3	neyman_chi_square_divergence	1	0.058	157.618	0.71	laplace_distribution	10	0.253	105.421	0.475	-0.195	52.197	0.235
SCH	4	neyman_chi_square_divergence	1	0.081	156.851	0.705	laplace_distribution	10	0.252	105.525	0.475	-0.171	51.326	0.23
SCH	5	neyman_chi_square_divergence	1	0.096	150.807	0.685	laplace_distribution	10	0.25	99.303	0.451	-0.154	51.504	0.234
SCH	6	neyman_chi_square_divergence	1	0.1	154.547	0.695	laplace_distribution	10	0.265	104.778	0.471	-0.165	49.769	0.224
SCH	7	neyman_chi_square_divergence	1	0.058	156.755	0.703	laplace_distribution	10	0.237	107.39	0.481	-0.179	49.365	0.222
SCH	8	neyman_chi_square_divergence	1	0.081	156.481	0.702	laplace_distribution	10	0.249	105.4	0.473	-0.168	51.081	0.229
SCH	9	neyman_chi_square_divergence	1	0.078	157.069	0.705	laplace_distribution	10	0.234	107.052	0.48	-0.156	50.017	0.225
SCH	10	neyman_chi_square_divergence	1	0.075	152.034	0.683	laplace_distribution	10	0.235	106.999	0.481	-0.16	45.035	0.202
US	1	min_contrast_4	10	0.446	90.501	0.345	pearson_chi_square	0.01	0.11	179.487	0.684	0.336	-88.986	-0.339
US	2	min_contrast_4	10	0.463	83.106	0.32	pearson_chi_square	0.01	0.102	173.848	0.67	0.361	-90.742	-0.35
US	3	min_contrast_4	10	0.424	93.415	0.356	min_contrast_4	10	0.411	182.307	0.695	0.013	-88.892	-0.339
US	4	min_contrast_4	10	0.408	93.22	0.355	min_contrast_4	10	0.394	182.016	0.694	0.014	-88.796	-0.339
US	5	min_contrast_4	10	0.46	93.352	0.356	pearson_chi_square	0.01	0.119	176.744	0.674	0.341	-83.392	-0.318
US	6	min_contrast_4	10	0.48	84.642	0.326	pearson_chi_square	0.01	0.101	174.832	0.673	0.379	-90.19	-0.347
US	7	min_contrast_4	10	0.434	90.616	0.345	min_contrast_4	10	0.419	180.943	0.689	0.015	-90.327	-0.344
US	8	min_contrast_4	10	0.426	91.647	0.35	min_contrast_4	10	0.417	181.294	0.692	0.009	-89.647	-0.342
US	9	min_contrast_4	10	0.446	92.044	0.351	min_contrast_4	10	0.434	181.748	0.693	0.012	-89.704	-0.342
US	10	min_contrast_4	10	0.356	93.236	0.357	pearson_chi_square	0.01	0.117	175.263	0.671	0.239	-82.027	-0.314

Table A.17: Testing performance of local and transferred physically-based models with US-tailored look-up table (LUT). The parameters correspond to the best-performing combination of parameters tested during the fivefold cross-validation. CH: Switzerland, ALB: Schwäbische Alb, HAI: Hainich-Dün, SCH: Schorfheide-Chorin, US: United States, R^2: coefficient of determination, RMSE: root-mean-square error, sRMSE: systematic component of RMSE, uRMSE: unsystematic component of RMSE, RRMSE: relative root-mean-square error, MBE: mean bias error.

		Calibration site				
Prediction site	**Metric**	**CH**	**ALB**	**HAI**	**SCH**	**US**
CH	**R^2**	0.19 ± 0.13	0.00 ± 0.00	0.04 ± 0.01	0.08 ± 0.00	0.08 ± 0.00
CH	**RMSE**	178.67 ± 17.06	243.85 ± 1.43	205.20 ± 3.28	191.83 ± 0.00	209.39 ± 0.00
CH	**sRMSE**	174.39 ± 16.33	190.96 ± 1.14	192.41 ± 1.93	184.07 ± 0.00	197.37 ± 0.00
CH	**uRMSE**	50.21 ± 16.79	151.61 ± 3.64	71.24 ± 4.32	54.00 ± 0.00	69.92 ± 0.00
CH	**RRMSE**	1.02 ± 0.11	1.40 ± 0.01	1.18 ± 0.02	1.10 ± 0.00	1.21 ± 0.00
CH	**MBE**	131.38 ± 26.00	155.84 ± 1.40	157.81 ± 2.34	147.59 ± 0.00	163.87 ± 0.00
ALB	**R^2**	0.39 ± 0.00	0.03 ± 0.06	0.23 ± 0.00	0.28 ± 0.00	0.38 ± 0.00
ALB	**RMSE**	247.91 ± 0.00	184.72 ± 26.81	194.44 ± 0.70	200.32 ± 0.00	256.10 ± 0.00
ALB	**sRMSE**	247.01 ± 0.00	119.67 ± 19.71	195.75 ± 0.76	202.49 ± 0.00	255.04 ± 0.00
ALB	**uRMSE**	21.15 ± 0.00	140.06 ± 22.64	22.58 ± 0.61	29.60 ± 0.00	23.24 ± 0.00
ALB	**RRMSE**	1.78 ± 0.00	1.32 ± 0.19	1.40 ± 0.01	1.44 ± 0.00	1.84 ± 0.00
ALB	**MBE**	232.16 ± 0.00	82.11 ± 27.44	176.57 ± 0.85	184.05 ± 0.00	240.69 ± 0.00
HAI	**R^2**	0.48 ± 0.00	0.02 ± 0.00	0.31 ± 0.11	0.41 ± 0.00	0.46 ± 0.00
HAI	**RMSE**	251.88 ± 0.00	223.38 ± 0.41	195.40 ± 13.23	206.53 ± 0.00	258.13 ± 0.00
HAI	**sRMSE**	255.37 ± 0.00	146.79 ± 0.46	199.40 ± 11.86	213.06 ± 0.00	261.40 ± 0.00
HAI	**uRMSE**	42.12 ± 0.00	168.38 ± 0.15	36.22 ± 15.28	52.33 ± 0.00	41.20 ± 0.00
HAI	**RRMSE**	2.17 ± 0.00	1.93 ± 0.00	1.70 ± 0.13	1.78 ± 0.00	2.22 ± 0.00
HAI	**MBE**	240.75 ± 0.00	118.96 ± 0.56	180.96 ± 16.51	195.27 ± 0.00	247.13 ± 0.00
SCH	**R^2**	0.16 ± 0.00	0.01 ± 0.00	0.02 ± 0.00	0.12 ± 0.06	0.15 ± 0.00
SCH	**RMSE**	202.61 ± 0.00	171.44 ± 0.78	160.21 ± 0.80	153.17 ± 10.08	209.93 ± 0.00
SCH	**sRMSE**	204.89 ± 0.00	121.59 ± 0.04	155.64 ± 0.39	156.26 ± 10.45	211.96 ± 0.00
SCH	**uRMSE**	30.48 ± 0.00	120.86 ± 1.08	37.93 ± 1.77	33.74 ± 13.43	29.31 ± 0.00
SCH	**RRMSE**	0.91 ± 0.00	0.77 ± 0.00	0.72 ± 0.00	0.69 ± 0.04	0.95 ± 0.00
SCH	**MBE**	166.86 ± 0.00	-23.08 ± 0.08	100.12 ± 0.59	99.35 ± 9.47	175.46 ± 0.00
US	**R^2**	0.42 ± 0.00	0.24 ± 0.04	0.44 ± 0.00	0.44 ± 0.00	0.51 ± 0.12
US	**RMSE**	110.88 ± 0.00	125.92 ± 2.43	92.36 ± 1.66	100.72 ± 0.00	87.52 ± 13.13
US	**sRMSE**	123.50 ± 0.00	127.06 ± 0.43	107.97 ± 1.56	115.29 ± 0.00	104.15 ± 13.18
US	**uRMSE**	54.39 ± 0.00	11.22 ± 12.61	55.91 ± 0.30	56.10 ± 0.00	55.88 ± 8.20
US	**RRMSE**	0.42 ± 0.00	0.48 ± 0.01	0.35 ± 0.01	0.39 ± 0.00	0.33 ± 0.05
US	**MBE**	-89.48 ± 0.00	-94.19 ± 0.62	-66.41 ± 2.51	-77.77 ± 0.00	-61.92 ± 7.33

Section A.20: PROSAIL forward model fit

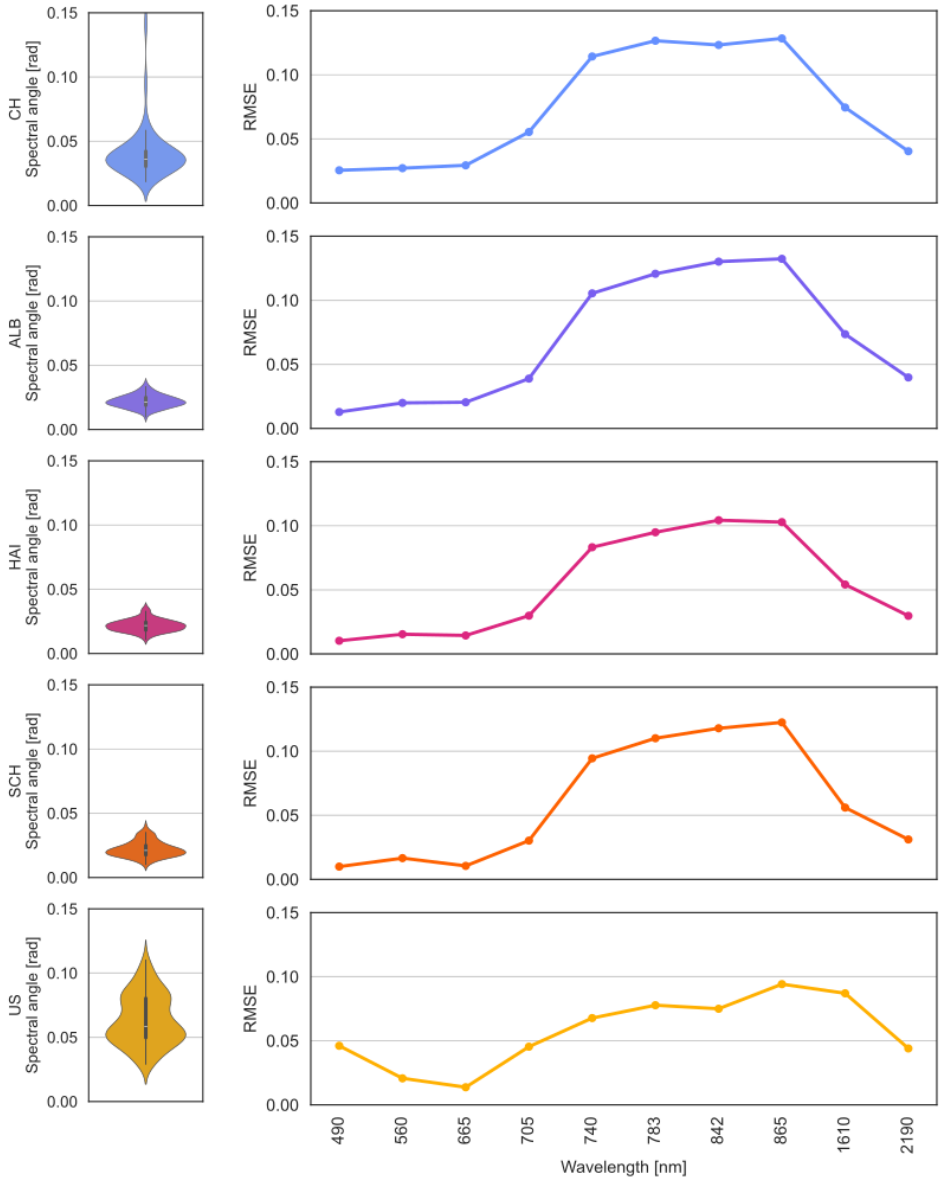

Figure 24: Violin plots show the smallest spectral angle (Yuhas et al., 1992) between the Sentinel-2 spectra and the PROSAIL simulations by site. Line plots show the root-mean-square error (RMSE) for the Sentinel-2 spectra and the closest PROSAIL simulations in terms of smallest spectral angle for each spectral band. CH: Switzerland, ALB: Schwäbische Alb, HAI: Hainich-Dün, SCH: Schorfheide-Chorin, US: United States.

Section A.21: Precipitation at US site

*Table A.1818: Summarized precipitation data in millimeters [mm] at the Norman (OK) weather station as provided by Mesonet (2024) for the summer months (June to August) from 2004-2023. * denotes the months in which the field measurements used in this study were conducted.*

Year	Monthly precipitation [mm]			Cumulative precipitation
	June	July	August	
2004	8.11	4.37	3.55	16.03
2005	3.51	2.60	4.92	11.03
2006	2.63	2.05	2.15	6.83
2007	10.82	8.08	6.09	24.99
2008	5.90	0.76	10.26	16.92
2009	1.27	3.56	4.59	9.42
2010	4.03	5.55	0.72	10.30
2011	2.35	0.34	2.06	4.75
2012	0.82	0.02	3.14	3.98
2013	4.16	9.56	2.73	16.45
2014	4.58	3.76	1.34	9.68
2015	5.95	7.46	1.74	15.15
2016	2.93	6.48	0.51	9.92
2017	0.66	2.43	8.43	11.52
2018	6.55	2.28	6.87	15.70
2019	5.67	0.18	6.61	12.46
2020	2.19	2.65	5.15	9.99
2021	6.54	2.70	1.46	10.70
2022	5.39	**1.19 ***	**0.84 ***	7.42
2023	5.13	7.62	0.59	13.34
Average	4.46	3.68	3.69	11.83

Section A.22: C3 and C4 species per study site

Information about the photosynthetic pathway of the species in the study sites investigated in this study were estimated from the TRY database (Cornelissen, 1996; Cornelissen et al., 2004; Cornwell et al., 2017, 2008; Craine et al., 2005; Diaz et al., 2004; Fitter and Peat, 1994; Flowers et al., 2023, 2017; Iversen et al., 2017; Kapralov et al., 2012; Kattge et al., 2020, 2009; Laughlin et al., 2011, 2010; Lin et al., 2015; Meir et al., 2002; Munroe et al., 2021; Poschlod et al., 2003; Quested et al., 2003; Reich et al., 2009, 2008; Smith and Dukes, 2017; Wang et al., 2017; Wright et al., 2004). We point out that the percentages indicated in Table A.19 relate to species occurrence and not species abundance. In fact, the abundance of C4 species was considerably higher for the US site. However, species abundance data was not available for all sites which is why we did not add a separate column.

Table A.19: Number of C3 and C4 species, and relative share of C4 species per study site. CH: Switzerland, ALB: Schwäbische Alb, HAI: Hainich-Dün, SCH: Schorfheide-Chorin, US: United States.

Study site	**Number of C3 species**	**Number of C4 species**	**Relative share of C4 species [%]**
CH	152	4	2.56
ALB	42	0	0.00
HAI	80	1	1.23
SCH	174	8	4.40
US	156	23	12.85

Section A.23: Transferability of local hybrid models with varying initial training set size

Table A.20: Testing performance of local and transferred hybrid models. The parameters correspond to the best-performing combination of parameters tested during the fivefold cross-validation using Active Learning with an initial training set size of 1%. CH: Switzerland, ALB: Schwäbische Alb, HAI: Hainich-Dün, SCH: Schorfheide-Chorin, US: United States, R^2: coefficient of determination, RMSE: root-mean-square error, sRMSE: systematic component of RMSE, uRMSE: unsystematic component of RMSE, RRMSE: relative root-mean-square error, MBE: mean bias error.

Initial training set size = 1%		**Calibration site**				
Prediction site	**Metric**	**CH**	**ALB**	**HAI**	**SCH**	**US**
CH	**R^2**	0.25 ± 0.19	0.03 ± 0.02	0.06 ± 0.06	0.02 ± 0.02	0.01 ± 0.02
CH	**RMSE**	103.69 ± 18.85	129.44 ± 8.99	134.83 ± 21.99	142.12 ± 9.30	191.62 ± 63.09
CH	**sRMSE**	113.31 ± 9.08	119.74 ± 9.18	122.02 ± 12.26	121.00 ± 9.74	171.73 ± 52.16
CH	**uRMSE**	47.11 ± 27.93	45.47 ± 18.60	52.98 ± 38.71	72.81 ± 15.75	71.14 ± 58.50
CH	**RRMSE**	0.59 ± 0.10	0.75 ± 0.05	0.78 ± 0.13	0.82 ± 0.05	1.10 ± 0.36
CH	**MBE**	-2.72 ± 13.49	-41.46 ± 23.45	-40.36 ± 35.62	5.02 ± 50.57	126.33 ± 63.89
ALB	**R^2**	0.08 ± 0.10	0.49 ± 0.17	0.32 ± 0.10	0.40 ± 0.07	0.06 ± 0.06
ALB	**RMSE**	126.21 ± 16.94	62.87 ± 10.57	74.22 ± 7.02	111.74 ± 12.28	162.29 ± 23.31
ALB	**sRMSE**	108.82 ± 16.12	85.15 ± 4.63	85.61 ± 0.94	120.57 ± 8.51	143.02 ± 14.02
ALB	**uRMSE**	59.38 ± 24.24	54.70 ± 14.70	41.52 ± 11.89	43.36 ± 9.64	61.41 ± 49.65
ALB	**RRMSE**	0.91 ± 0.12	0.45 ± 0.07	0.53 ± 0.05	0.80 ± 0.09	1.17 ± 0.17
ALB	**MBE**	65.03 ± 25.47	0.44 ± 13.69	-12.72 ± 6.51	85.76 ± 11.92	114.26 ± 18.83
HAI	**R^2**	0.06 ± 0.06	0.37 ± 0.10	0.51 ± 0.13	0.26 ± 0.08	0.08 ± 0.09
HAI	**RMSE**	135.73 ± 8.34	70.17 ± 7.51	60.93 ± 11.56	112.65 ± 10.12	188.68 ± 31.60
HAI	**sRMSE**	118.33 ± 13.62	86.30 ± 0.99	82.65 ± 9.90	116.60 ± 4.41	167.83 ± 26.43
HAI	**uRMSE**	62.44 ± 20.15	48.49 ± 10.83	54.56 ± 10.28	36.40 ± 12.60	70.53 ± 52.63
HAI	**RRMSE**	1.17 ± 0.07	0.60 ± 0.06	0.53 ± 0.09	0.97 ± 0.09	1.63 ± 0.27
HAI	**MBE**	79.76 ± 21.29	1.45 ± 13.36	-5.70 ± 6.34	79.31 ± 6.29	143.04 ± 31.57
SCH	**R^2**	0.04 ± 0.06	0.25 ± 0.05	0.17 ± 0.07	0.29 ± 0.12	0.07 ± 0.08
SCH	**RMSE**	139.32 ± 13.87	128.55 ± 9.52	143.68 ± 8.58	108.25 ± 12.61	151.20 ± 25.32
SCH	**sRMSE**	127.16 ± 10.54	141.13 ± 6.90	150.62 ± 4.83	120.60 ± 11.47	125.22 ± 2.90
SCH	**uRMSE**	54.08 ± 19.89	57.44 ± 6.97	42.75 ± 15.06	58.95 ± 11.45	69.11 ± 55.27
SCH	**RRMSE**	0.63 ± 0.06	0.58 ± 0.04	0.65 ± 0.04	0.49 ± 0.05	0.68 ± 0.11
SCH	**MBE**	-33.08 ± 31.21	-75.39 ± 12.86	-92.23 ± 8.13	0.41 ± 12.44	24.95 ± 28.13
US	**R^2**	0.11 ± 0.12	0.10 ± 0.08	0.18 ± 0.13	0.19 ± 0.10	0.30 ± 0.25
US	**RMSE**	226.44 ± 69.67	204.36 ± 51.18	197.08 ± 52.07	148.20 ± 37.87	72.09 ± 14.27
US	**sRMSE**	210.86 ± 61.49	200.61 ± 51.46	185.05 ± 60.75	125.16 ± 38.69	84.44 ± 12.64
US	**uRMSE**	76.37 ± 45.34	37.57 ± 20.66	58.73 ± 27.86	72.22 ± 36.25	34.16 ± 27.01
US	**RRMSE**	0.87 ± 0.27	0.78 ± 0.20	0.75 ± 0.20	0.57 ± 0.14	0.28 ± 0.05
US	**MBE**	-190.17 ± 68.45	-179.42 ± 57.72	-159.16 ± 72.14	-79.48 ± 58.63	1.16 ± 10.21

Table A.21: Testing performance of local and transferred hybrid models. The parameters correspond to the best-performing combination of parameters tested during the fivefold cross-validation using Active Learning with an initial training set size of 2%. CH: Switzerland, ALB: Schwäbische Alb, HAI: Hainich-Dün, SCH: Schorfheide-Chorin, US: United States, R^2: coefficient of determination, RMSE: root-mean-square error, sRMSE: systematic component of RMSE, uRMSE: unsystematic component of RMSE, RRMSE: relative root-mean-square error, MBE: mean bias error.

Initial training set size = 2%		**Calibration site**				
Prediction site	**Metric**	**CH**	**ALB**	**HAI**	**SCH**	**US**
CH	**R^2**	0.23 ± 0.14	0.02 ± 0.02	0.02 ± 0.03	0.03 ± 0.03	0.01 ± 0.01
CH	**RMSE**	112.22 ± 31.13	127.07 ± 7.94	125.43 ± 9.89	136.69 ± 13.00	164.02 ± 35.27
CH	**sRMSE**	113.87 ± 9.18	116.51 ± 7.64	117.34 ± 6.45	125.35 ± 13.19	146.02 ± 14.56
CH	**uRMSE**	54.73 ± 39.46	49.79 ± 13.76	44.33 ± 15.06	53.38 ± 17.36	58.53 ± 64.41
CH	**RRMSE**	0.64 ± 0.18	0.73 ± 0.05	0.72 ± 0.06	0.79 ± 0.07	0.94 ± 0.20
CH	**MBE**	-3.46 ± 17.01	-31.66 ± 21.59	-36.42 ± 18.12	36.96 ± 48.54	93.61 ± 20.14
ALB	**R^2**	0.07 ± 0.07	0.46 ± 0.18	0.34 ± 0.07	0.41 ± 0.09	0.03 ± 0.02
ALB	**RMSE**	122.05 ± 8.44	64.39 ± 11.93	72.30 ± 4.12	107.21 ± 8.09	158.60 ± 28.14
ALB	**sRMSE**	103.03 ± 10.46	84.85 ± 4.76	86.83 ± 1.25	118.81 ± 4.89	147.49 ± 33.86
ALB	**uRMSE**	61.51 ± 21.43	54.13 ± 12.30	47.60 ± 5.58	50.35 ± 6.74	42.55 ± 41.87
ALB	**RRMSE**	0.88 ± 0.06	0.46 ± 0.08	0.52 ± 0.03	0.77 ± 0.06	1.14 ± 0.20
ALB	**MBE**	55.91 ± 19.27	-0.37 ± 11.47	-19.74 ± 5.34	83.55 ± 6.82	117.33 ± 42.37
HAI	**R^2**	0.03 ± 0.03	0.32 ± 0.04	0.54 ± 0.11	0.25 ± 0.06	0.02 ± 0.03
HAI	**RMSE**	131.67 ± 12.72	72.81 ± 1.65	58.51 ± 11.47	110.02 ± 5.09	179.92 ± 31.30
HAI	**sRMSE**	112.79 ± 15.17	86.15 ± 0.83	83.22 ± 9.76	115.72 ± 4.17	171.60 ± 35.17
HAI	**uRMSE**	65.35 ± 16.62	45.90 ± 3.40	58.49 ± 6.67	35.08 ± 7.02	40.01 ± 41.06
HAI	**RRMSE**	1.13 ± 0.11	0.63 ± 0.01	0.51 ± 0.09	0.95 ± 0.04	1.55 ± 0.27
HAI	**MBE**	70.71 ± 24.06	0.42 ± 12.18	-9.55 ± 8.77	78.01 ± 6.21	146.89 ± 38.34
SCH	**R^2**	0.02 ± 0.02	0.23 ± 0.04	0.17 ± 0.07	0.27 ± 0.15	0.02 ± 0.03
SCH	**RMSE**	142.90 ± 12.30	129.56 ± 8.21	144.81 ± 6.85	104.35 ± 14.22	144.01 ± 25.57
SCH	**sRMSE**	129.70 ± 11.57	141.33 ± 6.42	152.09 ± 3.38	120.30 ± 11.46	132.76 ± 16.64
SCH	**uRMSE**	58.91 ± 12.09	56.03 ± 4.71	44.91 ± 12.62	56.42 ± 18.15	46.69 ± 44.79
SCH	**RRMSE**	0.64 ± 0.06	0.58 ± 0.04	0.65 ± 0.03	0.47 ± 0.06	0.65 ± 0.12
SCH	**MBE**	-44.35 ± 27.74	-75.77 ± 12.38	-94.74 ± 5.45	-0.14 ± 8.90	39.24 ± 43.46
US	**R^2**	0.13 ± 0.10	0.12 ± 0.10	0.14 ± 0.11	0.19 ± 0.05	0.23 ± 0.26
US	**RMSE**	184.27 ± 27.00	161.10 ± 38.01	155.40 ± 9.64	118.22 ± 23.46	76.40 ± 20.77
US	**sRMSE**	171.80 ± 24.72	159.96 ± 38.99	148.05 ± 10.26	106.73 ± 19.36	84.04 ± 13.67
US	**uRMSE**	63.41 ± 27.27	33.24 ± 13.22	45.41 ± 12.44	52.36 ± 23.27	22.45 ± 24.84
US	**RRMSE**	0.70 ± 0.10	0.62 ± 0.15	0.59 ± 0.04	0.45 ± 0.09	0.29 ± 0.07
US	**MBE**	-148.09 ± 28.52	-132.65 ± 46.57	-120.22 ± 12.54	-48.41 ± 44.96	0.49 ± 7.92

Table A.22: Testing performance of local and transferred hybrid models. The parameters correspond to the best-performing combination of parameters tested during the fivefold cross-validation using Active Learning with an initial training set size of 5%. CH: Switzerland, ALB: Schwäbische Alb, HAI: Hainich-Dün, SCH: Schorfheide-Chorin, US: United States, R^2: coefficient of determination, RMSE: root-mean-square error, sRMSE: systematic component of RMSE, uRMSE: unsystematic component of RMSE, RRMSE: relative root-mean-square error, MBE: mean bias error.

Initial training set size = 5%		**Calibration site**				
Prediction site	**Metric**	**CH**	**ALB**	**HAI**	**SCH**	**US**
CH	**R^2**	0.15 ± 0.15	0.02 ± 0.02	0.01 ± 0.01	0.02 ± 0.02	0.01 ± 0.01
CH	**RMSE**	111.07 ± 19.79	120.25 ± 4.85	120.99 ± 5.25	140.38 ± 6.01	143.60 ± 7.80
CH	**sRMSE**	114.20 ± 9.45	112.32 ± 1.75	115.70 ± 2.65	134.66 ± 4.40	141.40 ± 1.41
CH	**uRMSE**	44.88 ± 23.47	39.92 ± 16.58	31.77 ± 16.23	37.52 ± 13.52	10.75 ± 24.04
CH	**RRMSE**	0.63 ± 0.11	0.69 ± 0.03	0.70 ± 0.03	0.81 ± 0.03	0.83 ± 0.04
CH	**MBE**	-13.64 ± 13.37	-18.65 ± 10.31	-34.13 ± 8.57	76.89 ± 7.50	88.51 ± 2.21
ALB	**R^2**	0.04 ± 0.04	0.44 ± 0.16	0.30 ± 0.08	0.37 ± 0.09	0.02 ± 0.04
ALB	**RMSE**	113.02 ± 16.52	64.96 ± 10.37	73.35 ± 4.82	106.73 ± 8.13	152.55 ± 10.94
ALB	**sRMSE**	97.54 ± 10.32	84.72 ± 4.70	86.16 ± 1.01	118.23 ± 5.02	144.84 ± 12.28
ALB	**uRMSE**	53.11 ± 24.62	55.35 ± 8.69	44.39 ± 7.09	50.06 ± 6.30	16.82 ± 44.59
ALB	**RRMSE**	0.81 ± 0.12	0.46 ± 0.07	0.53 ± 0.03	0.77 ± 0.06	1.10 ± 0.08
ALB	**MBE**	44.89 ± 19.52	1.22 ± 10.29	-16.04 ± 6.17	82.66 ± 7.32	116.72 ± 16.84
HAI	**R^2**	0.05 ± 0.06	0.26 ± 0.08	0.46 ± 0.13	0.22 ± 0.07	0.02 ± 0.02
HAI	**RMSE**	125.35 ± 18.84	76.21 ± 4.91	63.10 ± 11.90	107.83 ± 7.36	171.78 ± 8.86
HAI	**sRMSE**	106.93 ± 9.33	85.54 ± 0.22	83.12 ± 9.67	113.64 ± 5.75	166.19 ± 8.06
HAI	**uRMSE**	61.60 ± 28.97	37.05 ± 10.57	52.57 ± 10.79	33.82 ± 11.05	16.02 ± 40.76
HAI	**RRMSE**	1.08 ± 0.16	0.66 ± 0.04	0.55 ± 0.09	0.93 ± 0.06	1.48 ± 0.08
HAI	**MBE**	62.55 ± 15.42	1.85 ± 5.40	-4.17 ± 11.12	74.69 ± 8.72	142.14 ± 9.74
SCH	**R^2**	0.02 ± 0.03	0.19 ± 0.05	0.13 ± 0.04	0.22 ± 0.08	0.01 ± 0.01
SCH	**RMSE**	142.94 ± 9.99	134.32 ± 4.59	147.07 ± 5.50	108.28 ± 11.79	131.14 ± 16.47
SCH	**sRMSE**	130.85 ± 5.26	143.28 ± 3.57	152.39 ± 3.78	121.01 ± 11.26	125.12 ± 1.57
SCH	**uRMSE**	54.97 ± 22.31	49.01 ± 8.91	38.37 ± 10.96	52.54 ± 12.04	15.61 ± 39.65
SCH	**RRMSE**	0.64 ± 0.05	0.61 ± 0.02	0.66 ± 0.02	0.49 ± 0.04	0.59 ± 0.07
SCH	**MBE**	-51.63 ± 16.42	-79.81 ± 6.50	-95.12 ± 6.11	-5.58 ± 14.29	34.03 ± 16.48
US	**R^2**	0.09 ± 0.09	0.18 ± 0.06	0.20 ± 0.05	0.19 ± 0.03	0.11 ± 0.17
US	**RMSE**	147.63 ± 26.06	163.08 ± 11.32	152.60 ± 7.63	102.45 ± 8.77	82.00 ± 16.11
US	**sRMSE**	142.80 ± 19.56	151.49 ± 11.25	145.50 ± 7.02	89.77 ± 5.75	82.40 ± 10.50
US	**uRMSE**	43.32 ± 20.47	59.97 ± 7.16	45.30 ± 8.60	48.85 ± 9.79	10.56 ± 16.63
US	**RRMSE**	0.56 ± 0.10	0.62 ± 0.04	0.58 ± 0.03	0.39 ± 0.03	0.31 ± 0.06
US	**MBE**	-113.41 ± 23.40	-124.34 ± 13.64	-117.09 ± 8.69	-18.94 ± 17.36	-1.07 ± 5.78

Table A.23: Testing performance of local and transferred hybrid models. The parameters correspond to the best-performing combination of parameters tested during the fivefold cross-validation using Active Learning with an initial training set size of 10%. CH: Switzerland, ALB: Schwäbische Alb, HAI: Hainich-Dün, SCH: Schorfheide-Chorin, US: United States, R^2: coefficient of determination, RMSE: root-mean-square error, sRMSE: systematic component of RMSE, uRMSE: unsystematic component of RMSE, RRMSE: relative root-mean-square error, MBE: mean bias error.

Initial training set size = 10%		**Calibration site**				
Prediction site	**Metric**	**CH**	**ALB**	**HAI**	**SCH**	**US**
CH	**R^2**	0.17 ± 0.17	0.02 ± 0.01	0.02 ± 0.03	0.01 ± 0.02	0.01 ± 0.03
CH	**RMSE**	104.26 ± 15.57	117.78 ± 3.98	118.99 ± 2.31	138.46 ± 3.69	141.06 ± 0.68
CH	**sRMSE**	113.18 ± 8.79	111.64 ± 0.99	115.54 ± 2.58	135.89 ± 4.20	140.93 ± 0.76
CH	**uRMSE**	34.21 ± 26.09	35.90 ± 13.64	26.58 ± 11.38	25.48 ± 7.16	0.89 ± 2.34
CH	**RRMSE**	0.60 ± 0.08	0.68 ± 0.02	0.69 ± 0.01	0.80 ± 0.02	0.81 ± 0.00
CH	**MBE**	-4.20 ± 10.30	-17.59 ± 9.13	-33.37 ± 8.68	79.04 ± 7.44	87.96 ± 1.08
ALB	**R^2**	0.03 ± 0.04	0.32 ± 0.21	0.27 ± 0.09	0.29 ± 0.10	0.00 ± 0.00
ALB	**RMSE**	102.02 ± 10.17	71.02 ± 12.27	74.43 ± 3.86	110.90 ± 5.44	149.05 ± 0.90
ALB	**sRMSE**	94.03 ± 5.34	84.82 ± 4.60	85.93 ± 0.66	119.22 ± 3.30	148.91 ± 0.95
ALB	**uRMSE**	34.53 ± 24.13	41.66 ± 20.56	41.94 ± 8.43	42.80 ± 7.97	0.08 ± 0.20
ALB	**RRMSE**	0.73 ± 0.07	0.51 ± 0.08	0.53 ± 0.03	0.80 ± 0.04	1.07 ± 0.01
ALB	**MBE**	38.65 ± 12.74	1.15 ± 9.86	-15.28 ± 4.10	84.09 ± 4.60	122.46 ± 1.10
HAI	**R^2**	0.04 ± 0.06	0.19 ± 0.07	0.39 ± 0.15	0.18 ± 0.07	0.00 ± 0.01
HAI	**RMSE**	119.38 ± 14.55	81.05 ± 4.65	67.97 ± 13.90	111.40 ± 5.62	169.02 ± 0.99
HAI	**sRMSE**	105.85 ± 9.46	85.95 ± 0.67	82.95 ± 9.52	115.88 ± 3.43	168.84 ± 1.10
HAI	**uRMSE**	45.78 ± 32.95	29.93 ± 9.05	45.05 ± 11.36	29.84 ± 11.23	1.37 ± 2.93
HAI	**RRMSE**	1.03 ± 0.13	0.70 ± 0.04	0.59 ± 0.11	0.96 ± 0.05	1.46 ± 0.01
HAI	**MBE**	60.19 ± 17.35	1.81 ± 11.26	-4.00 ± 9.09	78.19 ± 5.01	145.55 ± 1.23
SCH	**R^2**	0.01 ± 0.01	0.18 ± 0.06	0.10 ± 0.04	0.19 ± 0.12	0.00 ± 0.01
SCH	**RMSE**	138.26 ± 10.83	139.34 ± 4.02	149.11 ± 4.27	110.25 ± 11.89	125.74 ± 0.36
SCH	**sRMSE**	130.54 ± 9.74	147.00 ± 3.88	153.22 ± 2.61	120.60 ± 11.67	125.65 ± 0.38
SCH	**uRMSE**	40.52 ± 21.39	47.67 ± 11.13	33.54 ± 10.32	45.77 ± 18.46	1.70 ± 2.33
SCH	**RRMSE**	0.62 ± 0.05	0.63 ± 0.02	0.67 ± 0.02	0.50 ± 0.05	0.57 ± 0.00
SCH	**MBE**	-47.97 ± 24.76	-86.04 ± 6.35	-96.47 ± 4.13	-7.42 ± 8.90	39.67 ± 1.17
US	**R^2**	0.05 ± 0.04	0.18 ± 0.06	0.15 ± 0.07	0.17 ± 0.04	0.08 ± 0.20
US	**RMSE**	142.09 ± 13.04	156.92 ± 11.19	158.49 ± 7.94	94.97 ± 3.44	84.34 ± 12.95
US	**sRMSE**	140.19 ± 10.94	148.43 ± 9.00	153.74 ± 8.54	87.67 ± 1.33	82.16 ± 10.98
US	**uRMSE**	24.30 ± 16.72	51.18 ± 16.01	37.17 ± 9.65	35.88 ± 7.41	1.63 ± 4.32
US	**RRMSE**	0.54 ± 0.05	0.60 ± 0.04	0.61 ± 0.03	0.36 ± 0.01	0.32 ± 0.04
US	**MBE**	-110.53 ± 13.95	-120.95 ± 10.53	-127.21 ± 10.27	-13.80 ± 8.37	0.28 ± 5.41

Table A.24: Testing performance of local and transferred hybrid models. The parameters correspond to the best-performing combination of parameters tested during the fivefold cross-validation using Active Learning with an initial training set size of 100% (= no Active Learning). CH: Switzerland, ALB: Schwäbische Alb, HAI: Hainich-Dün, SCH: Schorfheide-Chorin, US: United States, R^2: coefficient of determination, RMSE: root-mean-square error, sRMSE: systematic component of RMSE, uRMSE: unsystematic component of RMSE, RRMSE: relative root-mean-square error, MBE: mean bias error.

Initial training set size = 100% (= no Active Learning)		**Calibration site**				
Prediction site	**Metric**	**CH**	**ALB**	**HAI**	**SCH**	**US**
CH	**R^2**	0.07 ± 0.07	0.03 ± 0.00	0.03 ± 0.00	0.03 ± 0.00	0.03 ± 0.00
CH	**RMSE**	112.71 ± 8.67	109.87 ± 0.00	109.87 ± 0.00	109.87 ± 0.00	109.87 ± 0.00
CH	**sRMSE**	112.96 ± 8.67	110.10 ± 0.00	110.10 ± 0.00	110.10 ± 0.00	110.10 ± 0.00
CH	**uRMSE**	7.59 ± 4.63	7.18 ± 0.00	7.18 ± 0.00	7.18 ± 0.00	7.18 ± 0.00
CH	**RRMSE**	0.64 ± 0.04	0.63 ± 0.00	0.63 ± 0.00	0.63 ± 0.00	0.63 ± 0.00
CH	**MBE**	0.07 ± 3.45	0.99 ± 0.00	0.99 ± 0.00	0.99 ± 0.00	0.99 ± 0.00
ALB	**R^2**	0.06 ± 0.00	0.09 ± 0.05	0.06 ± 0.00	0.06 ± 0.00	0.06 ± 0.00
ALB	**RMSE**	89.47 ± 0.00	89.24 ± 3.93	89.47 ± 0.00	89.47 ± 0.00	89.47 ± 0.00
ALB	**sRMSE**	90.72 ± 0.00	90.41 ± 3.59	90.72 ± 0.00	90.72 ± 0.00	90.72 ± 0.00
ALB	**uRMSE**	14.99 ± 0.00	13.53 ± 5.02	14.99 ± 0.00	14.99 ± 0.00	14.99 ± 0.00
ALB	**RRMSE**	0.64 ± 0.00	0.64 ± 0.02	0.64 ± 0.00	0.64 ± 0.00	0.64 ± 0.00
ALB	**MBE**	32.42 ± 0.00	32.03 ± 2.86	32.42 ± 0.00	32.42 ± 0.00	32.42 ± 0.00
HAI	**R^2**	0.03 ± 0.00	0.03 ± 0.00	0.08 ± 0.06	0.03 ± 0.00	0.03 ± 0.00
HAI	**RMSE**	100.17 ± 0.00	100.17 ± 0.00	98.26 ± 7.91	100.17 ± 0.00	100.17 ± 0.00
HAI	**sRMSE**	100.91 ± 0.00	100.91 ± 0.00	99.17 ± 7.33	100.91 ± 0.00	100.91 ± 0.00
HAI	**uRMSE**	12.20 ± 0.00	12.20 ± 0.00	14.74 ± 2.59	12.20 ± 0.00	12.20 ± 0.00
HAI	**RRMSE**	0.86 ± 0.00	0.86 ± 0.00	0.85 ± 0.05	0.86 ± 0.00	0.86 ± 0.00
HAI	**MBE**	53.30 ± 0.00	53.30 ± 0.00	54.24 ± 2.70	53.30 ± 0.00	53.30 ± 0.00
SCH	**R^2**	0.08 ± 0.00	0.08 ± 0.00	0.08 ± 0.00	0.09 ± 0.07	0.08 ± 0.00
SCH	**RMSE**	128.15 ± 0.00	128.15 ± 0.00	128.15 ± 0.00	129.58 ± 12.06	128.15 ± 0.00
SCH	**sRMSE**	130.20 ± 0.00	130.20 ± 0.00	130.20 ± 0.00	131.46 ± 12.23	130.20 ± 0.00
SCH	**uRMSE**	23.03 ± 0.00	23.03 ± 0.00	23.03 ± 0.00	20.49 ± 8.84	23.03 ± 0.00
SCH	**RRMSE**	0.58 ± 0.00	0.58 ± 0.00	0.58 ± 0.00	0.58 ± 0.04	0.58 ± 0.00
SCH	**MBE**	-52.78 ± 0.00	-52.78 ± 0.00	-52.78 ± 0.00	-53.14 ± 5.05	-52.78 ± 0.00
US	**R^2**	0.02 ± 0.00	0.02 ± 0.00	0.02 ± 0.00	0.02 ± 0.00	0.07 ± 0.08
US	**RMSE**	122.36 ± 0.00	122.36 ± 0.00	122.36 ± 0.00	122.36 ± 0.00	121.22 ± 12.12
US	**sRMSE**	122.41 ± 0.00	122.41 ± 0.00	122.41 ± 0.00	122.41 ± 0.00	121.32 ± 12.08
US	**uRMSE**	3.69 ± 0.00	3.69 ± 0.00	3.69 ± 0.00	3.69 ± 0.00	4.87 ± 1.51
US	**RRMSE**	0.47 ± 0.00	0.47 ± 0.00	0.47 ± 0.00	0.47 ± 0.00	0.46 ± 0.04
US	**MBE**	-87.21 ± 0.00	-87.21 ± 0.00	-87.21 ± 0.00	-87.21 ± 0.00	-86.97 ± 4.31

Section A.24: Mean field spectrum and AL-selected spectra by site

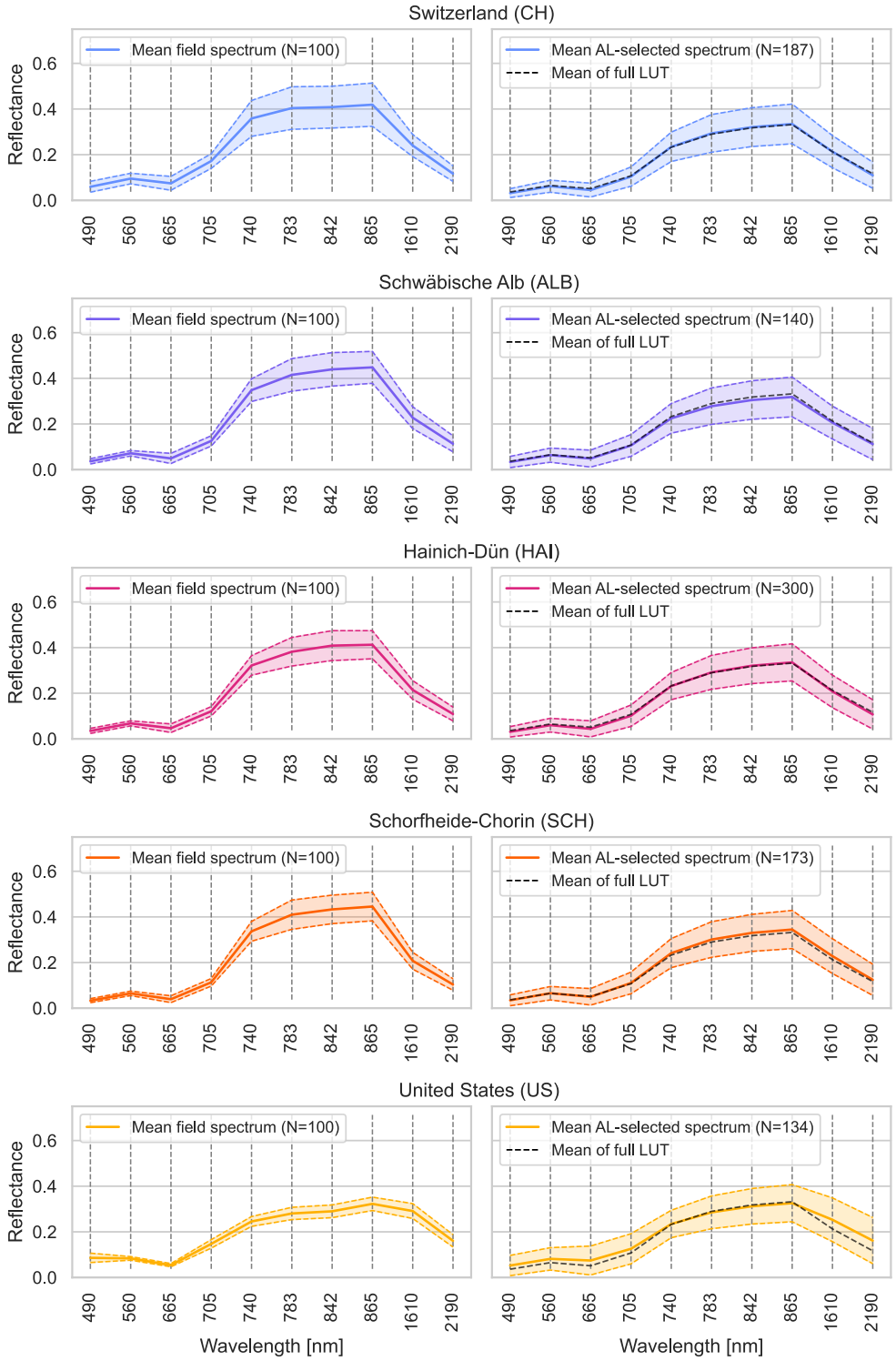

Figure A.25: Line plots of selected field spectra (left columns) and Active Learning (AL) selected training spectra of the look-up table (LUT) of the best performing local hybrid model with an initial training set size of 2% in terms of lowest relative root-mean-square error (right column) by study site. Bold lines represent mean spectra and colored areas represent the mean spectra ± 1 standard deviation.

References

Chen, T., Guestrin, C., 2016. XGBoost: A scalable tree boosting system. Proceedings of the ACM SIGKDD International Conference on Knowledge Discovery and Data Mining 13-17-August-2016, 785–794. https://doi.org/10.1145/2939672.2939785

Combal, B., Baret, F., Weiss, M., Trubuil, A., Macé, D., Pragnère, A., Myneni, R., Knyazikhin, Y., Wang, L., 2003. Retrieval of canopy biophysical variables from bidirectional reflectance. Remote Sens Environ 84, 1–15. https://doi.org/10.1016/S0034-4257(02)00035-4

Cornelissen, J.H.C., 1996. An Experimental Comparison of Leaf Decomposition Rates in a Wide Range of Temperate Plant Species and Types. J Ecol 84, 573–582. https://doi.org/10.2307/2261479

Cornelissen, J.H.C., Quested, H.M., Gwynn-Jones, D., Van Logtestijn, R.S.P., De Beus, M.A.H., Kondratchuk, A., Callaghan, T. V., Aerts, R., 2004. Leaf Digestibility and Litter Decomposability Are Related in a Wide Range of Subarctic Plant Species and Types. Funct Ecol 18, 779–786.

Cornwell, W.K., Cornelissen, J.H.C., Amatangelo, K., Dorrepaal, E., Eviner, V.T., Godoy, O., Hobbie, S.E., Hoorens, B., Kurokawa, H., Pérez-Harguindeguy, N., Quested, H.M., Santiago, L.S., Wardle, D.A., Wright, I.J., Aerts, R., Allison, S.D., Van Bodegom, P., Brovkin, V., Chatain, A., Callaghan, T. V., Díaz, S., Garnier, E., Gurvich, D.E., Kazakou, E., Klein, J.A., Read, J., Reich, P.B., Soudzilovskaia, N.A., Vaieretti, M.V., Westoby, M., 2008. Plant species traits are the predominant control on litter decomposition rates within biomes worldwide. Ecol Lett 11, 1065–1071. https://doi.org/10.1111/j.1461-0248.2008.01219.x

Cornwell, W.K., Wright, I., Turner, J., Maire, V., Barbour, M., Cernusak, L., Dawson, T., Ellsworth, D., Farquhar, G., Griffiths, H., Keitel, C., Knohl, A., Reich, P., Williams, D., Bhaskar, R., Cornelissen, J.H.C., Richards, A., Schmidt, S., Valladares, F., Körner, C., Schulze, E., Buchmann, N., Santiago, L., 2017. A global dataset of leaf D13 C values.

Craine, J.M., Lee, W.G., Bond, W.J., Williams, R.J., Johnson, L.C., 2005. Environmental constraints on a global relationship among leaf and root traits of grasses. Ecology 86, 12–19. https://doi.org/10.1890/04-1075

Diaz, S., Hodgson, J.G., Thompson, K., Cabido, M., Cornelissen, J.H.C., Jalili, A., Montserrat-Martí, G., Grime, J.P., Zarrinkamar, F., Asri, Y., Band, S.R., Basconcelo, S., Castro-Díez, P., Funes, G., Hamzehee, B., Khoshnevi, M., Pérez-Harguindeguy, N., Pérez-Rontomé, M.C., Shirvany, F.A., Vendramini, F., Yazdani, S., Abbas-Azimi, R., Bogaard, A., Boustani, S., Charles, M., Dehghan, M., de Torres-Espuny, L., Falczuk, V., Guerrero-Campo, J., Hynd, A., Jones, G., Kowsary, E., Kazemi-Saeed, F., Maestro-Martínez, M., Romo-Díez, A., Shaw, S., Siavash, B., Villar-Salvador, P., Zak, M.R., 2004. The plant traits that drive ecosystems: Evidence from three continents. Journal of Vegetation Science 15, 295–304. https://doi.org/10.1111/j.1654-1103.2004.tb02266.x

ESA, 2015. Sentinel-2 User Handbook Issue 1 Revision 2. Noordwijk.

Fitter, A.H., Peat, H.J., 1994. The Ecological Flora Database. J Ecol 82, 415–425. https://doi.org/10.2307/2261309

Flowers, T., Santos, J., Jahns, M., Warburton, B., Reed, P., 2023. eHALOPH - Halophytes Database (version 3.11) [WWW Document]. URL http://www.sussex.ac.uk/affiliates/halophytes, (accessed 11.28.23).

Flowers, T., Santos, J., Jahns, M., Warburton, B., Reed, P., 2017. eHALOPH - Halophytes Database (version 3.11) [WWW Document]. URL http://www.sussex.ac.uk/affiliates/halophytes, (accessed 1.1.17).

Huete, A.R., Liu, H., van Leeuwen, W.J.D., 1997. The use of vegetation indices in forested regions: issues of linearity and saturation, in: IGARSS'97. 1997 IEEE International Geoscience and Remote Sensing Symposium Proceedings. Remote Sensing - A Scientific Vision for Sustainable Development. IEEE, pp. 1966–1968. https://doi.org/10.1109/IGARSS.1997.609169

Iversen, C.M., McCormack, M.L., Powell, A.S., Blackwood, C.B., Freschet, G.T., Kattge, J., Roumet, C., Stover, D.B., Soudzilovskaia, N.A., Valverde-Barrantes, O.J., van Bodegom, P.M., Violle, C., 2017. A global Fine-Root Ecology Database to address below-ground challenges in plant ecology. New Phytologist 215, 15–26. https://doi.org/10.1111/nph.14486

Jehle, M., Hueni, A., Damm, A., D'Odorico, P., Weyermann, J., Kneubiihler, M., Schlapfer, D., Schaepman, M.E., Meuleman, K., 2010. APEX - current status, performance and validation concept, in: 2010 IEEE Sensors. IEEE, pp. 533–537. https://doi.org/10.1109/ICSENS.2010.5690122

Kapralov, M. V., Smith, J.A.C., Filatov, D.A., 2012. Rubisco Evolution in C4 Eudicots: An Analysis of Amaranthaceae Sensu Lato. PLoS One 7, e52974. https://doi.org/10.1371/journal.pone.0052974

Kattge, J., Bönisch, G., Díaz, S., Lavorel, S., Prentice, I.C., Leadley, P., Tautenhahn, S., Werner, G.D.A., Aakala, T., Abedi, M., Acosta, A.T.R., Adamidis, G.C., Adamson, K., Aiba, M., Albert, C.H., Alcántara, J.M., Alcázar C, C., Aleixo, I., Ali, H., Amiaud, B., Ammer, C., Amoroso, M.M., Anand, M., Anderson, C., Anten, N., Antos, J., Apgaua, D.M.G., Ashman, T., Asmara, D.H., Asner, G.P., Aspinwall, M., Atkin, O., Aubin, I., Baastrup-Spohr, L., Bahalkeh, K., Bahn, M., Baker, T., Baker, W.J., Bakker, J.P., Baldocchi, D., Baltzer, J., Banerjee, A., Baranger, A., Barlow, J., Barneche, D.R., Baruch, Z., Bastianelli, D., Battles, J., Bauerle, W., Bauters, M., Bazzato, E., Beckmann, M., Beeckman, H., Beierkuhnlein, C., Bekker, R., Belfry, G., Belluau, M., Beloiu, M., Benavides, R., Benomar, L., Berdugo-Lattke, M.L., Berenguer, E., Bergamin, R., Bergmann, J., Bergmann Carlucci, M., Berner, L., Bernhardt-Römermann, M., Bigler, C., Bjorkman, A.D., Blackman, C., Blanco, C., Blonder, B., Blumenthal, D., Bocanegra-González, K.T., Boeckx, P., Bohlman, S., Böhning-Gaese, K., Boisvert-Marsh, L., Bond, W., Bond-Lamberty, B., Boom, A., Boonman, C.C.F., Bordin, K., Boughton, E.H., Boukili, V., Bowman, D.M.J.S., Bravo, S., Brendel, M.R., Broadley, M.R., Brown, K.A., Bruelheide, H., Brumnich, F., Bruun, H.H., Bruy, D., Buchanan, S.W., Bucher, S.F., Buchmann, N., Buitenwerf, R., Bunker, D.E., Bürger, J., Burrascano, S., Burslem, D.F.R.P., Butterfield, B.J., Byun, C., Marques, M., Scalon, M.C., Caccianiga, M., Cadotte, M., Cailleret, M., Camac, J., Camarero, J.J., Campany, C., Campetella, G., Campos, J.A., Cano-Arboleda, L., Canullo, R., Carbognani, M., Carvalho, F., Casanoves, F., Castagneyrol, B., Catford, J.A., Cavender-Bares, J., Cerabolini, B.E.L., Cervellini, M., Chacón-Madrigal, E., Chapin, K., Chapin, F.S., Chelli, S., Chen, S., Chen, A., Cherubini, P., Chianucci, F., Choat, B., Chung, K., Chytrý, M., Ciccarelli, D., Coll, L., Collins, C.G., Conti, L., Coomes, D., Cornelissen, J.H.C., Cornwell, W.K., Corona, P., Coyea, M., Craine, J., Craven, D., Cromsigt, J.P.G.M., Csecserits, A., Cufar, K., Cuntz, M., da Silva, A.C., Dahlin, K.M., Dainese, M., Dalke, I., Dalle Fratte, M., Dang-Le, A.T., Danihelka, J., Dannoura, M., Dawson, S., de Beer, A.J., De Frutos, A., De Long, J.R., Dechant, B., Delagrange, S., Delpierre, N., Derroire, G., Dias, A.S., Diaz-Toribio, M.H., Dimitrakopoulos, P.G., Dobrowolski, M., Doktor, D., Dřevojan, P., Dong, N., Dransfield, J., Dressler, S., Duarte, L., Ducouret, E., Dullinger, S., Durka, W., Duursma, R., Dymova, O., E-Vojtkó, A., Eckstein, R.L., Ejtehadi, H., Elser, J., Emilio, T., Engemann, K., Erfanian, M.B., Erfmeier, A., Esquivel-Muelbert,

A., Esser, G., Estiarte, M., Domingues, T.F., Fagan, W.F., Fagúndez, J., Falster, D.S., Fan, Y., Fang, J., Farris, E., Fazlioglu, F., Feng, Y., Fernandez-Mendez, F., Ferrara, C., Ferreira, J., Fidelis, A., Finegan, B., Firn, J., Flowers, T.J., Flynn, D.F.B., Fontana, V., Forey, E., Forgiarini, C., François, L., Frangipani, M., Frank, D., Frenette-Dussault, C., Freschet, G.T., Fry, E.L., Fyllas, N.M., Mazzochini, G.G., Gachet, S., Gallagher, R., Ganade, G., Ganga, F., García-Palacios, P., Gargaglione, V., Garnier, E., Garrido, J.L., de Gasper, A.L., Gea-Izquierdo, G., Gibson, D., Gillison, A.N., Giroldo, A., Glasenhardt, M., Gleason, S., Gliesch, M., Goldberg, E., Göldel, B., Gonzalez-Akre, E., Gonzalez-Andujar, J.L., González-Melo, A., González-Robles, A., Graae, B.J., Granda, E., Graves, S., Green, W.A., Gregor, T., Gross, N., Guerin, G.R., Günther, A., Gutiérrez, A.G., Haddock, L., Haines, A., Hall, J., Hambuckers, A., Han, W., Harrison, S.P., Hattingh, W., Hawes, J.E., He, T., He, P., Heberling, J.M., Helm, A., Hempel, S., Hentschel, J., Hérault, B., Hereş, A., Herz, K., Heuertz, M., Hickler, T., Hietz, P., Higuchi, P., Hipp, A.L., Hirons, A., Hock, M., Hogan, J.A., Holl, K., Honnay, O., Hornstein, D., Hou, E., Hough-Snee, N., Hovstad, K.A., Ichie, T., Igić, B., Illa, E., Isaac, M., Ishihara, M., Ivanov, L., Ivanova, L., Iversen, C.M., Izquierdo, J., Jackson, R.B., Jackson, B., Jactel, H., Jagodzinski, A.M., Jandt, U., Jansen, S., Jenkins, T., Jentsch, A., Jespersen, J.R.P., Jiang, G., Johansen, J.L., Johnson, D., Jokela, E.J., Joly, C.A., Jordan, G.J., Joseph, G.S., Junaedi, D., Junker, R.R., Justes, E., Kabzems, R., Kane, J., Kaplan, Z., Kattenborn, T., Kavelenova, L., Kearsley, E., Kempel, A., Kenzo, T., Kerkhoff, A., Khalil, M.I., Kinlock, N.L., Kissling, W.D., Kitajima, K., Kitzberger, T., Kjøller, R., Klein, T., Kleyer, M., Klimešová, J., Klipel, J., Kloeppel, B., Klotz, S., Knops, J.M.H., Kohyama, T., Koike, F., Kollmann, J., Komac, B., Komatsu, K., König, C., Kraft, N.J.B., Kramer, K., Kreft, H., Kühn, I., Kumarathunge, D., Kuppler, J., Kurokawa, H., Kurosawa, Y., Kuyah, S., Laclau, J., Lafleur, B., Lallai, E., Lamb, E., Lamprecht, A., Larkin, D.J., Laughlin, D., Le Bagousse-Pinguet, Y., le Maire, G., le Roux, P.C., le Roux, E., Lee, T., Lens, F., Lewis, S.L., Lhotsky, B., Li, Y., Li, X., Lichstein, J.W., Liebergesell, M., Lim, J.Y., Lin, Y., Linares, J.C., Liu, C., Liu, D., Liu, U., Livingstone, S., Llusià, J., Lohbeck, M., López-García, Á., Lopez-Gonzalez, G., Lososová, Z., Louault, F., Lukács, B.A., Lukeš, P., Luo, Y., Lussu, M., Ma, S., Maciel Rabelo Pereira, C., Mack, M., Maire, V., Mäkelä, A., Mäkinen, H., Malhado, A.C.M., Mallik, A., Manning, P., Manzoni, S., Marchetti, Z., Marchino, L., Marcilio-Silva, V., Marcon, E., Marignani, M., Markesteijn, L., Martin, A., Martínez-Garza, C., Martínez-Vilalta, J., Mašková, T., Mason, K., Mason, N., Massad, T.J., Masse, J., Mayrose, I., McCarthy, J., McCormack, M.L., McCulloh, K., McFadden, I.R., McGill, B.J., McPartland, M.Y., Medeiros, J.S., Medlyn, B., Meerts, P., Mehrabi, Z., Meir, P., Melo, F.P.L., Mencuccini, M., Meredieu, C., Messier, J., Mészáros, I., Metsaranta, J., Michaletz, S.T., Michelaki, C., Migalina, S., Milla, R., Miller, J.E.D., Minden, V., Ming, R., Mokany, K., Moles, A.T., Molnár, A., Molofsky, J., Molz, M., Montgomery, R.A., Monty, A., Moravcová, L., Moreno-Martínez, A., Moretti, M., Mori, A.S., Mori, S., Morris, D., Morrison, J., Mucina, L., Mueller, S., Muir, C.D., Müller, S.C., Munoz, F., Myers-Smith, I.H., Myster, R.W., Nagano, M., Naidu, S., Narayanan, A., Natesan, B., Negoita, L., Nelson, A.S., Neuschulz, E.L., Ni, J., Niedrist, G., Nieto, J., Niinemets, Ü., Nolan, R., Nottebrock, H., Nouvellon, Y., Novakovskiy, A., Nystuen, K.O., O'Grady, A., O'Hara, K., O'Reilly-Nugent, A., Oakley, S., Oberhuber, W., Ohtsuka, T., Oliveira, R., Öllerer, K., Olson, M.E., Onipchenko, V., Onoda, Y., Onstein, R.E., Ordonez, J.C., Osada, N., Ostonen, I., Ottaviani, G., Otto, S., Overbeck, G.E., Ozinga, W.A., Pahl, A.T., Paine, C.E.T., Pakeman, R.J., Papageorgiou, A.C., Parfionova, E., Pärtel, M., Patacca, M., Paula, S., Paule, J., Pauli, H., Pausas, J.G., Peco, B., Penuelas, J., Perea, A., Peri, P.L., Petisco-Souza, A.C., Petraglia, A., Petritan, A.M., Phillips, O.L., Pierce, S., Pillar, V.D., Pisek, J., Pomogaybin, A., Poorter, H., Portsmuth, A., Poschlod, P., Potvin, C., Pounds, D., Powell, A.S., Power, S.A., Prinzing, A., Puglielli, G., Pyšek, P., Raevel, V., Rammig, A., Ransijn, J., Ray, C.A., Reich, P.B., Reichstein, M., Reid, D.E.B., Réjou-Méchain, M., de Dios, V.R., Ribeiro, S., Richardson, S., Riibak, K., Rillig, M.C., Riviera, F., Robert, E.M.R., Roberts, S., Robroek, B., Roddy, A., Rodrigues, A.V.,

503 Rogers, A., Rollinson, E., Rolo, V., Römermann, C., Ronzhina, D., Roscher, C., Rosell, J.A.,
504 Rosenfield, M.F., Rossi, C., Roy, D.B., Royer-Tardif, S., Rüger, N., Ruiz-Peinado, R., Rumpf, S.B.,
505 Rusch, G.M., Ryo, M., Sack, L., Saldaña, A., Salgado-Negret, B., Salguero-Gomez, R., Santa-
506 Regina, I., Santacruz-García, A.C., Santos, J., Sardans, J., Schamp, B., Scherer-Lorenzen, M.,
507 Schleuning, M., Schmid, B., Schmidt, M., Schmitt, S., Schneider, J. V., Schowanek, S.D., Schrader,
508 J., Schrodt, F., Schuldt, B., Schurr, F., Selaya Garvizu, G., Semchenko, M., Seymour, C., Sfair, J.C.,
509 Sharpe, J.M., Sheppard, C.S., Sheremetiev, S., Shiodera, S., Shipley, B., Shovon, T.A., Siebenkäs,
510 A., Sierra, C., Silva, V., Silva, M., Sitzia, T., Sjöman, H., Slot, M., Smith, N.G., Sodhi, D., Soltis, P.,
511 Soltis, D., Somers, B., Sonnier, G., Sørensen, M.V., Sosinski, E.E., Soudzilovskaia, N.A., Souza,
512 A.F., Spasojevic, M., Sperandii, M.G., Stan, A.B., Stegen, J., Steinbauer, K., Stephan, J.G., Sterck,
513 F., Stojanovic, D.B., Strydom, T., Suarez, M.L., Svenning, J., Svitková, I., Svitok, M., Svoboda, M.,
514 Swaine, E., Swenson, N., Tabarelli, M., Takagi, K., Tappeiner, U., Tarifa, R., Tauugourdeau, S.,
515 Tavsanoglu, C., te Beest, M., Tedersoo, L., Thiffault, N., Thom, D., Thomas, E., Thompson, K.,
516 Thornton, P.E., Thuiller, W., Tichý, L., Tissue, D., Tjoelker, M.G., Tng, D.Y.P., Tobias, J., Török, P.,
517 Tarin, T., Torres-Ruiz, J.M., Tóthmérész, B., Treurnicht, M., Trivellone, V., Trolliet, F., Trotsiuk, V.,
518 Tsakalos, J.L., Tsiripidis, I., Tysklind, N., Umehara, T., Usoltsev, V., Vadeboncoeur, M., Vaezi, J.,
519 Valladares, F., Vamosi, J., van Bodegom, P.M., van Breugel, M., Van Cleemput, E., van de Weg,
520 M., van der Merwe, S., van der Plas, F., van der Sande, M.T., van Kleunen, M., Van Meerbeek,
521 K., Vanderwel, M., Vanselow, K.A., Vårhammar, A., Varone, L., Vasquez Valderrama, M.Y.,
522 Vassilev, K., Vellend, M., Veneklaas, E.J., Verbeeck, H., Verheyen, K., Vibrans, A., Vieira, I.,
523 Villacís, J., Violle, C., Vivek, P., Wagner, K., Waldram, M., Waldron, A., Walker, A.P., Waller, M.,
524 Walther, G., Wang, H., Wang, F., Wang, W., Watkins, H., Watkins, J., Weber, U., Weedon, J.T.,
525 Wei, L., Weigelt, P., Weiher, E., Wells, A.W., Wellstein, C., Wenk, E., Westoby, M., Westwood,
526 A., White, P.J., Whitten, M., Williams, M., Winkler, D.E., Winter, K., Womack, C., Wright, I.J.,
527 Wright, S.J., Wright, J., Pinho, B.X., Ximenes, F., Yamada, T., Yamaji, K., Yanai, R., Yankov, N.,
528 Yguel, B., Zanini, K.J., Zanne, A.E., Zelený, D., Zhao, Y., Zheng, Jingming, Zheng, Ji, Ziemińska, K.,
529 Zirbel, C.R., Zizka, G., Zo-Bi, I.C., Zotz, G., Wirth, C., 2020. TRY plant trait database – enhanced
530 coverage and open access. Glob Chang Biol 26, 119–188. https://doi.org/10.1111/gcb.14904

531 Kattge, J., Knorr, W., Raddatz, T., Wirth, C., 2009. Quantifying photosynthetic capacity and its
532 relationship to leaf nitrogen content for global-scale terrestrial biosphere models. Glob Chang
533 Biol 15, 976–991. https://doi.org/10.1111/j.1365-2486.2008.01744.x

534 Laughlin, D.C., Fulé, P.Z., Huffman, D.W., Crouse, J., Laliberté, E., 2011. Climatic constraints on trait-
535 based forest assembly. Journal of Ecology 99, 1489–1499. https://doi.org/10.1111/j.1365-
536 2745.2011.01885.x

537 Laughlin, D.C., Leppert, J.J., Moore, M.M., Sieg, C.H., 2010. A multi-trait test of the leaf-height-seed
538 plant strategy scheme with 133 species from a pine forest flora. Funct Ecol 24, 493–501.
539 https://doi.org/10.1111/j.1365-2435.2009.01672.x

540 Lin, Y.-S., Medlyn, B.E., Duursma, R.A., Prentice, I.C., Wang, H., Baig, S., Eamus, D., de Dios, V.R.,
541 Mitchell, P., Ellsworth, D.S., de Beeck, M.O., Wallin, G., Uddling, J., Tarvainen, L., Linderson, M.-
542 L., Cernusak, L.A., Nippert, J.B., Ocheltree, T.W., Tissue, D.T., Martin-StPaul, N.K., Rogers, A.,
543 Warren, J.M., De Angelis, P., Hikosaka, K., Han, Q., Onoda, Y., Gimeno, T.E., Barton, C.V.M.,
544 Bennie, J., Bonal, D., Bosc, A., Löw, M., Macinins-Ng, C., Rey, A., Rowland, L., Setterfield, S.A.,
545 Tausz-Posch, S., Zaragoza-Castells, J., Broadmeadow, M.S.J., Drake, J.E., Freeman, M.,
546 Ghannoum, O., Hutley, L.B., Kelly, J.W., Kikuzawa, K., Kolari, P., Koyama, K., Limousin, J.-M.,
547 Meir, P., Lola da Costa, A.C., Mikkelsen, T.N., Salinas, N., Sun, W., Wingate, L., 2015. Optimal

stomatal behaviour around the world. Nat Clim Chang 5, 459–464. https://doi.org/10.1038/nclimate2550

Meir, P., Kruijt, B., Broadmeadow, M., Barbosa, E., Kull, O., Carswell, F., Nobre, A., Jarvis, P.G., 2002. Acclimation of photosynthetic capacity to irradiance in tree canopies in relation to leaf nitrogen concentration and leaf mass per unit area. Plant Cell Environ 25, 343–357. https://doi.org/10.1046/j.0016-8025.2001.00811.x

Mesonet, 2024. Monthly Rainfall Table: Norman (NRMN) Monthly Actual Oklahoma Mesonet Rainfall Table (in inches) [WWW Document]. URL https://www.mesonet.org/weather/rainfall/monthly-rainfall-table?ref=1210 (accessed 1.4.24).

Munroe, S.E.M., McInerney, F.A., Andrae, J., Welti, N., Guerin, G.R., Leitch, E., Hall, T., Szarvas, S., Atkins, R., Caddy-Retalic, S., Sparrow, B., 2021. The photosynthetic pathways of plant species surveyed in Australia's national terrestrial monitoring network. Sci Data 8, 97. https://doi.org/10.1038/s41597-021-00877-z

Pedregosa, F., Varoquaux, G., Gramfort, A., Michel, V., Thirion, B., Grisel, O., Blondel, M., Müller, A., Nothman, J., Louppe, G., Prettenhofer, P., Weiss, R., Dubourg, V., Vanderplas, J., Passos, A., Cournapeau, D., Brucher, M., Perrot, M., Duchesnay, É., 2012. Scikit-learn: Machine Learning in Python. Journal of Machine Learning Research 12, 2825–2830.

Poschlod, P., Kleyer, M., Jackel, A.-K., Dannemann, A., Tackenberg, O., 2003. BIOPOP — A database of plant traits and internet application for nature conservation. Folia Geobot 38, 263–271. https://doi.org/10.1007/BF02803198

Quested, H.M., Cornelissen, J.H.C., Press, M.C., Callaghan, T. V., Aerts, R., Trosien, F., Riemann, P., Gwynn-Jones, D., Kondratchuk, A., Jonasson, S.E., 2003. Decomposition of sub-arctic plants with differing nitrogen economies: A functional role for hemiparasites. Ecology 84, 3209–3221. https://doi.org/10.1890/02-0426

Reich, P.B., Oleksyn, J., Wright, I.J., 2009. Leaf phosphorus influences the photosynthesis–nitrogen relation: a cross-biome analysis of 314 species. Oecologia 160, 207–212. https://doi.org/10.1007/s00442-009-1291-3

Reich, P.B., Tjoelker, M.G., Pregitzer, K.S., Wright, I.J., Oleksyn, J., Machado, J., 2008. Scaling of respiration to nitrogen in leaves, stems and roots of higher land plants. Ecol Lett 11, 793–801. https://doi.org/10.1111/j.1461-0248.2008.01185.x

Richter, R., Schläpfer, D., 2002. Geo-atmospheric processing of airborne imaging spectrometry data. Part 2: Atmospheric/topographic correction. Int J Remote Sens 23, 2631–2649. https://doi.org/10.1080/01431160110115834

Schaepman, M.E., Jehle, M., Hueni, A., D'Odorico, P., Damm, A., Weyermann, J., Schneider, F.D., Laurent, V., Popp, C., Seidel, F.C., Lenhard, K., Gege, P., Küchler, C., Brazile, J., Kohler, P., De Vos, L., Meuleman, K., Meynart, R., Schläpfer, D., Kneubühler, M., Itten, K.I., 2015. Advanced radiometry measurements and Earth science applications with the Airborne Prism Experiment (APEX). Remote Sens Environ 158, 207–219. https://doi.org/10.1016/j.rse.2014.11.014

Schiefer, F., Schmidtlein, S., Kattenborn, T., 2021. The retrieval of plant functional traits from canopy spectra through RTM-inversions and statistical models are both critically affected by plant phenology. Ecol Indic 121, 107062. https://doi.org/10.1016/j.ecolind.2020.107062

Schläpfer, D., Richter, R., 2002. Geo-atmospheric processing of airborne imaging spectrometry data. Part 1: Parametric orthorectification. Int J Remote Sens 23, 2609–2630. https://doi.org/10.1080/01431160110115825

Schweiger, A.K., Schütz, M., Anderwald, P., Schaepman, M.E., Kneubühler, M., Haller, R., Risch, A.C., 2015. Foraging ecology of three sympatric ungulate species – Behavioural and resource maps indicate differences between chamois, ibex and red deer. Mov Ecol 3, 6. https://doi.org/10.1186/s40462-015-0033-x

Smith, N.G., Dukes, J.S., 2017. LCE: leaf carbon exchange data set for tropical, temperate, and boreal species of North and Central America. Ecology 98, 2978–2978. https://doi.org/10.1002/ecy.1992

Stevens, A., Ramirez-Lopez, L., 2022. An introduction to the prospectr package [WWW Document]. URL https://CRAN.R-project.org/package=prospectr

Van Der Meer, F., Bakker, W., Scholte, K., Skidmore, A., De Jong, S., Clevers, J., Addink, E., Epema, G., 2001. Spatial scale variations in vegetation indices and above-ground biomass estimates: Implications for MERIS. Int J Remote Sens 22, 3381–3396. https://doi.org/10.1080/01431160152609227

Verrelst, J., Dethier, S., Rivera, J.P., Munoz-Mari, J., Camps-Valls, G., Moreno, J., 2016. Active Learning Methods for Efficient Hybrid Biophysical Variable Retrieval. IEEE Geoscience and Remote Sensing Letters 13, 1012–1016. https://doi.org/10.1109/LGRS.2016.2560799

Wang, H., Harrison, S.P., Prentice, I.C., Yang, Y., Bai, F., Furstenau Togashi, H., Wang, M., Zhou, S., Ni, J., 2017. The China Plant Trait Database.

Wright, I.J., Reich, P.B., Westoby, M., Ackerly, D.D., Baruch, Z., Bongers, F., Cavender-Bares, J., Chapin, T., Cornelissen, J.H.C., Diemer, M., Flexas, J., Garnier, E., Groom, P.K., Gulias, J., Hikosaka, K., Lamont, B.B., Lee, T., Lee, W., Lusk, C., Midgley, J.J., Navas, M.-L., Niinemets, Ü., Oleksyn, J., Osada, N., Poorter, H., Poot, P., Prior, L., Pyankov, V.I., Roumet, C., Thomas, S.C., Tjoelker, M.G., Veneklaas, E.J., Villar, R., 2004. The worldwide leaf economics spectrum. Nature 428, 821–827. https://doi.org/10.1038/nature02403

Yuhas, R., Goetz, A., Boardman, J., 1992. Discrimination among semi-arid landscape endmembers using the spectral angle mapper (SAM) algorithm, in: Summaries of the Third Annual JPL Airborne Geoscience Workshop. Volume 1: AVIRIS Workshop. JPL, pp. 147–149.